



Magnetisme i estructura en aliatges funcionals

Magnetism and structure in functional alloys

David González Alonso

ADVERTIMENT. La consulta d'aquesta tesi queda condicionada a l'acceptació de les següents condicions d'ús: La difusió d'aquesta tesi per mitjà del servei TDX (www.tdx.cat) i a través del Dipòsit Digital de la UB (diposit.ub.edu) ha estat autoritzada pels titulars dels drets de propietat intel·lectual únicament per a usos privats emmarcats en activitats d'investigació i docència. No s'autoritza la seva reproducció amb finalitats de lucre ni la seva difusió i posada a disposició des d'un lloc aliè al servei TDX ni al Dipòsit Digital de la UB. No s'autoritza la presentació del seu contingut en una finestra o marc aliè a TDX o al Dipòsit Digital de la UB (framing). Aquesta reserva de drets afecta tant al resum de presentació de la tesi com als seus continguts. En la utilització o cita de parts de la tesi és obligat indicar el nom de la persona autora.

ADVERTENCIA. La consulta de esta tesis queda condicionada a la aceptación de las siguientes condiciones de uso: La difusión de esta tesis por medio del servicio TDR (www.tdx.cat) y a través del Repositorio Digital de la UB (diposit.ub.edu) ha sido autorizada por los titulares de los derechos de propiedad intelectual únicamente para usos privados enmarcados en actividades de investigación y docencia. No se autoriza su reproducción con finalidades de lucro ni su difusión y puesta a disposición desde un sitio ajeno al servicio TDR o al Repositorio Digital de la UB. No se autoriza la presentación de su contenido en una ventana o marco ajeno a TDR o al Repositorio Digital de la UB (framing). Esta reserva de derechos afecta tanto al resumen de presentación de la tesis como a sus contenidos. En la utilización o cita de partes de la tesis es obligado indicar el nombre de la persona autora.

WARNING. On having consulted this thesis you're accepting the following use conditions: Spreading this thesis by the TDX (www.tdx.cat) service and by the UB Digital Repository (diposit.ub.edu) has been authorized by the titular of the intellectual property rights only for private uses placed in investigation and teaching activities. Reproduction with lucrative aims is not authorized nor its spreading and availability from a site foreign to the TDX service or to the UB Digital Repository. Introducing its content in a window or frame foreign to the TDX service or to the UB Digital Repository is not authorized (framing). Those rights affect to the presentation summary of the thesis as well as to its contents. In the using or citation of parts of the thesis it's obliged to indicate the name of the author.



FACULTAT DE FÍSICA

DEPARTAMENT D'ESTRUCTURA I CONSTITUENTS DE LA MATÈRIA

PHD THESIS:

**MAGNETISME I ESTRUCTURA EN
ALIATGES FUNCIONALS**

**MAGNETISM AND STRUCTURE IN
FUNCTIONAL ALLOYS**

A Thesis submitted by **David González Alonso** for the degree of
Doctor of Philosophy in the University of Barcelona

27.01.14

Tutored and Supervised by:

Lluís Mañosa i Carrera

*A la memoria de mi pequeño compañero Cuki,
a mis padres y a mi Dulcinea de Sel del Tojo.*

ABSTRACT

DEPENDING on whether the magnetic field is applied adiabatically to a sample or in isothermal conditions, the thermal response of the material will result in a temperature change or in an entropy change, respectively. In both cases, one obtains a thermal response which is known as *Magnetocaloric Effect* (MCE). In fact, any variation of the thermal variables can be classified based on the external applied field. Thus, depending on the nature of the external stimulus we will obtain a different caloric effect, such as the aforementioned magnetocaloric effect when applying a magnetic field.

In the 1930s this magnetocaloric effect, indeed, showed up the possibility to reach temperatures well below 1 K through the adiabatic demagnetization of paramagnetic salts. Today, the discovery of new materials together with technological improvements are bridging the gap between research and solid-state refrigeration at room temperature.

In summary, within this thesis we have studied a variety of magnetic materials exhibiting different giant Caloric effects that are proving to be very promising materials

for eco-friendly solid-state refrigeration purposes.

BÉ sigui el canvi de temperatura que experimenta un material a l'aplicar-li un camp magnètic en condicions adiabàtiques, o bé sigui el canvi d'entropia del material com a conseqüència de la modificació del camp magnètic en condicions isoterms, en tots dos casos aquest canvi es coneix com a *Efecte Magnetocalòric* (MCE).

En qualsevol cas, l'aplicació o la retirada d'un camp magnètic extern, és el responsable de l'alineament o desalineament, respectivament, dels moments magnètics als àtoms del material. De fet, és aquest ordenament dels moments magnètics als àtoms del material, el que provoca una disminució de l'entropia associada als graus de llibertat magnètics del material. Si a més, el camp s'aplica en condicions adiabàtiques, resulta que per tal de mantenir l'entropia del sistema constant, aquesta disminució de l'entropia magnètica reverteix en un augment de l'entropia lligada als graus de llibertat de la xarxa cristal·lina, i conseqüentment, en un augment en la temperatura del sistema. Si en canvi, es retira el camp magnètic en condicions adiabàtiques, l'entropia magnètica és la que s'incrementa en augmentar el grau de desordre del

nostre sistema; cosa que pel raonament anterior, resulta en la disminució de la temperatura final del nostre sistema com a conseqüència de la reducció de l'entropia associada als graus de llibertat de la xarxa [a la figura 1.3 és pot trobar un esquema del procés de magnetització i desmagnetització d'una sal paramagnètica].

Com acabem de veure, l'MCE rau en un acoblament “magneto-cristal·lí”¹ entre la xarxa del material i el camp magnètic extern aplicat. A més, l'MCE és un efecte que es pot observar en una gran diversitat de materials, això si, han de ser materials magnètics [1, 2].

A dia d'avui, existeix certa polèmica sobre qui va ser el primer en observar l'MCE [3]. Malgrat això, existeix un ampli consens en atorgar aquest honor a E. Warburg per un estudi publicat l'any 1881 [4]. De totes maneres, no va ser fins als anys trenta del segle passat, s. XX, quan es va trobar l'MCE com a solució per a la refrigeració. Això si, l'aplicació d'aquest efecte en la nouvinguda refrigeració magnètica, hauria d'estar restringit a temperatures molt baixes i properes al zero absolut. De fet, va ser l'estudi d'aquest efecte en sals paramagnètiques per les que en W.F. Giaque [5, 6] va ser guardonat amb el premi Nobel de Química al 1949. Tècnica encara emprada per a l'obtenció d'heli líquid.

No va ser fins al 1997, amb el descobriment de l'MCE *gegant* a temperatura ambient [7] juntament amb l'acord del protocol de Kyoto [8], que l'MCE va disposar novament de l'atenció i de la inversió necessària per poder fer recerca. Aquest acord rep el nom en reconeixement a la ciutat on va ser adoptat aquell mateix any. De fet, el protocol de Kyoto va ser un acord internacional fruit de la concienciació del món occidental per intentar tallar l'augment progressiu de les temperatures a escala planetària, tot reduint les taxes de pol·lució dels països desenvolupats. Amb aquesta

¹Això passarà sempre que parlem d'àtoms disposats de forma regular en una xarxa cristal·lina, si no estarem parlant d'amorfs.

adopció, s'intentava redreçar la demora que estava portant al planeta cap a un canvi climàtic, amb repercussions ecològiques, econòmiques i socials a escala mundial.

Deixant enrere els temes espinosos, tal i com s'ha indicat abans, la desmagnetització era un procés restringit, fins llavors, per assolir molt baixes temperatures. D'altra banda, per a temperatures prou elevades –per sobre dels 20 K–, els materials coneguts presentaven un canvi de temperatura adiabàtic menyspreable, com a conseqüència directa de l'augment de la capacitat calorífica dels materials amb la temperatura. L'alternativa era trobar materials que tinguessin transicions magnètiques properes a la temperatura d'interès i amb un fort salt en la magnetització². Materials amb una transició propera a la temperatura ambient es podrien fer servir per a sistemes de climatització, o bé, com a frigorífics per a la conserva d'aliments.

L'únic element conegut que presenta una transició magnètica important a prop de temperatura ambient és el gadolini. Una terra rara, de preu elevat i escassa abundància [veure figura 1.6], amb una temperatura de transició de 294 K. De fet, el material que van trobar al 1997 *Pecharsky* i *Gschneidner* és un aliatge tipus Gd–Si–Ge, amb Gd en la seva composició i que exhibeix un MCE *gegant* al voltant de temperatura ambient com a conseqüència d'una transició de primer ordre a prop de la transició magnètica [9]. Aquest descobriment, tal com hem mencionat amb anterioritat, va desfermar l'interès en la recerca de nous i millors materials refrigeradors amb un MCE gegant en el rang de temperatures desitjat, fàcilment modificables i amb unes propietats que es conservin al llarg d'un temps d'ús que sigui raonable.

També cal destacar el paper pioner de G.W. Brown [10], qui va ser el primer en construir un sistema de refrigeració basat en la desmagnetització adiabàtica del Gd. Ell va ser qui va fer realitat aquesta idea de la refrigeració magnètica a temperatura

²Materials amb una elevada temperatura de Curie –transició magnètica Ferro-Para.

ambient; fent més fàcil la feina dels qui van seguir les seves petjades. A més, la refrigeració magnètica ha demostrat ser una alternativa neta i més eficient a les tècniques convencionals basades en la compressió de gasos nocius per al medi ambient [11].

Finalment, m'agradaria generalitzar que qualsevol resposta tèrmica, ja sigui associada a un canvi de temperatura o a un canvi d'entropia, i com a resultat de l'aplicació d'un camp extern –com ara la pressió o l'esforç, entre d'altres– es pot definir com a *Efecte Calòric* [12–16] [en la figura 1.1 es pot veure un esquema dels diferents efectes calòrics estudiats en aquesta tesi].

En resum, en aquesta tesi s'han estudiat materials que presenten transicions magneto-estructurals. Concretament hem estudiat materials magnètics de la família dels aliatges Heusler amb memòria de forma, i compostos intermetàl·lics de la família La–Fe–Si. Hem realitzat mesures magnètiques i de calorimetria sota camps externs –mecànics i magnètics– per tal de determinar els efectes magnetocalòrics, barocalòrics i elastocalòrics d'aquests compostos. A més, s'han observat valors grans per als canvis d'entropia i de temperatura, cosa que fa més pròxim el somni de la refrigeració en estat sòlid.

Contents

Abstract	v
Resum	vii
List of Abbreviations	xv
List of Symbols	xvii
1 Introduction	1
1.1 Caloric Effects	2
1.2 Magnetocaloric Effect	4
1.3 Magnetic Refrigeration	12
1.4 The Heusler alloys	18
1.5 The Martensitic Transformation	24
1.6 The La[Fe(Si)] ₁₃ family of alloys	37
1.7 Magnetic Interactions	38
2 Experimental Techniques	41
2.1 Sample Preparation	41
2.2 Calorimetry	43
2.2.1 Direct Methods	45
2.2.2 Indirect Methods	49
2.3 Ultrasonic Experiments	50

3	Results	53
3.1	List of Contributions	53
3.2	Factor d'Impacte	54
3.3	Participació de David González Alonso en els articles de la seva tesi	55
3.3.1	Article 1: "Lattice dynamics in magnetic superelastic Ni-Mn-In alloys: Neutron scattering and ultrasonic experiments"	55
3.3.2	Article 2: "Stress-and magnetic field-induced entropy changes in Fe-doped Ni-Mn-Ga shape-memory alloys"	55
3.3.3	Article 3: "Giant solid-state barocaloric effect in the Ni-Mn-In magnetic shape memory alloy"	56
3.3.4	Article 4: "Inverse barocaloric effect in the giant magnetocaloric La-Fe-Si-Co compound"	57
3.3.5	Article 5: "Caloric effects induced by magnetic and mechanical fields in a $\text{Ni}_{50}\text{Mn}_{25-x}\text{Ga}_{25}\text{Co}_x$ magnetic shape memory alloy"	58
3.4	Paper 1: <i>Phys. Rev. B</i> 79 , 214118 (2009)	59
3.5	Paper 2: <i>Appl. Phys. Lett.</i> 96 , 071912 (2010)	67
3.6	Paper 3: <i>Nat. Mater.</i> 9 , 478 (2010)	71
3.7	Paper 4: <i>Nat. Commun.</i> 2 , 595 (2011)	77
3.8	Paper 5: <i>Phys. Rev. B</i> 83 , 174109 (2011)	83
4	Resum dels Resultats i Conclusions	91
5	Summary and Conclusions	97
	Bibliography	103
	Curriculum Vitae	115

List of Tables

1.1	A summary of the different atomic orders for Heusler alloys	21
2.1	A rough description of a selected Thermal Analysis methods.	44
2.2	A brief description of the different magnetometers.	51
2.3	Propagation modes used in ultrasonic measurements.	51

List of Figures

1.1	Diagram of the different Caloric Effects studied within this thesis . . .	3
1.2	Sketch for the Weiss theory of ferromagnetism	5
1.3	Schematic representation of the MCE proposal by Debye and Giaque in a Paramagnet	7
1.4	The impact of the MCE over the past 44 years	10
1.5	$ \Delta S_{iso} $ and $ \Delta T_{ad} $ as a function of the transition temperature	14
1.6	Time evolution in Rare-Earth price and global production	16
1.7	Periodic table of elements that reveals the possible combination of the Heusler alloys by a colored elements code	19

1.8	Crystal structures of Heusler alloys	20
1.9	Representation of the Austenite and non-modulated/modulated martensite structures for $Ni_{50}Mn_{50-x}Z_x$ (Z: Ga, In, Sn and Sb) alloys	25
1.10	Phase diagram of Ni–Mn–Z (Z: Ga, In, Sn and Sb) alloys	27
1.11	Sketch of a Martensitic Transformation	28
1.12	Shape-memory effects	30
1.13	Schematic representation of the Gibb’s free energy in the forward and in the reverse martensitic transformation	32
1.14	Schematic representation of the entropy change in the vicinity of a first-order magnetic transition	34
1.15	Schematic representation of the different phases in the vicinity of a first-order magnetic phase transition	36
1.16	Indirect Exchange interaction	39
2.1	Diagram of the different Thermo-Analytical methods	43
2.2	Schematic representation of a DSC	46
2.3	Typical calibration of a DSC	47
2.4	Sketch of the adiabatic temperature-change set-ups from both University of Duisburg-Essen and University of Barcelona	48
2.5	Direct ΔT_{ad} measurements from the University of Barcelona	49
2.6	MPMS system	50
2.7	Ultrasonic experiment	52

List of Abbreviations

A_f	austenite finish temperature
A_s	austenite start temperature
AF	antiferromagnet or antiferromagnetic
AMR	active magnetic regenerator
bcc	body-centered cubic
bct	body-centered tetragonal
BCE	barocaloric effect
COP	coefficient of performance
DSC	diferential scanning calorimetry
DTA	diferential thermal analysis
ECE	elasto-caloric effect
EDX	energy dispersive X-ray analysis
FC	field-cooled
fcc	face-centered cubic
FH	field-heated
FI	ferrimagnetic
FM	ferromagnetic
$FOST$	first-order structural phase transformation
$FOMT$	first-order magnetic phase transformation
$FWHM$	Full width at half maximum
MCE	magnetocaloric effect
M_f	martensite finish temperature
M_s	martensite start temperature

<i>MT</i>	martensitic transformation
<i>PM</i>	paramagnetic
<i>RCP</i>	relative cooling power
<i>RE</i>	rare earth
<i>SMA</i>	shape memory alloys
<i>SQUID</i>	superconducting quantum interference device
T_C^A	Curie temperature of the austenite phase
T_C^M	Curie temperature of the martensite phase
<i>XYZ</i>	half-Heusler
X_2YZ	full-Heusler
<i>ZFC</i>	zero-field-cooled

List of Symbols

ΔT_{ad}	adiabatic temperature change
μ_B	Bohr magneton ($9.274096 \times 10^{-24} \text{ J/T}$)
\vec{E}	electric field
e	elementary charge ($1.602 \times 10^{-19} \text{ C}$)
S	entropy
\vec{F}	force
G	Gibbs free energy
C_x	heat capacity at constant “x”
ΔS_{iso}	isothermal entropy change
a	lattice constant
\vec{H}	magnetic field
\vec{m}	magnetic moment
\vec{H}_e	molecular or effective field
A_0	original cross-section
L_0	original length
L	distorted length
a'	distorted lattice constant
ΔL	length-change ($L - L_0$)
ϵ	strain ($\Delta L/L_0$)
σ	stress (F/A_0)
μ_0	vacuum permeability ($4\pi \times 10^{-7} \text{ H/m}$)
e/a	valence electron concentration

CHAPTER 1

INTRODUCTION

THE Western society today relies on technology to maintain the welfare society. But, at the same time, this technology is supported by a market-based capitalism which enables the full commercialization of goods, people and, actually, governments. In fact, although it still prevails, the Western way of life has failed just because only a minority on Earth deserves this privilege, but at the expense of the rest. As a matter of fact, the Planned Obsolescence¹ [17] in industrial design, the widening gap between rich and poverty, the scarcity and high price of raw materials, the environmental problem are just the result of such policy.

Herein, the present work faces the pollution problem through available eco-friendly cooling devices. A sustainable technology that has been revealed as a more energy-efficient, less noisy, more compact, reducing the CO₂ emission, built-up without toxic materials and, therefore, reducing the impact on the environment [2, 11, 18].

¹The deliberate policy of shortening the product lifespans to increase consumer demand at the beginning of 1920.

This technology is an old–one technology [6], which was used to attain temperatures below 1 K, based on the response of certain new–materials that exhibit different caloric effects in consequence of an external stimulus.

Many efforts have been focused on the society development. Now we have the challenge to reduce a part of the impact of our society in the environment. It is a tough problem, but we have the responsibility to face the problem with the flavour of our contribution.

1.1 Caloric Effects

Broadly speaking, any thermal response in a material as a result of an external applied field is defined as a *Caloric Effect*. Thus, any variation of the thermal variables (T, S) can be classified based on the nature of the external applied field. Therefore, any *Caloric Effect*– (ω, Ω) ² is classified in terms of a generalized force (ω) and its conjugated generalized displacement (Ω) [see fig. 1.1 for a sketch of the different Caloric Effects studied within this thesis], e.g., the *magnetocaloric effect* arises from the variation of magnetic variables– (H, M) [7, 19, 20], the *elastocaloric effect*– (σ, ϵ) ³ [12, 15], the *barocaloric effect*– $(-p, V)$ ⁴ [13, 14], the *electrocaloric effect*– (E, P) [16] and so on.

Furthermore, *Caloric Effects*, i.e., the *Isothermal Entropy change*, $\langle\langle \Delta S_{iso} \rangle\rangle$, and

² Ω and ω are different rank tensors depending on the external stimuli, e.g., if ω =pressure and Ω =volume, then they are zero-rank tensors (scalars). But if ω = σ –i.e., stress– and Ω = ϵ –i.e., strain–, then they are second-rank tensors.

³The *stress*– σ and the *strain*– ϵ are defined as the applied force per unit area and the deformation of the sample due to the stress applied, respectively.

⁴When applying a generalized force, usually the response of the generalized displacement is positive. But for a positive applied pressure, the volume response is negative.

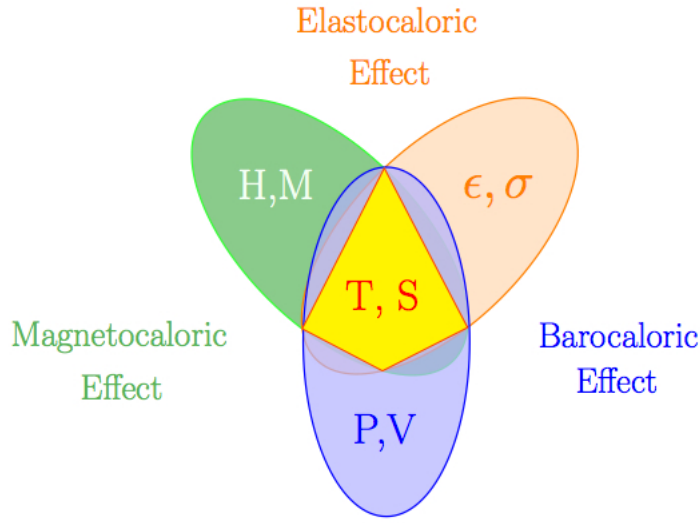


Figure 1.1: Diagram of the different Caloric Effects studied in this thesis based on the nature of an external stimulus.

the *Adiabatic Temperature change*, $\langle\langle \Delta T_{ad} \rangle\rangle^5$, can be calculated in terms of a *response function*, $\langle\langle \xi_{\Omega} = \left(\frac{\partial \Omega}{\partial T}\right)_{\omega} \rangle\rangle$, as follows:

$$\Delta S_{iso}^{\omega_0 \rightarrow \omega} = S(T, \omega) - S(T, \omega_0) = \int_{\omega_0}^{\omega} \xi_{\Omega} \cdot d\omega \quad (1.1)$$

$$\Delta T_{ad}^{\omega_0 \rightarrow \omega} = T(S, \omega) - T(S, \omega_0) = - \int_{\omega_0}^{\omega} \frac{T}{C(\omega, T)} \xi_{\Omega} \cdot d\omega \quad (1.2)$$

It is clear that the above equations are really sensitive to the *response function*⁶. In addition, any thermal variation of a generalized displacement (Ω) is taken into account through the $\langle\langle \xi_{\Omega} \rangle\rangle$ component in the direction of the external perturbative field (ω) in order to compute the related *Caloric Effect* [eqs. 1.1 and 1.2]. Therefore,

⁵In eq. 1.2, $C(\omega, T)$ represents the heat capacity of the material.

⁶See fig. 1.14b on page 34 for the particular case of MCE.

in an adiabatic process all the change is stored by the lattice through its heat capacity C resulting in a temperature change, $\langle\langle\Delta T_{ad}\rangle\rangle$. On the other hand, in an isotherm process all the contribution results in an entropy change, $\langle\langle\Delta S_{iso}\rangle\rangle$ [21]. A historical approach has been introduced below.

1.2 MCE: Magnetocaloric Effect

The thermal response (T, S) in consequence of the application of a magnetic field $(\mu_0\vec{H})$ on a magnetic material is straightforward known as *Magnetocaloric Effect*. The vast majority of the authors point out that the first whoever noticed the MCE was E. Warburg [4, 22] in the late nineteenth century in iron.

By that time, not only iron but nickel and cobalt were also ferromagnets⁷ used in order to unravel the mechanism that underlay their magnetic behavior⁸. But it would not be until 1907 that P. Weiss [25] built a suitable explanation for the Ferro-Para transition through a modification in the Langevin theory of paramagnetism⁹. In

⁷Shortly, a ferromagnet is any material with a spontaneous magnetic moment even in the absence of a magnetic field.

⁸In the 1850s M. Faraday and in the 1860s W. Thomson —later Lord Kelvin— studied the sharp end in the magnetization when ferromagnets are heated above a certain characteristic temperature —the Curie temperature [23]. The corresponding Curie temperature for the previous listed materials are: $T_C^{Ni} = 628$ K, $T_C^{Fe} = 1044$ K and $T_C^{Co} = 1388$ K. Furthermore, it should be notice that no material is known to have a higher Curie temperature than cobalt. [24]. In that sense, due to its Curie room temperature, Nickel would have been a more suitable candidate for the MCE.

⁹For an isotropic material formed by a single element, Langevin Theory of paramagnetism has two important assumptions: firstly, Langevin supposed that atoms with unpaired electrons have a net magnetic moment (m_o —orbital and m_s —spin) that interacts with the magnetic field by minimizing its magnetic energy (E_M). Secondly, he imposed noninteracting magnetic moments between them. This two general and uniform hypothesis leads to a classical Boltzmann statistics

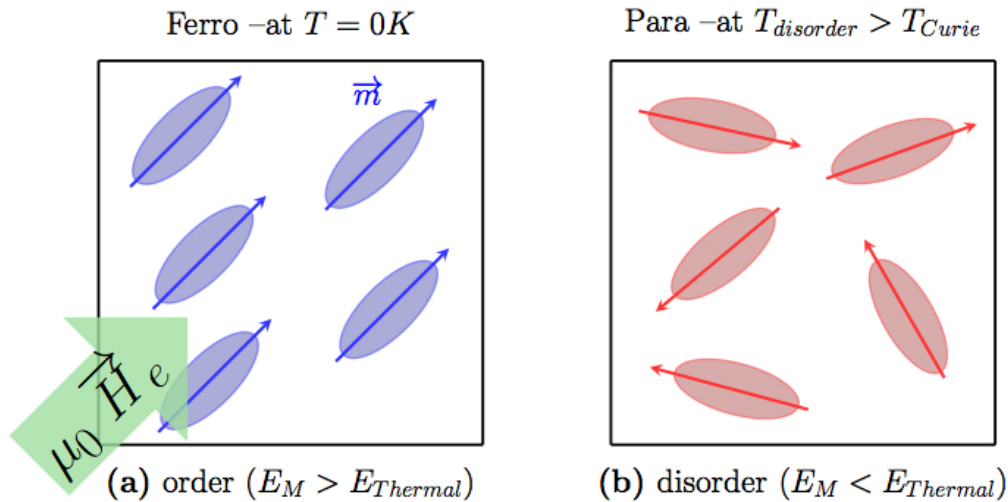


Figure 1.2: Sketch for the Weiss theory of ferromagnetism –the “*molecular field*”, \vec{H}_e .

his model, Weiss introduced an interaction between the –localized– atomic magnetic moments through an effective field –the «*molecular field*», \vec{H}_e –, which extended the Langevin theory from paramagnetism to ferromagnetism. The goodness of the Weiss model was confirmed when there was found a group within the paramagnets, such as Nickel and the lanthanides –4f electrons–, that obey very well the Curie–Weiss law [26]¹⁰.

Now, let’s provide an easy example to shed light on the ordering effect of the «*molecular field*»¹¹. In fig. 1.2a, it is represented a solid ferromagnet at 0 K with

– $\exp(-E_M/\kappa_B T)$ – in the population of the electronic energy states.

¹⁰As a result of the fact that in the Weiss model the magnetic moments of the unpaired electrons should be localized –in the atom–, his model does not offer a solution for the electrons that are shared with neighboring atoms –i.e., Itinerant Electron Models (IEM).

¹¹If Weiss had presented his model after 1917 –when the diffraction experiments showed that the moments were localized in the atoms–, he would not have called «*molecular field*». But X-ray diffraction was first time noticed in 1912. Therefore, the «atomic» term would have been a more

magnetic moments (\vec{m}) localized in the atoms. There arises—in the ferromagnet—a collective behavior that aligns the atomic moments parallel along the direction of what Weiss defined as «*molecular field*»¹². Thus, the «*molecular field*» provides to the ferromagnet a magnetic order as a consequence of the minimization of its magnetic energy¹³. However, as the system heats up the thermal energy becomes more and more important up to a point where the order vanishes and the magnetization drops down—at the Curie temperature. The figure 1.2b shows that at temperatures well above the Curie point the thermal effect prevails and exhibits the disordering effect of the thermal energy¹⁴, i.e., the Paramagnetic state.

So far, it does seem easy to extrapolate that the more «*molecular field*», the higher transition temperature—i.e., the more order in the ferromagnet, the higher temperature is need to vanish the arrangement of the magnetic moments. Consequently, if we apply a magnetic field on the ferromagnet it will undergo the magnetic transition at higher temperature. Accordingly, the magnetization of any conventional ferromagnet will increase as the magnetic field rises, which agrees the Weiss model— $\Delta M_{H_0 \rightarrow H_{ext}}(T) = M_{H_{ext}}(T) - M_{H_0}(T) > 0$, at any fixed temperature. Therefore, the maximum change in the magnetization— ΔM —will take place during the magnetic transition, i.e., at the Curie point.

Later on, in 1918 P.Weiss and A.Picard [28] observed in the vicinity of Nickel Curie point ($T_{Curie}^{Ni} = 628$ K) a temperature span of 0.7 K when applying a magnetic field of 1.5T. In that moment, Weiss and Picard established the basis that open up

suitable election, instead of the «molecular» one.

¹²The «*molecular field*» is an uniform field that is proportional to the magnetic moment per unit volume of a magnetic domain—i.e., the volume within all the moments are parallel ($\vec{H}_e \propto \vec{M}_{domain}$).

¹³The energy of a magnetic system is defined as: $E_M = -\mu_0 \vec{M} \cdot \vec{H}$.

¹⁴Thermal energy: $E_T = k_B T$

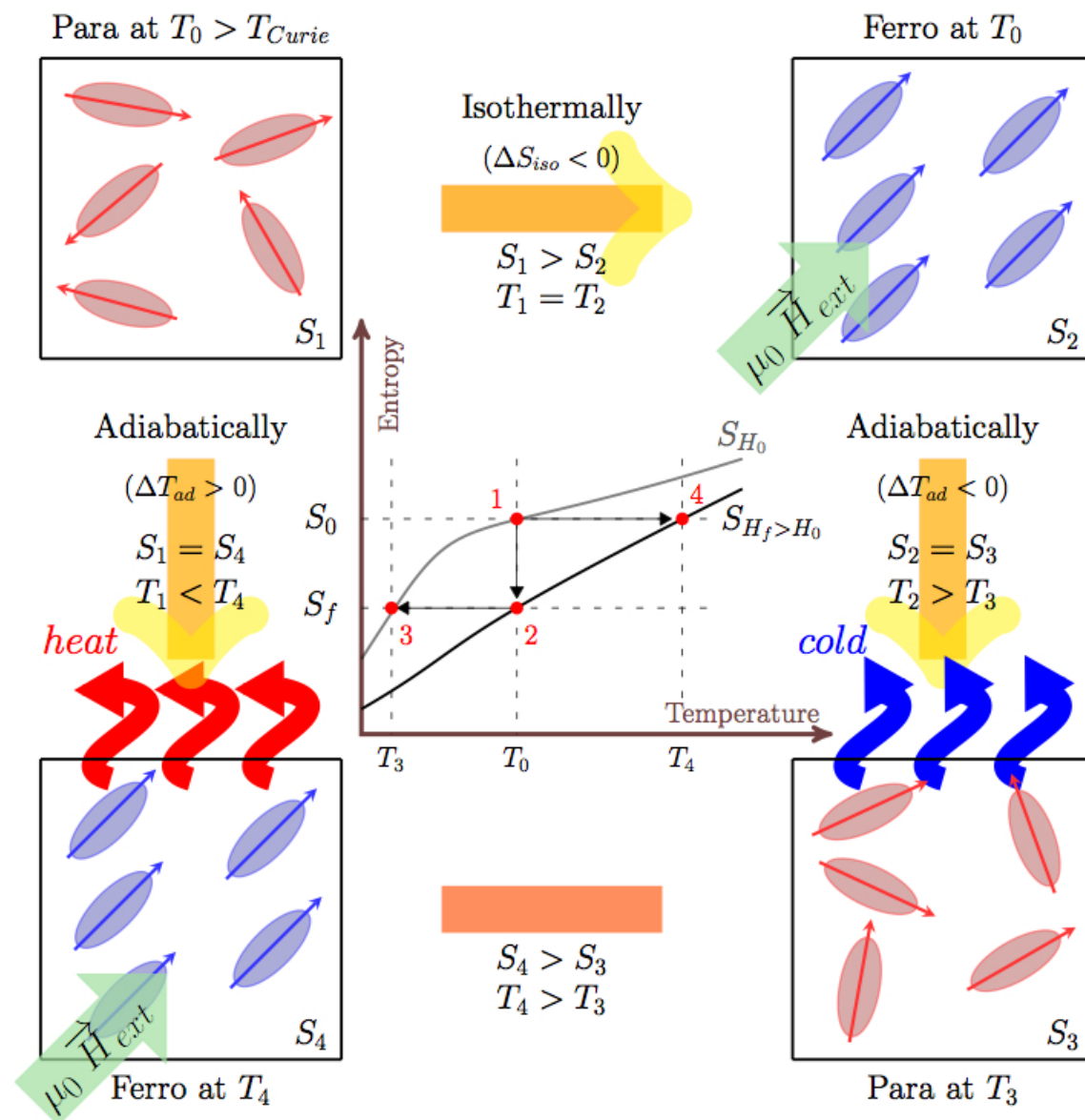


Figure 1.3: Schematic representation of the MCE proposal by Debye and Giaque in a Paramagnet [5, 27]. In the beginning, the system starts off as a *Paramagnet* —with $T_0 > T_{Curie}$. In track (i) or section 1-2-3, the system finally cools down: in section 1-2, an external magnetic field is applied isothermally, so that the system reduces its entropy. Afterwards, the field is adiabatically removed to the *Para*-state (section 2-3) obtaining a negative ΔT_{ad} . On the other hand, in track (ii) or section 1-4, an external magnetic field is applied through the original *Para*-state towards a *Ferro*-state, which results in a positive temperature span $-\Delta T_{ad}$.

a new technology for magnetic cooling. Soon after, as an evidence of that, P. Debye [27, 29] and W.F. Giauque [5] both independently described in detail a similar procedure based on the low-temperature magnetocaloric properties of a paramagnetic salt at the liquid helium temperatures¹⁵. But was in 1933 when the pioneering work of Giauque¹⁶ and MacDougall finally showed up the possibility to reach temperatures well below 1K through the adiabatic demagnetization of the paramagnetic $Gd_2(SO_4)_3 \times 8H_2O$ salt [6].

The figure 1.3 presents the MCE proposal by Debye and Giauque in a paramagnetic salt. Initially, the magnetic moments are disordered –aligned randomly– by thermal effects (point 1 in the fig. 1.3). When a moderate¹⁷ magnetic field is applied isothermally, the moments arrange mostly along the magnetic field (track 1-2), which increases the magnetization and decreases the total entropy of the system. At this point, if we remove the field adiabatically ($\Delta S^{2-3} = 0$) –the system is also in isochoric and isobaric conditions–, the total entropy of the system remains constant (track 2-3). So that, the entropy related to the magnetic moments increases –i.e., the moments get disordered when the field is removed: $\Delta S_{spin}^{2-3} > 0$ – and, therefore, the vibrational entropy decreases through a cooling –($\Delta S^{2-3} = \Delta S_{spin}^{2-3} + \Delta S_{lattice}^{2-3} =$

¹⁵«A paramagnetic salt is inserted between the poles of a powerful magnet contained in a bath of liquid helium. As the field is turned on, the magnetic dipoles are oriented, with the production of heat; in turn, this heat is absorbed in the bath. Following the strong magnetization, the salt is insulated from its surroundings. On decrease of the field strength the orientation of the dipoles moves toward randomization, increasing the potential energy at the expense of the kinetic energy of the molecules. Accordingly, the temperature of the salt is decreased» [29].

¹⁶The Nobel Prize in Chemistry 1949 was awarded to William F. Giauque «for his contributions in the field of chemical thermodynamics, particularly concerning the behaviour of substances at extremely low temperatures».

¹⁷When a magnetic field is reached by means of permanent magnets, e.g., up to $\mu_0 H \approx 2T$ [30].

$0 \xrightarrow{\Delta S_{spin}^{2-3} > 0} \Delta S_{lattice}^{2-3} < 0 \Rightarrow \Delta T_{ad}^{2-3} < 0$). However, if a magnetic field is applied adiabatically in the original Paramagnetic-state, then the system –at the end Ferro-state– finally heats up –remaining the total entropy constant (track 1-4).

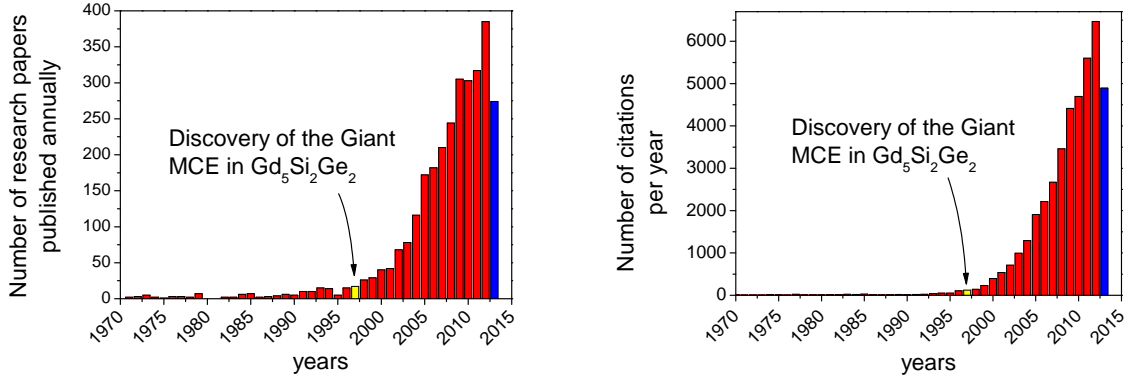
From the above, it results clear that in conventional ferromagnets the MCE arises roughly from the –ordered– alignment of the magnetic moments on applying an external magnetic field. It is worth noting that as well as the majority of the authors target Warburg to be the first, it may not be so clear because there exists a controversy for his pioneering role in the discovery of the MCE [3]. In addition, shortly after the discovery of the MCE –leaving aside this controversy– new efforts were carried out in technologies based on magnetic effects. Hence, back to the 1880-1890s T.A.Edison [31, 32] and N.Tesla [33, 34] registered different versions of “*thermomagnetic-motors*”, which were suggested by J.Steffan [35, 36]. But unable to compete with contemporaneous motors and generators.¹⁸

Now, let’s make a break up to 1997. For the time being, we have shown the convenient use of the MCE in paramagnetic salts to reach temperatures close to liquid helium. In the fig. 1.3 on page 7 and, previously, on fig. 1.2, it was clearly stated the ordering role that plays the magnetic field in the Ferro–Para transition¹⁹, which enhances the magnetization change at the Curie-Point —i.e., $\Delta M_{Curie-Point}^{H_{ext}} > \Delta M_{Curie-Point}^{no-field}$. In light of that, when a magnetic field is applied isothermally the paramagnet tends to arrange its moments at the expense of the entropy of the system, thus resulting in a decrease in the total entropy of the system (track 1-2 of the fig. 1.3). On the contrary, if we remove the field from the Ferro–state, it will result in an opposite effect. On the other hand, the field applied adiabatically produces

¹⁸For instance, with the first patent for a vapor-compression refrigeration system obtained by Jacob Perkins in 1834.

¹⁹In fact, the Ferro–Para transition is defined as the Curie–Point.

larger temperature span as the field increases.



(a) Number of papers published annually.

(b) Number of citations per year.

Figure 1.4: The impact of the MCE is weighted over the past 44 years with through the publications containing the word “magnetocaloric” in the title, abstract, or among the keywords. The data are based on the values picked up from the Web of Knowledge where the blue bar values includes up to September 2013 and the yellow bar marks the year of the discovery of the Giant MCE in $Gd_5Si_2Ge_2$ —noticed by Pecharsky and Gschneidner, Jr., in 1997.

To sum up, it can be inferred that the more $\Delta M_{Curie-Point}$, the more MCE. In order to improve the MCE it is needed a higher jump in $\langle\Delta M\rangle$. This can be obtained through a discontinuous first-order transition in the vicinity of a second-order magnetic transition. In fact, is the *latent heat* from the structural transition which enhances the MCE to be *giant*. In addition, it is desirable that the material exhibits a reversible²⁰ MCE in order to harness the giant MCE for cooling refrigeration at room temperature. According to that, the discovery of the $Gd_5(Si_2Ge_2)$

²⁰Recovering the hysteresis with through an alternating magnetic field.

–with both large a magnetic entropy change and temperature change on applying a magnetic field– meant more than one publication, but a giant leap for MCE around room temperature. As follows from the fig. 1.4 on the facing page, the Pecharsky and Gschneidner paper [7] in 1997 broke through a milestone in MCE for potential cooling refrigeration.

Up to now, it has been dealing with ferromagnetism and paramagnetism in materials. Actually, we know about different types of magnetic order –ferromagnetism, antiferromagnetism, ferrimagnetism, and so on and so forth– in alloys formed by more than one element [37,38]. The key point in the Weiss model is that he –implicitly– stated that any solid which exhibits ferromagnetism becomes paramagnetic above the Curie-point. But the statement is equally applicable to solids that exhibiting any kind of magnetic-order will become paramagnetic above a certain temperature.

Nowadays, the need for high-efficiency devices and the reduction of energy consumption are two great goals for the world consumer society. Actually, the food preservation compels the society in the use of cooling devices which energetic efforts affects not only economy, but also for the well-being of citizens and to the detriment of the Earth –Kyoto protocol²¹. For example, 15% of the total worldwide energy consumption involves the use of refrigeration (air conditioning, refrigeration, freezing, etc.) [18]. In Fact, it has been indicated that a 1% improvement in efficiency would result in the savings of hundreds of millions of dollars and a reduction in CO_2 emissions of nearly 2.2 million metric tons of carbon equivalent [2]. In addition, it was demonstrated that magnetic refrigeration is a competitive technology in comparison with current cooling devices based on chemical hazardous and greenhouse gases, presenting potential energy savings of up to 30% [39]. From the aforementioned,

²¹The Kyoto Protocol legally binds developed countries to emission reduction targets. [8].

several authors state that these new magnetic materials will have a deep impact on the forthcoming eco-friendly technologies.

1.3 Magnetic Refrigeration

Previously to the paper of V. K. Pecharsky and K. A. Gschneidner, Jr, [7] a first breakthrough on magnetic refrigeration in the vicinity of room temperature was achieved by G.V. Brown in 1976 [10]. Prior to this, as mentioned above, there existed the generalized use of paramagnetic salts for magnetic refrigeration below 20 K for two reasons. First, at high temperatures the magnetic order of these materials is reduced as a consequence of the disorder effect of the thermal energy. Therefore, a higher magnetic field should be applied²² in order to obtain a similar *isothermal entropy change* as a result of the temperature increase. Secondly, as the temperature rises the heat capacity increases due to the lattice contribution [see eq. 1.2]. As a consequence, the *adiabatic temperature change* becomes insignificant for these materials at high temperatures [see fig. 1.3 where it is represented a sketch of the MCE proposal by Debye [27] and Giauque [5] in a paramagnetic salt].

However, it is well-known that the ordering effect of the $\langle\text{molecular field}\rangle$ ²³ –i.e., the exchange interaction [see section 1.7 for at-a-glance reference]– and the disordering effect of the *thermal energy* are approximately balanced near the *Curie* tem-

²²The maximum magnetic field strength is limited by the current technology. At the time of this writing the highest steady magnetic field is 45T, 100T sending brief-pulses (10 μ s) through them and, finally, 60T for long-pulses (100 ms) magnets [40].

²³Ferromagnetism and the Curie temperature were explained by Weiss in terms of an internal “molecular field” proportional to the magnetization [see section 1.2]. The theory is applicable to both localized and delocalized electrons. No such magnetic field really exists, but it is a useful way of approximating the effect [24].

perature. In this way, if the *Curie-point* takes place at high temperatures, then MCE can be used for magnetic refrigeration at temperatures above 20 K.

In fact, Brown found *gadolinium* to be a suitable candidate for magnetic refrigeration. Gd *Curie-point* takes place at 294 K²⁴ with $\Delta S_{ad} = -10.02 \text{ J/kgK}$ and $RCP^{25} = 410 \text{ J/kg}$ due to applying a 5-T field [39], seems made-to-order as the perfect nominee for the working material near room temperature. In addition, Gd presents a field dependence of the MCE $\sim 3 \text{ T/K}$ in low magnetic fields ($\leq 5\text{T}$) and falls to MCE $\sim 2 \text{ T/K}$ in high magnetic fields ($> 5\text{T}$), which give us an idea of the temperature span of the working material as the field rises. Here, indeed, it is shown how the MCE scales with the field.

According to the above, Brown built a refrigerating device working near room temperature using Gd as the working material. In his paper [10], Brown report that the application of a 7-T magnetic field to Gd at the Curie-point produced an *isothermal entropy change* of 4 J/kgK or an *adiabatic temperature change* of 14 K. He, indeed, attained a maximum temperature span²⁶ of 47 K²⁷ after 50 cycles, where the working material was immersed in 80% water-20% ethyl alcohol solution as a regenerator. The corresponding heat transfer was, indeed, stored in and withdrawn from the regenerator [18]. Following on from Brown, in 1982 Barclay and Steyert des-

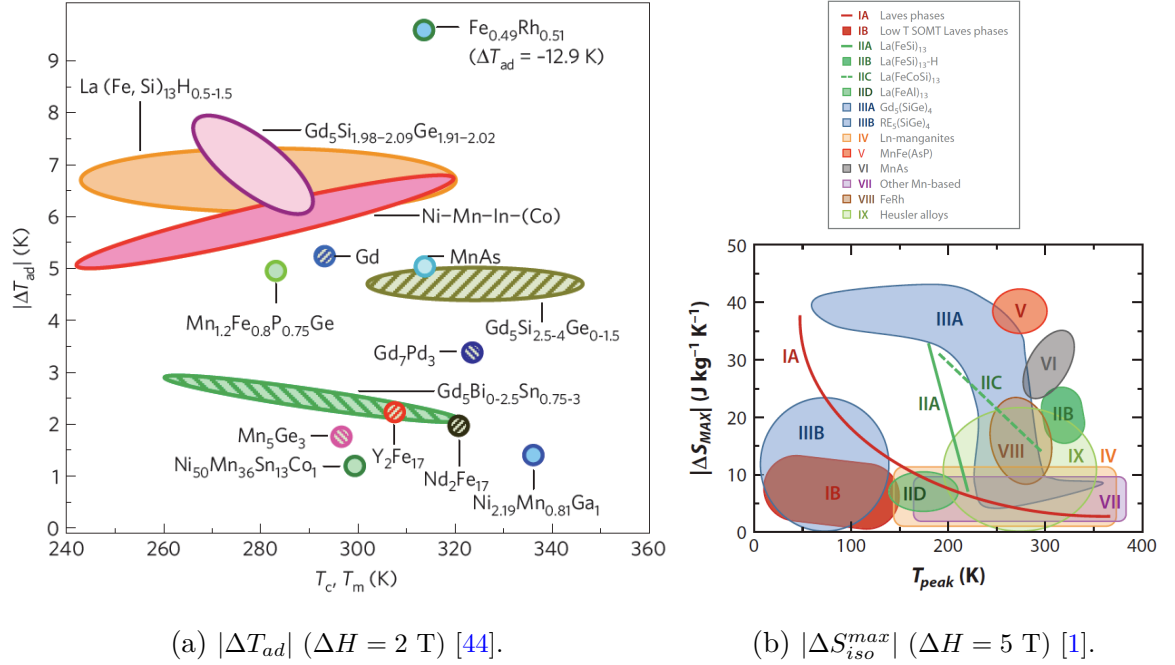
²⁴In fact, besides iron, cobalt and nickel, only gadolinium can be ferromagnetic at room temperature [24].

²⁵The relative cooling power (RCP), also known as refrigerant capacity (RC), quantifies the energy absorbed in a refrigerant cycle, and is defined as the amount of heat transferred between the hot and cold reservoirs. It is calculated as the product of the maximum $|\Delta S_M|$ peak value and the full width at half maximum, δT_{FWHM} [41].

²⁶The temperature span is measured from the hot end temperature, $T_{hot} = 319 \text{ K}$, to the cold end temperature, $T_{cold} = 272 \text{ K}$, in the refrigerator.

²⁷A temperature span that is three times bigger than the Gd maximum ΔT_{ad} value of 16 K at the Curie-point, 294 K.

cribed in their patent [42] the possibility to reach larger temperature spans than just ΔT_{ad} using the working material simultaneously as a regenerator and as the active magnetic component, which boosted the magnetic refrigeration with the appearance of an active magnetic regenerator (AMR) cycle²⁸.



(a) $|\Delta T_{ad}|$ ($\Delta H = 2$ T) [44].

(b) $|\Delta S_{iso}^{max}|$ ($\Delta H = 5$ T) [1].

Figure 1.5: In figure 1.5a, it is represented $|\Delta T_{ad}|$ ($\Delta H = 2$ T) for several ambient magnetic refrigerants at either a purely magnetic transition temperature T_c (second-order transition, marked by hatched pattern) or magnetostructural coupling transition temperature T_m (first-order transition, solid fill-pattern) [44]. In figure 1.5b, it is shown $|\Delta S_{iso}^{max}|$ ($\Delta H = 5$ T) versus peak temperature for different families of MCE materials [1].

²⁸In addition, there are several aspects in magnetic refrigeration that should keep in mind. For a summary about theoretical aspects –e.g., thermodynamics of the MCE–, the properties for selected MCE materials and so on, I recommend [43]. For instance, alternative processes for entropy change depending on the kind of cycle, e.g., Carnot cycle (two isothermal and two adiabatic processes), Ericsson cycle: two isothermal and two isofield processes, etc.

In 1998, MCE was revealed as a feasible technology when the Astronautics/Ames Lab. performed a magnetic refrigerator run “maintenance free” for over 1500 h. The demonstration showed significant cooling powers, 600 W²⁹, at high Carnot efficiencies, 60%³⁰, with a large coefficient of performance³¹, 15, and with a maximum temperature span of 38°C near room temperature in moderately strong magnetic fields (< 5 T) [45, 46].

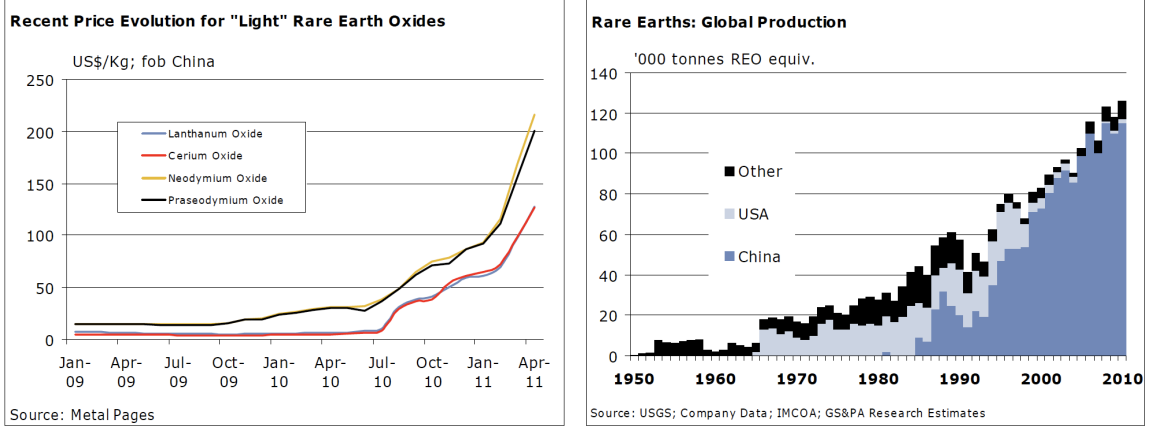
Besides above and bibliography [18, 47–49], it can be inferred that some of the best AMR are materials undergoing a second-order transition. Furthermore, the succession of several layers, which are constituted by different working materials with an increasing sequence of Curie temperatures, is clearly necessary to achieve a significant cooling span. Later on, it was reported the introduction of the $La(Fe_{0.88}Si_{0.12})_{13}H_{1.0}$ alloy, as an extra layer in the form of crushed powders, exhibiting a first-order magnetic transition through a 1.5 T Nd₂Fe₁₄B permanent magnet, which is suitable for domestic uses. For the latter magnetic refrigerator, the $La(Fe_{0.88}Si_{0.12})_{13}H_{1.0}$ was found as a promising MCE alloy with a first-order magnetic transition, although its usage will require a layered bed [50, 51].

Let’s make a break to quickly introduce that a variety of Gd-RE alloys, such as Tb, Dy, Ho, or Er, were prepared in order to improve the MCE in Gd. But, the results in the Curie temperature of Gd are just a shift to lower temperatures without any significant improvement in the MCE [53]. The Gd-Y alloying (such as Sb, Si, Sn), in contrast, gives rise to different behaviors. The Gd₅Si₄ and Gd₄Sb₃ alloys increase the T_C , but diminishes the MCE in both ΔS_{iso} and ΔT_{ad} . However, the Gd₅Sn₄

²⁹It is about 100 times greater than that obtained by previous near room temperature magnetic refrigerators [45].

³⁰The best gas-compression refrigerators exhibit only about 40% [11].

³¹The coefficient of performance (COP) is the cooling power divided by the input work. The typical vapor cycle in refrigerators have a COP between 2 and 6 [45].



(a) Price evolution in RE .

(b) Evolution of the global production in RE .

Figure 1.6: Time evolution of both global production and price in Rare-Earth [52].

alloy increases its ΔS_{iso} , but at the expense of a lower T_C [39]. Consequently, as mentioned previously in section 1.2, in 1997 the Pecharsky and Gschneidner paper [7] boosted MCE near room temperature for magnetic refrigeration. Since then, several other families have appeared exhibiting giant MCE near room temperature. These include $MnAs_{1-x}Sb_x$ (Wada and Tanabe, 2001) [54] [labelled within MnAs as VI in fig. 1.5b], $La(Fe_{1-x}Si_x)_{13}$ (Hu et al., 2001) [55] [labelled as IIA in fig. 1.5b] and their hydrides (Fujita et al., 2003) [56] [labelled as IIB in fig. 1.5b], $MnFeP_{1-x}As_x$ (Tegus et al., 2002) [57] [labelled as V in fig. 1.5b], $Ni_{2+x}Mn_{1-x}Ga$ (J.Marcos et al., 2003) [58] [labelled within Heusler alloys as IX in fig. 1.5b], $Ni_{0.50}Mn_{0.50-x}Sn_x$ (Krenke et al., 2005) [59] [labelled within Heusler alloys as IX in fig. 1.5b], and the $MnCoGeB_x$ alloys (Trung et al., 2010) [60] [labelled within Other Mn-based as VII in fig. 1.5b], among other families. In figure 1.5, it is represented $|\Delta S_{iso}|$ [see fig. 1.5b³²] and $|\Delta T_{ad}|$ [see fig. 1.5a], as a function of the transition temperature,

³²Laves phases, with stoichiometry A-B2 (space group Fd3m), crystallize in three types of structures, but the interesting for MCE is the cubic MgCu2-type phase, with A an RE metals, and B

in a summary of selected MCE materials for magnetic refrigeration. Nevertheless, despite the advantages offered by giant MCE materials, they present three main problems resulting from the nature of their first-order magnetostructural transition that should be solved: (1) a large volume change, (2) hysteresis, and (3) the delay to reach a maximum equilibrium value of ΔT_{ad} on applying magnetic field.

Finally, it is important to keep in mind the price for the magnetic refrigerant components. In figure 1.6a, shows the increasing price evolution of four representative RE³³, which are crucial compounds for magnetic refrigeration. On 2011, an investment research of Goldman Sachs & Partners Australia [52] reported that the annual global demand was 130000 tonnes, and supply was dominated by China, which currently accounts for more than 95% of global production [see figure 1.6b]. The mentioned report [52] points out that China's government had reduced export quotas since 2006. In addition, it is worth noting that V.K.Pecharsky et al. [62] reported large interstitial impurities, specially in a sample from The Peoples' Republic of China³⁴, causing some erroneous results in the MCE and lowering the Curie-point.

To sum up, the future looks bright for magnetic refrigeration but there are still a number of challenges to overcome. First, improved engineering to overcome the limitations of the currently available working materials. Secondly, the increase of the magnetic field strength of the permanent magnets while reducing the size, mass and its cost [18]. Further efforts should be focused to enhance the magnetic refrige-

mainly a transition metal.

³³Cerium, Lanthanum and Neodymium are the three RE elements of highest demand, but not the more expensive ones [52]. Here is presented the Rhodium, Rh, which in 1997 was already prohibitively expensive 120000\$/kg in comparison to 120\$/kg for Gd [61].

³⁴A chemical analysis, carried out at the Ames Laboratory on a typical commercial standard purity polycrystalline sample, showed that the claimed purity of 99.9 wt.% was approximately correct, but when one considers the purity on an atomic basis, it was only 93.1 at % pure [62].

ration with the ultimate improvements in the different caloric effects that have been unraveled [12–16].

1.4 The Heusler alloys: prototypical Functional materials

Heusler alloys³⁵ are defined as ternary intermetallic compounds generally described by means of two distinct families: one with the XYZ formula –the so-called *half-Heusler* alloys– and composition 1 : 1 : 1, and the other one with X_2YZ formula –the *full-Heusler* alloys– and 2 : 1 : 1 stoichiometry³⁶. These alloys bear the name of Fritz Heusler who in 1903 observed magnetic properties in $CuMn$ -based alloys which are indeed formed by non-magnetic elements [65, 66]. For example, neither of the constituent elements Cu , nor Mn and Al is magnetic, but the resulting Cu_2MnAl Heusler alloy is ferromagnetic. Hence, here appears the special feature of the Heusler alloys which final alloy properties differ completely from the originally combined elements. Actually, they are a group of more than 1000 compounds with endless possibilities of combination, which are shown in fig. 1.7 by means of a colored code. X and Y are usually transition metals and Z is, generally, a IIIA-VA element. Furthermore, we should note that in our notation, the X element is the most electropositive of the three elements –i.e., the element who transfers its valence electrons–, Z, the most electronegative and Y, somewhere in the middle.

³⁵For sure it is more accurate to say Heusler compounds rather than Heusler alloys, because the constituents can not be separated by any mechanical procedure. But for historical reasons, hereafter, it will be used the latter.

³⁶For further information about current Heusler alloy topic I recommend the refs. [63, 64], which describe in detail the structure and properties of the Heusler alloys.

X_2YZ Heusler compounds

H 2.20																	He	
Li 0.98	Be 1.57											B 2.04	C 2.55	N 3.04	O 3.44	F 3.98	Ne	
Na 0.93	Mg 1.31											Al 1.61	Si 1.90	P 2.19	S 2.58	Cl 3.16	Ar	
K 0.82	Ca 1.00	Sc 1.36	Ti 1.54	V 1.63	Cr 1.66	Mn 1.55	Fe 1.83	Co 1.88	Ni 1.91	Cu 1.90	Zn 1.65	Ga 1.81	Ge 2.01	As 2.18	Se 2.55	Br 2.96	Kr 3.00	
Rb 0.82	Sr 0.95	Y 1.22	Zr 1.33	Nb 1.60	Mo 2.16	Tc 1.90	Ru 2.20	Rh 2.28	Pd 2.20	Ag 1.93	Cd 1.69	In 1.78	Sn 1.96	Sb 2.05	Te 2.10	I 2.66	Xe 2.60	
Cs 0.79	Ba 0.89			Hf 1.30	Ta 1.50	W 1.70	Re 1.90	Os 2.20	Ir 2.20	Pt 2.20	Au 2.40	Hg 1.90	Tl 1.80	Pb 1.80	Bi 1.90	Po 2.00	At 2.20	Rn
Fr 0.70	Ra 0.90																	
		La 1.10	Ce 1.12	Pr 1.13	Nd 1.14	Pm 1.13	Sm 1.17	Eu 1.20	Gd 1.20	Tb 1.10	Dy 1.22	Ho 1.23	Er 1.24	Tm 1.25	Yb 1.10	Lu 1.27		
		Ac 1.10	Th 1.30	Pa 1.50	U 1.70	Np 1.30	Pu 1.28	Am 1.13	Cm 1.28	Bk 1.30	Cf 1.30	Es 1.30	Fm 1.30	Md 1.30	No 1.30	Lr 1.30		

Figure 1.7: Periodic table of elements where the colored elements reveal the possible combination of both Heusler alloys: XYZ –*half-Heusler*– and X_2YZ –*full-Heusler* alloys. Below the element symbol appears the Pauling electronegativity [64].

Today, we are all aware of the strong interplay between the properties of Heusler alloys and the atomic order. Therefore, a deep knowledge and an accurate study of their crystal structure is fundamental to understand the structure-to-property relation for the subsequent Heusler alloy design [67–70]. A common feature for both families is that they are based on a bcc structure, which consists of four interpenetrating fcc sublattices. As for the X_2YZ alloys, all four sublattices are completed, but one of them is empty in XYZ alloys. In the former case, these alloys occupy the crystallography non-equivalent Wyckoff positions $8c(1/4, 1/4, 1/4)$ for X, $4b(1/2, 1/2, 1/2)$ for Y and $4a(0, 0, 0)$ for Z. In the latter case, each one of the corresponding three interpenetrating fcc sublattices are occupied by the X, Y and Z, which are located in the non-equivalent Wyckoff positions at $4b(1/2, 1/2, 1/2)$,

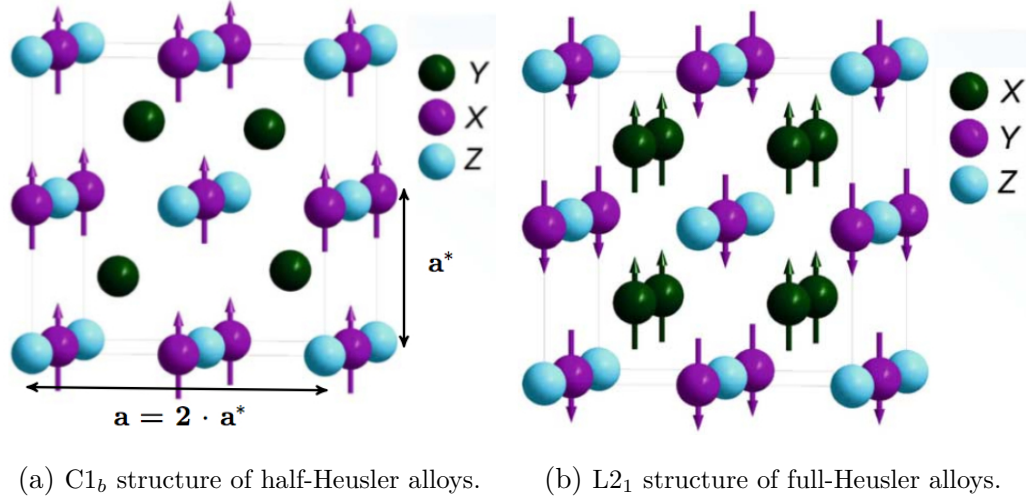


Figure 1.8: Crystal structure of half-Heusler (left) and full-Heusler alloys (right) exhibiting one magnetic sublattice, and two magnetic sublattice, respectively [71].

$4c(1/4, 1/4, 1/4)$ and $4a(0, 0, 0)$, respectively [63]. So far, for a common description in both *half* and *full*-Heusler structures, we adapt the notation to the next Wyckoff position $4c(1/4, 1/4, 1/4)$ for X, $4d(3/4, 3/4, 3/4)$ for X', $4b(1/2, 1/2, 1/2)$ for Y and, finally, $4a(0, 0, 0)$ for Z —which fully takes into account the four interpenetrating sublattices³⁷.

Figure 1.8 shows the $C1_b$ structure of *half*-Heusler alloys [fig. 1.8a] and the $L2_1$ structure of *full*-Heusler alloys [fig. 1.8b]. These structures are based on the zincblende structure (ZnS), from which all Heusler alloys can be decomposed into a ZnS-type substructure [see table 1.1], but with variations in the occupancy of the interstitial lattice sites [71]. In contrast to *half*-Heusler alloys, which magnetic moments are localized on the octahedral –ionic– sites in one of the *fcc* sublattice, i.e., the $4b$ -X sublattice [see fig. 1.8a], the X_2YZ presents two magnetic sublattices in

³⁷In the particular case of the *half*-Heusler alloys, the X' ($4d$) sublattice is empty (see fig. 1.8).

Table 1.1: Site occupancy and general formula for different atomic orders of Heusler alloys, represented with respect to the prototype material in the Inorganic Crystal Structure Database (ICSD), the structure and superstructure (S), atoms per unit cell (Z), the Pearson database and the Space group [24, 63, 64].

Site occupancy	Formula	Prototype	S	Z	Pearson	Space group
4c, 4b, 4a	XYZ	LiAlSi	fcc- $C1_b$	12	cF16	$F\bar{4}3m$ (No. 216)
4c, 4b=4a	XZ_2	CaF ₂	fcc-C1	12	cF12	$Fm\bar{3}m$ (No. 225)
4d=4c, 4b, 4a	X_2YZ	Cu ₂ MnAl	fcc-L2 ₁	16	cF16	$Fm\bar{3}m$ (No. 225)
4d, 4c=4b, 4a	XY_2Z	CuHg ₂ Ti	fcc-X	16	cF16	$F\bar{4}3m$ (No. 216)
4d, 4c, 4b, 4a	$XX'YZ$	LiMgPdSn	fcc-Y	16	cF16	$F\bar{4}3m$ (No. 216)
4b=4c=4d, 4a	X_3Z	BiF ₃	bcc-DO ₃	16	cF16	$Fm\bar{3}m$ (No. 225)
4d=4c, 4b=4a	X_2Z_2	CsCl	bcc-B2	2	cP2	$Pm\bar{3}m$ (No. 221)
4d=4c=4b=4a	X_4	W	bcc-A2	2	cI2	$Im\bar{3}m$ (No. 229)

the L2₁ structure. One sublattice, which formed by the 4c-X and the 4d-X', fills all the tetrahedral -covalent- sites in the strongly localized magnetic sublattice, and the 4b-Y fills the octahedral -ionic- sites in the second magnetic sublattice [see fig. 1.8b]. Thus, depending on the atomic order different Heusler alloys might emerge based on both crystal structure and magnetic phenomena.

The stability of Heusler alloys could be explained through electron counting rules [71, 72]. In fact, most *half*-Heusler alloys with a number of valence electrons different from 18, $\langle N_V \neq 18 \rangle$, do not crystallize in a $C1_b$ structure because of the formation of an extra magnetic sublattice that destabilizes the cubic structure -i.e.,

it is said that XYZ has a closed electron shell configuration for $\ll N_V = 18 \gg$. For instance, the CoMnSb alloy crystallizes in a different structure-type with more than one magnetic lattice site [73]. Thus, *Half*-Heusler alloys become stable through a closed shell configuration, when the valence atomic orbitals of X become void for the sake of a close configuration of $\ll d^{10} \gg$ and $\ll s^2 p^6 \gg$ orbitals for Y and Z, respectively. But, indeed, they do have exceptions to the $\ll 18\text{-electron-rule} \gg$. The known exception is the MnYSb –with Y=Ni, Pd and Pt– family of alloys. For example, following the “18–electron–rule” for the MnNiSb alloy, the valence electrons count sums up to $N_V = 22$, with $Mn^{+3} (d^4)$, $Ni^0 (d^{10})$ and $Sb^{-3} (s^2 p^6)$. Here, indeed, is reflected the crucial role of X in *half*-Heusler alloys. The possible answer for that alloy to crystallize in a $C1_b$ structure is related to the strongly localized nature of the 3d electrons when X=Mn.

In the same vein, it was found that –as in the $\ll 18\text{-electron-rule} \gg$ for *half*-Heusler with the $C1_b$ structure– the close electron shell configuration for the *full*-Heusler alloys is $\ll N_V = 24 \gg$, but with the $L2_1$ structure³⁸.

So, for a disclosed electron shell configuration –i.e., $\ll N_V \neq 24 \gg$ – a new magnetic sublattice emerges to interact with the strong localized magnetic sublattice occupying the tetrahedral sites ($4c$ and $4d$), which results in a diverse kind of magnetic behaviors in the *full*-Heusler alloys³⁹, i.e., ferromagnetism, ferrimagnetism, antiferromagnetism (NiMn-based alloys) and half-metallicity (Co₂TiZ Heusler alloys, with Z= Al, Si, Ge, Sn)⁴⁰ [64, 71]. A brief summary of the different structure-types in Heusler alloys

³⁸In fact, the $L2_1$ structure is stable for all the *full-Heusler* alloys at high temperatures. At low temperatures, if the $L2_1$ structure becomes unstable, then some of them undergo a structural transformation –i.e., a martensitic transformation [see section 1.5].

³⁹Due to the important role of the atomic order–disorder phenomena to the Heusler properties –especially the magnetic ones– are pretty sensitive to the heat treatments [69, 74].

⁴⁰Half-metal materials are those materials characterized by a very small overlap between the

are presented in table 1.1.

In addition to the structures mentioned above, there also exist two interesting structures regarding the atomic order. On the one hand, the *inverse* Heusler structure basically appears when two elements from the same period satisfy: $Z(Y) > Z(X)$, where $\llbracket Z(\text{element}) \rrbracket$ is the atomic number. The structure is still a four interpenetrating *fcc* sublattices. But the Y atoms are now placed on the Wyckoff positions $4c(1/4, 1/4, 1/4)$ and $4b(1/2, 1/2, 1/2)$, while the X and Z atoms are located at $4d(3/4, 3/4, 3/4)$ and $4a(0, 0, 0)$, respectively. CuHg_2Ti is the prototype of this structure and in Mn_2 -based materials is frequently observed. On the other hand, the *quaternary* Heusler alloys –with composition 1 : 1 : 1 : 1– are constituted by four different elements: Z, Y, X and X', which are located at $4a$, $4b$, $4c$ and $4d$, respectively [76, 77].

Besides the great tunability of the Heusler alloys, low toxicity –i.e., Sb is an exception– and low price. We should add the vast functionality⁴¹ that these materials exhibit ranging from Magneto-Optical properties (light polarization by Kerr's effect, e.g., the MnPtSb *half*-Heusler), Magnetocaloric effects [21], Shape-Memory [78, 79], Superconductors (e.g., LaPtBi as a multifunctional material because is also semiconductor), Topological Insulators (e.g., LuPtSb) and so on and so forth. In addition, one has to take into account the multifunctional possibility of such alloys (e.g., LaPtBi as both semiconductor and superconductor. The observed effects in NiMn-Based alloys such as MCE, exchange-bias, giant magneto-resistance). Hence, here remains the ever-increasing interest in Heusler alloys in the long way forthcoming.

bottom of the conduction band and the top of the valence band [75].

⁴¹Functional materials are those materials that exhibit an important physical response (mechanic, electric or magnetic) in consequence of an external stimulus (temperature, stress, magnetic field, or any other external field).

1.5 The Martensitic Transformation: a First-Order Structural Transformation

Among the two Heusler families mentioned before, in the present thesis an important effort has been centered on a singular branch of full-Heusler alloys, the Ni₂Mn-based alloys. Today martensitic transformation is revealed at appropriate off-stoichiometric compositions for any of the Ni₂Mn-Z alloys (with Z = Ga⁴², Sn, In, Sb). A vast quantity of interesting properties arise from the magneto-structural/elastic interplay ranging from the field-induced strains [81], caloric effects [see section 1.1] [12, 13], magnetoresistance [82, 83], exchange-bias [84] and so on.

Over the years, many Heusler alloys have been found undergoing *Martensitic* transformation⁴³ when the alloy is cooled down to a characteristic transition temperature –i.e., the Martensite-start temperature (M_s). At this point (M_s), the high-temperature cubic L2₁ structure transforms to a low-temperature with tetragonal L1₀ or modulated monoclinic/orthorhombic phases. The high-temperature solid-state L2₁ phase –or parent phase– is named *austenite*, while the low-temperature solid-state phase is named *martensite* [in fig. 1.9 are represented the austenite structure and the different modulated structures of martensites]. So far, *Martensitic* transformations⁴⁴ (MT) are nowadays defined as solid-state first-order structural phase transformations (FOST) that are displacive –therefore diffusionless– and dominated

⁴²Ni-Mn-Ga is the only NiMn-based alloy with the exact 2-1-1 stoichiometry that undergoes a MT [80].

⁴³For the sake of clarity, hereafter, a structural phase transition will be referred to as a phase «*transformation*» and, on the other hand, the term «*transition*» will be used for the rest of the phase transitions.

⁴⁴In fact, not only Heusler alloys, but also a wide variety of materials suffer a martensitic transformation –e.g., non-ferrous alloys, ceramics, inorganic compounds [85].

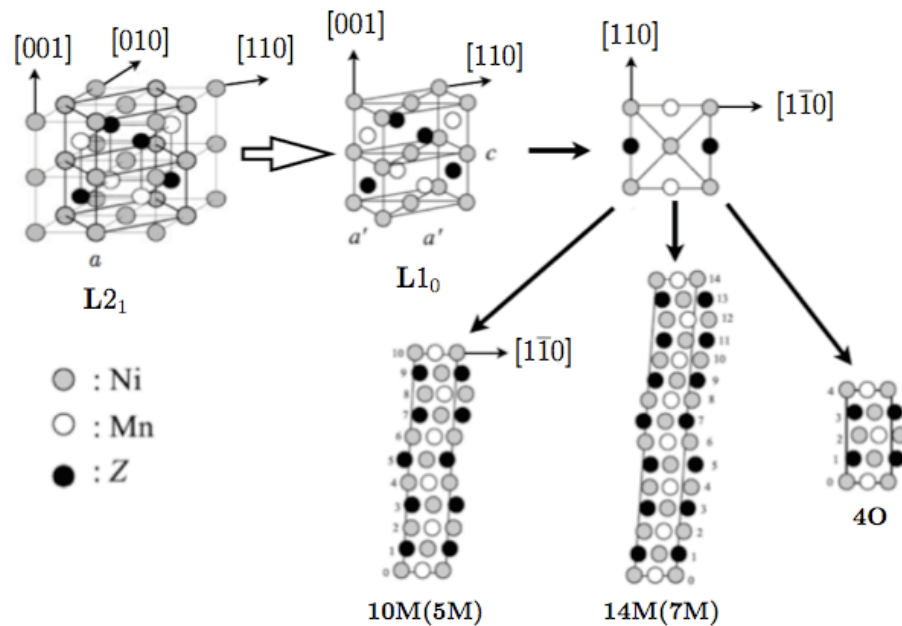


Figure 1.9: Austenite ($L2_1$) and non-modulated ($L1_0$)/modulated [$10M$ ($5M$), $14M$ ($7M$) monoclinic and $4O$ orthorhombic] martensite structures of $Ni_{50}Mn_{50-x}Z_x$ (Z : Ga, In, Sn and Sb) alloys. The tetragonal non-modulated unit cell with lattice parameters $a'(<a)$ and $c(>a')$ becomes modulated by shearing the (110) planes along the $[1\bar{1}0]$ direction.

by a shear-like behavior [see fig. 1.9] which is produced by means of nucleation and growth [86].

Figure 1.9 shows the lattice correspondence between the $L2_1$ cubic axes and those for the $L1_0$ tetragonal structure [67]. In addition, figure 1.9 displays how modulated martensitic phases are originated by shearing the (110) planes of the non-modulated $L1_0$ phase along the $[1\bar{1}0]$ direction.

Typically, the martensitic transition is preceded by precursor effects. On cooling, the austenite phase becomes *soft* for shear distortions on $\{110\}$ planes along $\langle 1\bar{1}0 \rangle$ direction. Curiously, these are the planes that show lattice instabilities in NiMn-

based single-crystals. This behavior is observed by ultrasonic and inelastic neutron scattering experiments that show low values of the elastic constant C' and in the energy of the TA_2 phonon branch, in consequence of weak restoring forces in the high-temperature phase [87]. The latter reflects that the MT is consequence of the strain-energy that arises from shear-like displacements [78].

Figure 1.10 shows the phase diagram in the off-stoichiometric Ni–Mn–Z Heusler alloys for (a) Ni–Mn–Ga⁴⁵, (b) Ni₅₀Mn_{50-x}In_x, (c) Ni₅₀Mn_{50-x}Sn_x and (d) Ni₅₀Mn_{50-x}Sb_x. The magnetic transition and the structural (M_S) temperatures are plotted as a function of the valence electron concentration per atom, i.e., $\langle\langle e/a \rangle\rangle$ ⁴⁶. Besides the slope growth in the martensitic start temperature (M_S) ranging from Ni–Mn–Ga to Ni₅₀Mn_{50-x}Sb_x alloys, the M_S increases almost linearly by increasing the $\langle\langle e/a \rangle\rangle$, at the expense of the $\langle\langle x \rangle\rangle$ element concentration, in all the alloys. Here the $\langle\langle e/a \rangle\rangle$ concentration is critic for the M_S . For instance, M.Acet et al. [79] noticed that a 0.1 $\langle\langle e/a \rangle\rangle$ reduction for both Ga and Sb, which corresponds to a negative change of about 5 and 2 at %, shows a rapid decrease in the M_S of about 80 K and 270 K, respectively. This gives an idea of the difficulties in designing samples with desired properties [79].

On the other hand, T_C^A and T_C^M are the Curie temperatures of the austenite and martensite phases, respectively. Above T_C^A all the alloys are paramagnetic (PM). In contrast to M_S , the T_C^A presents a slow increasing as Z rises, ranging from Ga to Sb. On the contrary, $\langle\langle e/a \rangle\rangle$ concentration is again critic for the T_C^M , which suffers a rapid

⁴⁵The scattering of the Ni–Mn–Ga data is consequence of a data collected with no constraints in the composition of any of its components. In addition, the data for Z as In, Sn and Sb have a constant Ni composition of 50 at %.

⁴⁶ $\langle\langle e/a \rangle\rangle$ is calculated as the concentration-weighted-average of the $\langle\langle s \rangle\rangle$ and $\langle\langle d \rangle\rangle$ electrons for the transition elements, and the $\langle\langle s \rangle\rangle$ and $\langle\langle p \rangle\rangle$ valence electrons for the group **IIIA-VA** elements.

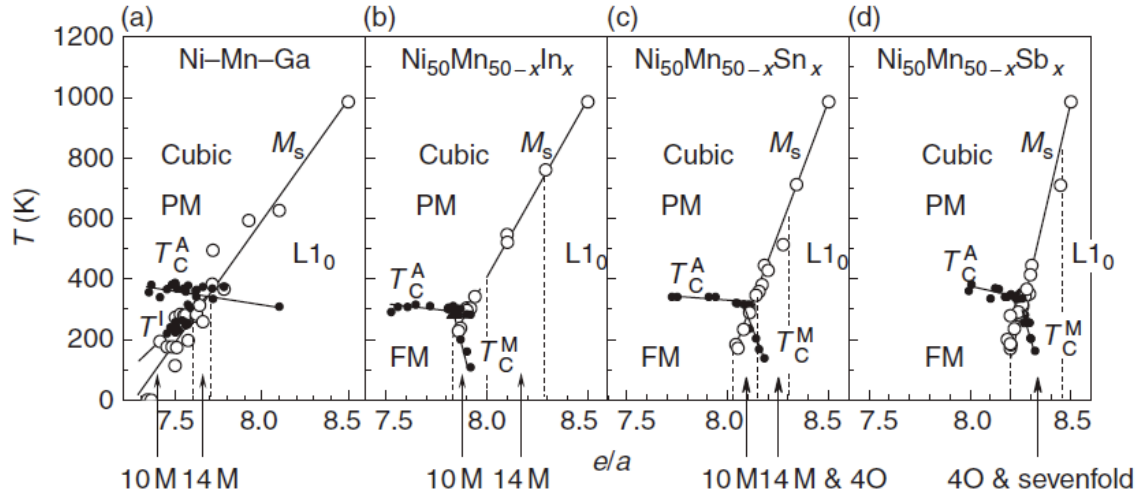
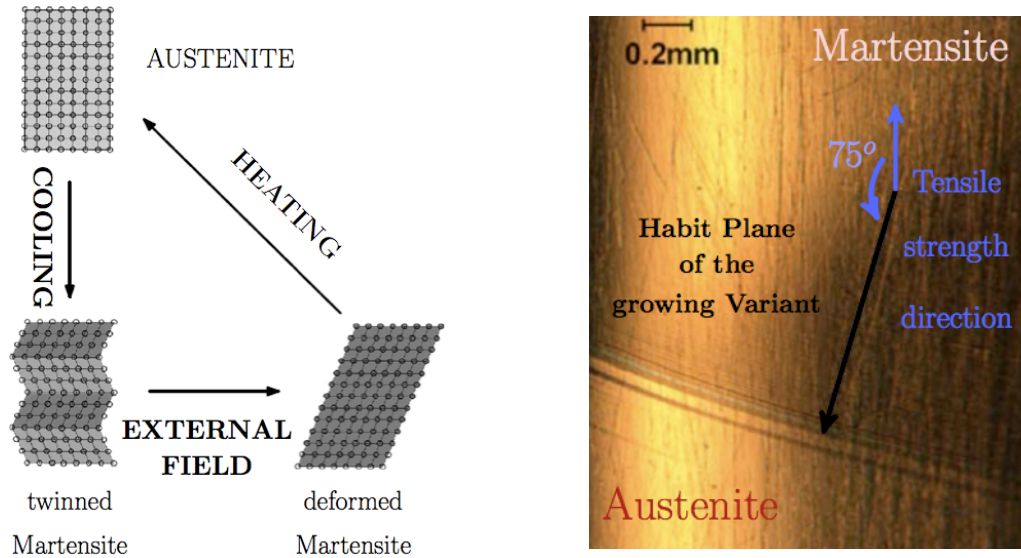


Figure 1.10: Magnetic and structural phase diagram of Ni–Mn–Z with Z as (a) Ga, (b) In, (c) Sn and (d) Sb. The filled and open circles correspond to the magnetic and martensitic transformation temperatures, respectively. The crystal structure changes with composition and the regions related to the different structures are separated by dashed lines [79, 88].

decrease as $\langle e/a \rangle$ rises [21, 79, 88]. The latter can be explained through a lowering in the ferro–magnetic (FM) coupling as a result of a strong anti–ferromagnetic (AF) exchange between Mn–Mn nearest neighbors in the martensite phase. However, in the austenite phase, the FM exchange is strong enough and the $\langle e/a \rangle$ is not as crucial as for both T_C^M and M_S [89].

At room temperature, figure 1.10 [(a)→(c)] essentially presents the following **cubic**→**10M**→**14M**→**L10** structure evolution for a $\langle e/a \rangle$ increasing. But Sb–(d) alloy follows the next sequence **cubic**→**4O**–**7fold(mixture)**→**L10**. **4O** modulated structure is also found in the Sn–(c) alloy. It is worth noting that the martensite window becomes narrow as Z increases. Finally, in figure 1.10 (a) –for the NiMnGa– appears a linear T_I with the $\langle e/a \rangle$, that stands for the premartensitic transition temperatures.



(a) MT is consequence of the strain-energy that arises from shear-like displacements. (b) Martensite propagation in a Cu-Zn-Al single crystal resulting from a tensile strength [90].

Figure 1.11: (a) displays a sketch of the shearing atomic displacements that lies beneath the martensitic transformation (an insight in Shape-memory effects can be found in [21]). (b) shows a real picture on a Cu-Zn-Al single crystal undergoing a MT due to an external tensile force.

With respect to the MT, as a consequence of an external applied field, the subsequent growth of the new phase –once nucleation starts– is perpendicular to the invariant plane at the interface, i.e., the *Habit plane* [see figs. 1.11b and 1.15] [90,91].

In fact, immediately after of being transformed and in order to minimize the *strain-energy* of the variants, the strain can be accommodated by the reversal of some of the variants into new ones. There are two ways to minimize the *strain-energy*, either by introducing *slip* or by introducing *twins*. Herein, we are going to attach the *twin* solution because of the critical strength that is need to overcome the shape-memory range, i.e., the *slip* range, causes the loss of the shape-memory

properties in the alloy [78]. Then, *twinning* [see fig. 1.11a] is the mechanism that explains the re-accommodation of the different martensite *variants* [92].

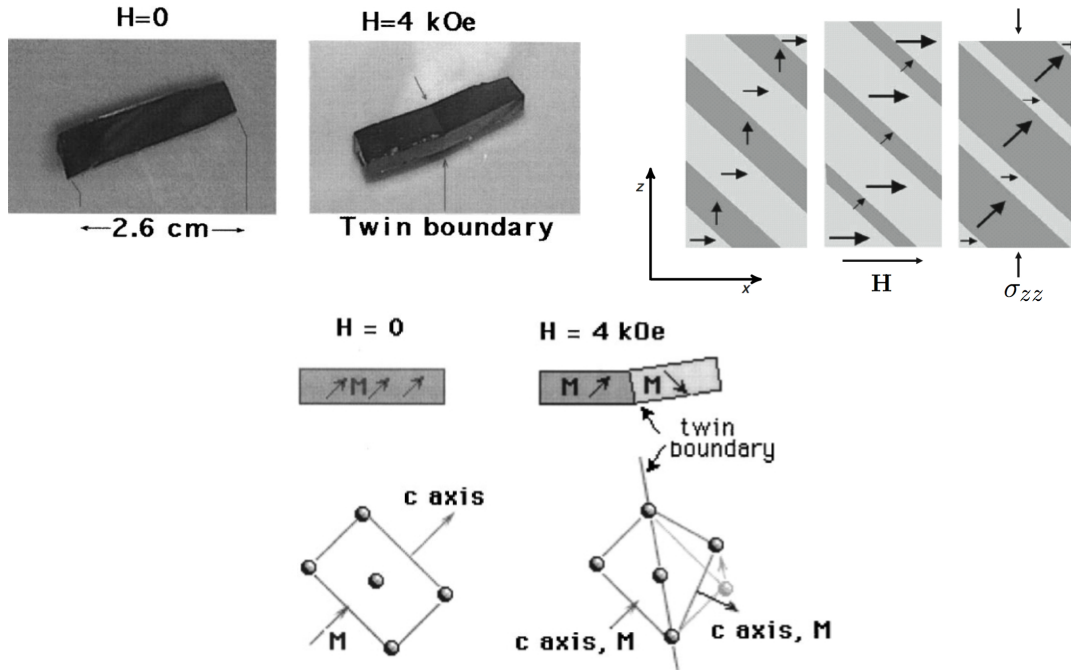
In fig. 1.11b an externally applied tensile strength in a Cu-Zn-Al single crystal clearly shows the progress of the martensite variant through the mobility of the *Habit plane* –which is pointed by a black arrow– at the expense of the parent-phase. The forward transformation from the single crystal parent-phase towards a symmetry lowering enables the possibility of different orientations or *twin variants* within the martensite, but in the absence of any external stress.

On the other hand, due to a magneto-structural interplay the application of an external magnetic field on the low-temperature martensite phase produces a twin-variant reorientation promoting the growth of one variant at the expense of unfavorably oriented twin variants (see fig. 1.12b). In fig. 1.12a is observed the aforementioned formation of a twin-boundary induced by the application of 4 KOe in a single martensite variant of NiMnGa and, in fig. 1.12c, the subsequent accommodation of the new variant minimizing its *strain-energy* through the rearrangement of the atoms at the interface [93].

Lately, it has been pointed out that the different modulated structures in the martensite phase [67,68] can be explained as *adaptive* intermartensitic –metastable– phases within the martensite and constructed from nanotwinned variants of the tetragonal $L1_0$ martensite phase [94]. In addition, they are stacked in order to minimize its strain-energy during the nucleation. Here, once again we remark that in $Ni_2Mn_{1-x}Z_x$ alloys not only the temperature, but also the $\langle\langle e/a \rangle\rangle$ and the amount at % of Z in the composition ($\langle\langle x \rangle\rangle$) are crucial for the crystal structure and, therefore, for the lattice parameter, which finally involves the neighboring magnetic interaction [see fig. 1.10]. Finally, it can be pointed out as a recipe that for high $\langle\langle e/a \rangle\rangle$ –low $\langle\langle x \rangle\rangle$ – the austenite transforms to a $L1_0$. On the other hand, for low $\langle\langle e/a \rangle\rangle$ –high

« x »— shows the onset of the martensite modulated structures [21, 95, 96].

- (a) A twin-boundary kink (right) appears in a single martensite variant (left) of NiMnGa at room temperature due to an externally magnetic applied field [93].
- (b) Twin-variant reorientation at the expense of the unfavourables as a result of an external applied field, e.g., a magnetic field and stress [79].



- (c) At the top, a sketch of (a) showing the two different direction of magnetization in the two martensite variants. The orientation of the martensitic unit cell (left) and the twinned martensitic cell (right) are represented at the bottom [93].

Figure 1.12: Shape-memory effects.

Figure 1.13 shows the transition point at T_0 between the two structural phases through a Gibbs⁴⁷ energy balance. However, actually, experiments exhibit a non-fixed transition point. Thus, depending on the temperature cooling or heating rate,

⁴⁷The Gibbs energy, $G(T, p)$, can be described as follows « $G = H + S \cdot T$ », in terms of the

whether in the forward or in the reverse transformation, there is observed an overcooling (in blue) in the forward transformation –overheating (in red) in the reverse–, which gives rise to thermal hysteresis [see fig. 1.13]. So, there should be a further interaction between the phases than the pure chemical (CH), i.e., the aforementioned *strain–energy*.

The driving force $-\Delta G_{CH}$ arises from the imbalance produced by an external field between the parent–phase and the martensite, which is defined as follows:

$$\Delta G_{balance}^{MT} = \Delta G_{CH} + \Delta E_{NC} = 0 \quad (1.3)$$

$$\begin{cases} (G_f^M + \Delta E_{NC}) - G_f^A = G_{M_S}^{A \rightarrow M} + \Delta E_{NC}^{forward} = 0, & \text{forward} \\ (G_r^A + \Delta E_{NC}) - G_r^M = G_{A_S}^{M \rightarrow A} + \Delta E_{NC}^{reverse} = 0, & \text{reverse} \end{cases} \quad (1.4)$$

where the term $\langle \Delta E_{NC} \rangle$ ⁴⁸ includes not only the *strain–energy*, but also a *dissipative* term that originates the energy loss as a result of friction in grain boundaries and in crystallographic defects. The former *strain–energy* oppose the forward transformation increasing the $\langle G_{balance}^M \rangle$ (in blue), which results in overcooling in the forward transformation –overheating in the reverse [see fig. 1.13]. But, indeed, remains stored in the martensite phase in order to promote the reverse transformation. This is true, up to the point that the reverse transformation can take place at temperatures below T_0 [this third possibility is displayed in green in fig. 1.13, which results in a $\langle A_s^{overcooled} \rangle$]. On the other hand, the *dissipative* energy always opposes the martensite transformation. Therefore, there arises a competition between both

enthalpy, H , the entropy, S , and the temperature, T . With the aim of giving an idea of the amount of available energy of the system in order to harness its potential. Thus, the Gibbs energy provides the balance concept between two different phases.

⁴⁸Non-chemical change in energy.

the *strain* and the *dissipative* energy, which are represented by the term $\langle\Delta E_{NC}\rangle$ in eqs. 1.3 and 1.4.

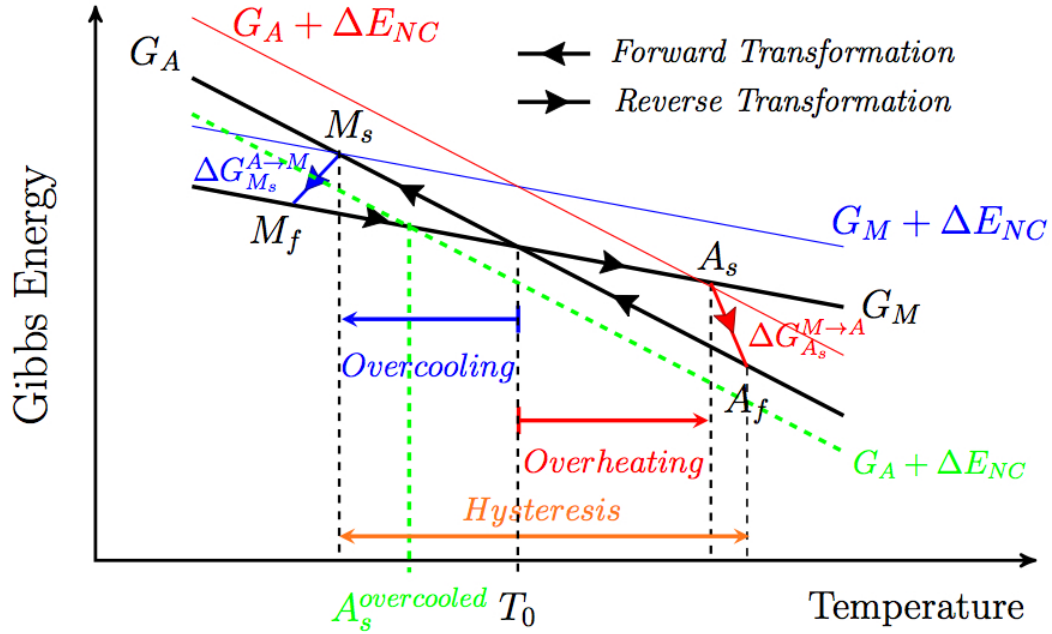


Figure 1.13: Schematic representation of the Gibbs free energy in the forward and in the reverse martensitic transformation. Further information is explained within the text.

In the forward transformation both the *strain* and the *dissipative* energy opposes the transformation ($\langle\Delta E_{NC} > 0\rangle$), which in practice results in overcooling to reach the $\langle M_s \rangle$ through the overcoming of a higher energetic barrier [in blue in fig. 1.13]. On the other hand, in the reverse transformation, the *strain* energy promotes the transformation and, therefore, the *dissipative* term opposes to the austenite formation. Herein arises a competition between both energies. So, if the *dissipative* term prevails, then $\langle\Delta E_{NC} > 0\rangle$ resulting in overheating [in red in fig. 1.13]. But if prevails the *strain* term, then $\langle\Delta E_{NC} < 0\rangle$, and results that the reverse transformation

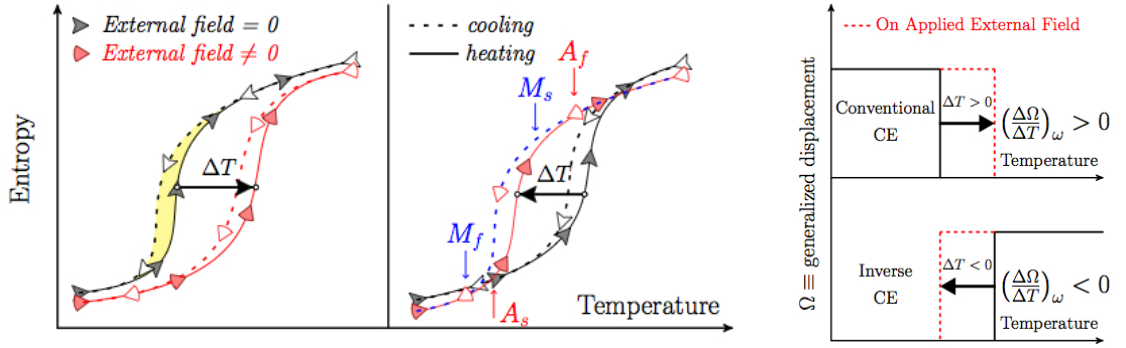
undergoes at temperatures below T_0 [in green in fig. 1.13].

When the *strain–energy* prevails over the *dissipative* term, the MT can be classified as a *burst* transformation. These transformations are characterized by a small temperature range, with a broad hysteresis —e.g., hundreds of degrees for Fe70–Ni [97]. In fact, due to its high strain–energies there gives rise to a critical size above which the interface is paralyzed. So, the transition requires the re–nucleation of a new phase to be fulfilled, which contributes to the high hysteresis.

In contrast to the previous one, *thermoelastic* transformations present an almost negligible change in volume [13,98]. They are therefore more reversible than the *burst* –, i.e., upon removal of the external field, the recover amount is more important in the *thermoelastic* than in the *burst* transformations (the reverse transition is easiest to recover)–, and shows a higher mobility in the *habit plane* than in the *burst* transformation –due to a low *strain–energy*. In the *thermoelastic* case, the transformation takes place as long as there exists a change in the temperature. On the contrary, in the *burst* transformations the driven force $-\Delta G_{Ms}^{A \rightarrow M}$, in the forward– is enough to fulfill the transformation and does not need any thermal supply. Nevertheless, hereafter, the present thesis has been focused on *thermoelastic* transformations for its suitability for magnetic cooling devices.

In summary, due to the FOST nature of the martensitic transformations, which is in between two different magnetic states –e.g., the Curie point undergoes a ferro–para transition–, there emerges two important related features. Firstly, the latent heat⁴⁹ –intrinsic to the FOST– enhances the MCE to be *giant*. But, at the same time, appears the hysteresis, which is also inherent to the FOST, limiting the efficiency for magnetic cooling applications and introducing irreversible entropy contributions –i.e.,

⁴⁹The latent heat (enthalpy) takes place all along a temperature span –instead of a fixed temperature– due to the lack of homogeneity.



(a) Conventional (left) and Inverse (right) CE. In black the entropy in absence of an external field, while in red on applying an external field. Dotted lines for cooling, straight lines for heating. (b) Response in the generalized displacement depending on CE's type.

Figure 1.14: Schematic representation of the entropy change in the vicinity of a first-order magnetic transition. If the field shifts the transition towards a higher temperature, then the response change $\langle\langle \left(\frac{\Delta\Omega}{\Delta T}\right)_\omega \rangle\rangle$ is positive and results a *Direct* or *Conventional* CE. On the other hand, if the field shifts the transition to a lower temperature, then $\langle\langle \left(\frac{\Delta\Omega}{\Delta T}\right)_\omega \rangle\rangle < 0$ for an *Inverse* CE (in the Inverse case (a-right), for clarity, the forward martensitic transition is colored in blue, but the reverse remains in red. Furthermore, in the Conventional case (a-left), the yellow zone remarks the hysteresis in the case of non-external applied field.)

hysteresis losses [yellow zone in fig. 1.14a (left)]. Secondly, $\langle\langle A_f(A_s) \rangle\rangle > M_s(M_f)$ will always be true in consequence of thermal hysteresis [see fig. 1.14a (right) and 1.13]. In fact, the width of the thermal hysteresis is defined by the difference between $\langle\langle A_f(A_s) \rangle\rangle$ and $\langle\langle M_s(M_f) \rangle\rangle$ [see figs. 1.14a (right) and 1.13]. Actually, those heat losses are reduced by both annealing the sample and tuning the composition –consequently, varying the lattice parameters. The samples does suffer the latter treatment in order to attain the Curie temperature close to the martensitic transformation, which results in low-hysteresis materials [99, 100].

To sum up, I would like to remark the *magneto–structural* coupling in the materials studied in the present work. The new martensite phase in the forward transformation emerges from slight coordinated displacements of the atoms in the parent–phase, which are smaller than the interatomic distances. So that, the neighbors in the parent–phase are still neighbors in the new phase as a result of the *displacive* nature during the transformation. Furthermore, the lack of diffusion enables low temperature transitions [101]. Accordingly, the onset of the new crystalline structure does not change the atomic–order of the parent phase neither the original composition. But, indeed, these materials also exhibit magnetic shape–memory effects (see figs. 1.11a, 1.12a and 1.12c) as a result of the *magneto–elastic* coupling.

Finally, in Figure 1.15 it is shown in a easy way, how slight coordinated displacements in the martensitic transformation give rise to different magnetic–order due to the *magneto–structure* coupling in the martensite transformation. In the inset in blue, it is displayed a $M(T)$ curve of a NiMnSn alloy with a FOST in the vicinity of a second order magnetic transition, i.e., from the Ferro–austenite (*iii*) state to a Para–austenite (*iv*) state. It is shown, firstly, that –in the ZFC– the distortion of the material –but not the volume⁵⁰ [9, 13]– diminishes from the (*i*) rhombic martensite state (l''), to the (*iii*) cubic austenite state ($l < l''$). Secondly, how the structural transformation change the atomic order resulting in a magnetization jump, from (*i*) \rightarrow (*iii*). Thus, herein, the phenomenological theory introduced by Weiss [see section 1.2] can easily explain the rearranging of the atoms through the ordering effect of the *molecular field*, as a result of the strong coupling of structural and magnetic degrees of freedom in these alloys.

⁵⁰The martensite volume is, indeed, minor than the austenite one. In fact, the change of volume as a result of an external magnetic field is named *magnetostriction*.

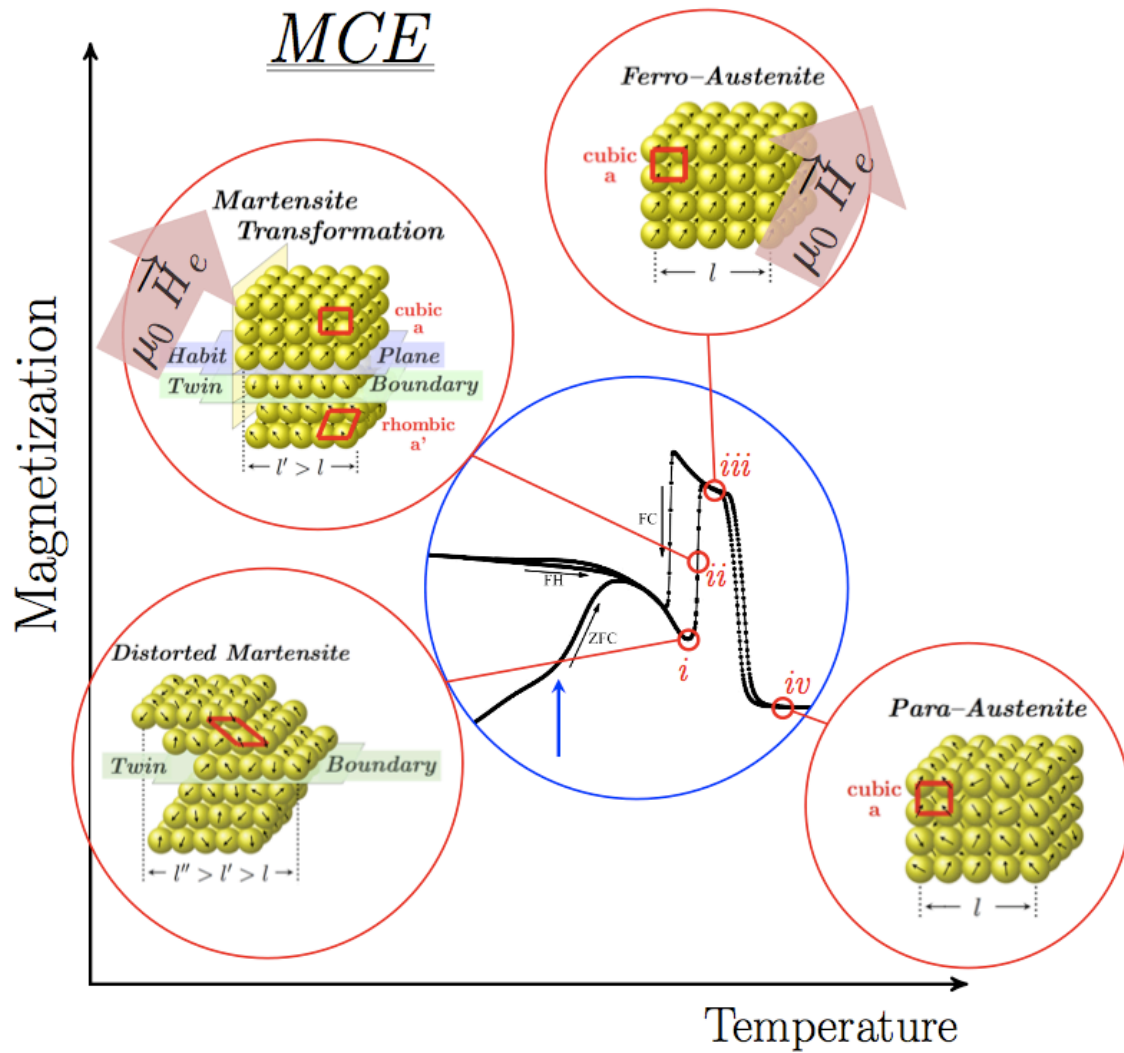


Figure 1.15: Schematic representation of the different phases in the vicinity of a first-order magnetic phase transition.

Therefore, figure 1.15 shows how the structural change –i.e., the atomic order–change the magnetic interaction from a monotonous decrease to the Para-martensite, (*i*), to a magnetization jump in the Ferro-austenite, (*iii*), in the vicinity of the Curie point. In-between the martensite and the austenite, (*ii*), there is a mix-

ing/competition of both states with high related strains, which is consequence of the FOST.

As a matter of fact, a neutron polarization analysis was performed by S.Aksoy et al. [89] in order to understand the magnetization drop nearby the Para-martensite state (*i*). This work revealed an antiferromagnetic behavior –more precisely, antiferromagnetic correlations– at temperatures closely below M_s , whereas they are ferromagnetic above M_s and well beyond the Curie temperature of the austenitic state. Therefore, there exist a short-range ferromagnetic order beyond the Curie point. This explains, for instance, the Exchange-Bias effect of this samples [102] through the ferro-antiferromagnetic competition, which is marked by a blue arrow in the turning point of the fig. 1.15.

1.6 The La[Fe(Si)]₁₃ family of alloys

Today, MCE materials undergoing first-order magnetic transformation (FOMT) are promising materials for magnetic refrigeration at room temperature [see sec. 1.3]. In contrast to second-order magnetic transitions, they can exhibit *giant* MCE, but at the expense of hysteresis losses. In fact, the enhancement of the MCE lies beneath the first-order of the transformation.

Up to now, the *giant* MCE emerges in consequence of the *magneto-structural* coupling in the FOMT, e.g., martensites. On the other hand, the LaFeSi family of alloys undergo a FOMT due to a *magneto-elastic* coupling. In the former case, there exist a structural change in the transition-point [13], while in the latter case, there is a lattice distortion accompanied by a possible volume change [14]. As a common feature, the compounds with a *magneto-structural* coupling often show large thermal and field hysteresis, but the compounds exhibiting a *magneto-elastic* coupling usually

reveal small or tunable hysteresis [9].

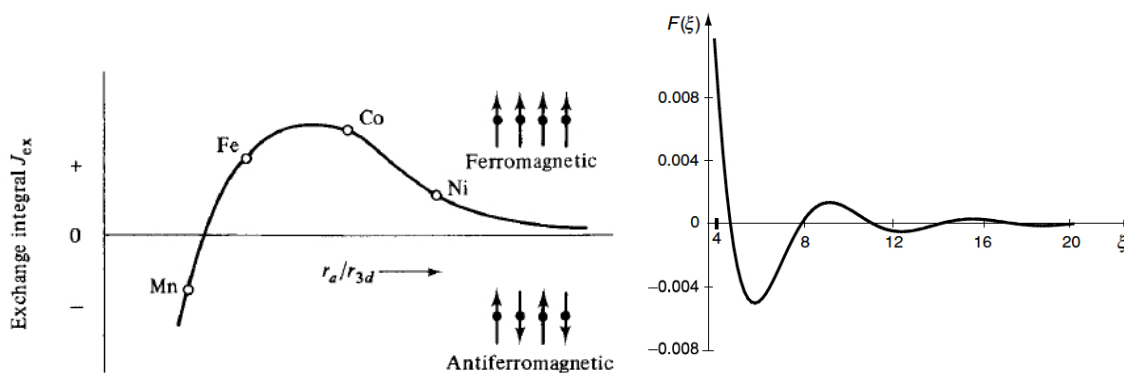
This is an interesting family of compounds constituted by RE and transition elements, with a face-centered-cubic NaZn_{13} -type structure (space group $\text{Fm}\bar{3}\text{c}$). The $\text{La}(\text{Fe}_x\text{Si}_{1-x})_{13}$ alloy emerges among them as the more promising material for magnetic refrigeration. In 2001 *Hu et al.* [103] reported a *giant* MCE for the $\text{LaFe}_{11.4}\text{Si}_{1.6}$, exhibiting a $|\Delta S_{iso}| \simeq 20 \text{ J/kgK}$ at 210 K, and $\text{RC}_{FWHM} = 530 \text{ J/kg}$ for a magnetic change of 5 T, and with a volume reduction of about 1% due to the *magneto-elastic* coupling. But the latter results undergoes the MCE below room temperature. Hydrides [56] appeared as a solution to overcome this problem shifting the transition-point to temperatures close to room temperature, while $|\Delta S_M|$ remains almost the same value, and with an enhancement of ΔT_{ad} as the heat capacity remains almost unchanged [1]. However, hydrides in this alloy are unstable above 423 K. The solution was revealed with the introduction of Co in the LaFeSi alloy [104], which results in the same hydrides' enhancement but without the drawbacks. In addition, as was shown in sec. 1.3, these alloys are postulated as promising MCE materials due to the previously mentioned together with the economic reasons⁵¹.

1.7 Magnetic Interactions: Indirect Exchange

In 1928, Heisenberg showed that such collective behavior, i.e., the ferromagnetism, is the result of a quantum-mechanical exchange interaction between the atomic spins in a crystal lattice: $H_{exch} = -\sum_{i<j} 2 J_{exch} \vec{S}_i \cdot \vec{S}_j$, where the sign of the $\langle J_{exch} \rangle$ determines the spin arrangement of the nearest-neighbor atoms. So, in order to minimize $\langle E_{exch} \rangle$, when $\langle J_{exch} \rangle$ is positive, the spins are aligned parallel ($\cos\phi_{ij} = 1, \rightarrow \phi = 0$). But, if $\langle J_{exch} \rangle$ is negative, the lowest energy states are those

⁵¹The $\langle La \rangle$ appears to be one the cheapest RE [see fig. 1.6a]

spins with antiparallel alignment ($\cos\phi_{ij} = -1, \rightarrow \phi = \pi$) [38,105]. Nevertheless, the interaction becomes complex due to the exchange term, $\langle\langle J_{exch} \rangle\rangle$.



(a) The Bethe–Slater curve for 3d atoms [38].

(b) The RKKY function [24].

Figure 1.16: Indirect Exchange interaction depending on the distance between atomic cores.

Later on, in order to understand the magnetic behavior of the “3d”-transition elements like chromium, manganese, iron, cobalt and nickel, Slater published values of the interatomic distance, $\langle\langle r_{ab} \rangle\rangle$, and the distance of the magnetic cores of the incompletely filled “d” subshell, $\langle\langle r_d \rangle\rangle$, where $\langle\langle r_{ab}/r_d \rangle\rangle$ seems to correlate with the sign of the $\langle\langle J_{exch} \rangle\rangle$ [37]. Soon after, Bethe found the exchange integral for a two-bodies interaction. The results are represented in figure 1.16a. In the 1930s, this Slater-Bethe curve shows a short-range interaction of two “3-d” localized electrons revealing both antiferromagnetism and ferromagnetism behavior.

Due to the localized nature of the electrons the direct exchange becomes difficult. Therefore, the momentum exchange should be produced through an indirect exchange. Ruderman, Kittel, Kasuya and Yosida [eqs. 1.5 and 1.6] showed –in the 1960s– an oscillating behavior of the $\langle\langle J_{exch} \rangle\rangle$ which falls off as $\langle\langle 1/r^3 \rangle\rangle$ [see fig. 1.16b].

The equations of the RKKY-model⁵² are presented below:

$$F(\xi) = \frac{(\sin\xi - \xi\cos\xi)}{\xi^4}, \text{ where } \xi = 2k_F r \quad (1.5)$$

$$\mathcal{J}_{eff} \approx \frac{9 \pi \mathcal{J}_{s-f}^2 n^2 F(\xi)}{64 \mathcal{E}_F} \quad (1.6)$$

where n is the number of conduction electrons per atom, $\mathcal{J}_{s-f} = 0.2eV$ is the exchange constant, of the “ s - d ” electron orbitals of the transition metals, r is the distance of the magnetic cores, and \mathcal{E}_F and \mathcal{K}_F are the Fermi energy and the Fermi wavevector, respectively [24].

This model exhibits a long-range oscillatory coupling between magnetic cores, where the sign of the $\langle J_{exch} \rangle$ fluctuates on a scale of nanometers depending on $\langle r \rangle$ —i.e., the distance between the magnetic cores. Thus, this model can explain the different magnetic orders that exhibit many Heusler alloys undergoing a martensitic transformation through the adaptive atomic-order of martensites [subsect. 1.5].

Nowadays, does not exist an “*a priori*” easy way to design smart materials with the suitable functional properties. So, There is still a long way to go.

⁵²Which can be extender to the 4-f rare-earth metals [24].

CHAPTER 2

EXPERIMENTAL TECHNIQUES

WITHIN the Second Chapter of the present thesis I review at-a-glance the main experimental techniques and the consolidated abilities reached during the thesis period.

2.1 Sample Preparation

The two single-crystal alloys $Ni_{49.3}Mn_{34.2}In_{16.5}$ and $Ni_{48.8}Mn_{34}In_{17.2}$ were synthesized with similar composition at the Materials Preparation Center, Ames Laboratory, U.S. DOE¹ [see section 3.4]. The remaining compositions are polycrystalline ingots. The Heusler alloy $Ni_{49.26}Mn_{36.08}In_{14.66}$ was prepared at the University of Duisburg-Essen² [see section 3.6]; the Fe-doped Heusler alloy $Ni_{52.6}Mn_{21.9}Ga_{24.2}Fe_{1.3}$ [see section 3.5] and the Co-doped $Ni_{50}Mn_{25-x}Ga_{25}Co_x$ MSMA [see section 3.8] were prepared at the

¹Materials Preparation Center, Ames Laboratory, Ames IA 50011, USA. See <http://www.mpc.ameslab.gov>.

²Experimentalphysik, Universität Duisburg-Essen, D-47048 Duisburg, Germany.

Instituto Potosino de Investigación Científica y Tecnológica³ [see sections 3.8]. Finally, the alloy $LaFe_{11.33}Co_{0.47}Si_{1.2}$ at the Indian Association for the Cultivation of Science⁴ [see section 3.7]. All ingots were prepared by arc melting the pure elements under argon atmosphere. The melting process was repeated several times to attain homogeneous compositions⁵. The chemical compositions of the different alloys presented in this thesis were determined by Energy Dispersive X-ray analysis (EDX). For further details check the sample preparation section of the respective paper.

³Instituto Potosino de Investigación Científica y Tecnológica, Camino a la Presa San José 2055. Col. Lomas 4 sección, 78216 San Luis Potosí, S.L.P. México.

⁴Department of Solid State Physics. Jadavpur, Kolkata 700 032 , India.

⁵For further specifications in the sample preparation go to the respective papers.

2.2 Calorimetry

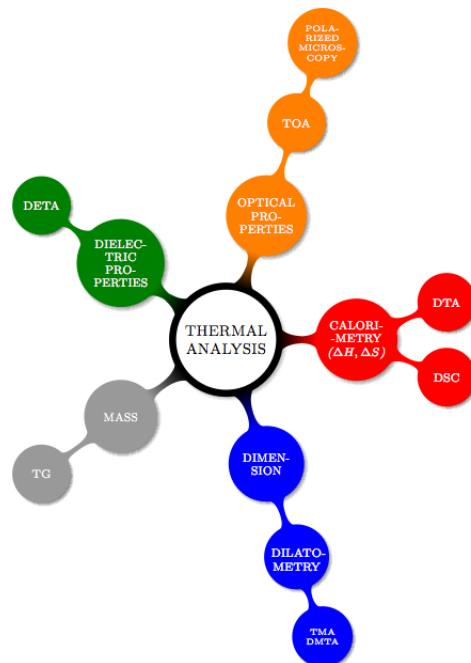


Figure 2.1: Diagram of the different Thermo-Analytical methods. A brief explanation of each technique can be found in table 1.1.

From the suggestion of A.C. Becquerel in 1826 [106] in order to use Seebeck's effect for measuring high temperatures⁶, *calorimetry* has turned to be a fundamental set of techniques in material science to matter characterization. In fact, *thermocouple*⁷ opened up a new kind of devices and thermal techniques. Thus, calorimetry is just one of the different available techniques in Thermal Analysis [see fig. 2.1]. Table 2.1 compiles selected Thermal Analysis techniques.

⁶For a good review in low-temperature calorimetry see the ref. [107].

⁷The thermobattery or the thermopile are just a step forward from the thermocouple which are usually build as a serial-combination of thermocouples.

Table 2.1: A rough description of a selected Thermal Analysis methods.

Thermal Analysis method	Description
Thermogravimetry (TG)	to measure mass changes as a function of the temperature while the sample is subjected to a controlled temperature program.
Thermal Mechanical Analysis (TMA)	to measure volume and linear thermal expansion coefficients but also modulus as a function of temperature.
Dynamical-(D)TMA	to measure stress and strain in a periodically deformed sample at different loading frequencies and temperatures.
Thermal Optical Analysis (TOA)	to measure the transmitted light intensity thanks to a polarized light microscopy (crossed polarized) with a hot-stage by which the temperature of the sample is controlled.
Dielectric Thermal Analysis (DETA)	to provide information about the segmental mobility of a polymer due to the existence of chemical bonds of unlike-atoms.

Within this thesis, the measuring of the magnetocaloric effect –i.e., $\langle\langle\Delta T_{adi}\rangle\rangle$ and $\langle\langle\Delta S_{iso}\rangle\rangle$ – is one of the problems we face. Below are briefly described each one of the different methods that is used for the latter purpose:

- Direct methods: The direct $\langle\langle\Delta T_{adi}\rangle\rangle$ measurements are performed through the

difference between the initial temperature –before applying the magnetic field– and the final temperature –once the field has been applied–, with a confidence ranging from 5% to 10% [53]. On the other hand, the direct $\langle\langle\Delta S_{iso}\rangle\rangle$ measurements are realized by a differential Scanning calorimeter (DSC) device which was design to working with applied magnetic fields [a sketch of the DSC device built by the PhD student is shown in fig. 2.2]. Then, we should integrate the heat-flux rate data obtained from the calorimetric run in order to compute the desired $\langle\langle\Delta S_{iso}\rangle\rangle$, $S(T, H) - S(T_0, H) = \int_{T_0}^T 1/T \dot{Q}(H)/\dot{T} dT$ ⁸.

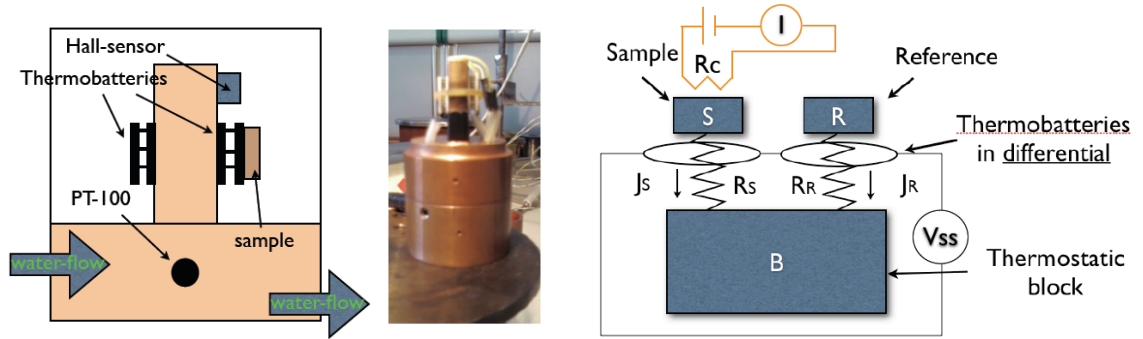
- Indirect methods: On one side, measuring the temperature dependence of the heat capacity, $C_H(T, H)$, when applying a magnetic field on the sample. It is easy to compute both $\langle\langle\Delta T_{adi}\rangle\rangle$ and $\langle\langle\Delta S_{iso}\rangle\rangle$ through the eqs. [1.2] and [1.1], respectively. On the other hand, from the magnetization curves as a function of the temperature when applying a magnetic field, it is also easy to compute the MCE through again the eqs. [1.2] and [1.1].

2.2.1 Direct Methods

In fig. 2.2a it is shown a sketch of a DSC calorimeter, where thermobatteries are the key point of the heat reading. Heating or cooling at moderate rates results in a time evolution of the temperatures in the system, such as the temperature of the block, the temperature of the sample and the temperature of the reference.

If the sample undergoes a first order transition, it results in a variation of the enthalpy at a rate, i.e., in a heat-flux rate dQ/dt . In this case, the energetic equations

⁸where $\dot{Q}(H)$ is the heat flux, \dot{T} is the cooling rate and H is the magnetic field.



(a) Sketch (left) and a photo (right) of a DSC. (b) Schematic representation of a typical DSC.

Figure 2.2: Schematic representation of the DSC used within the present thesis in order to measure all the calorimetric data on applying a magnetic field. In (a) it is represented an sketch of the DSC together with a real photo where are pointed all the different parts. In addition it is shown the water-flow which refrigerates the whole system. A block diagram of the experimental set-up for calibration.

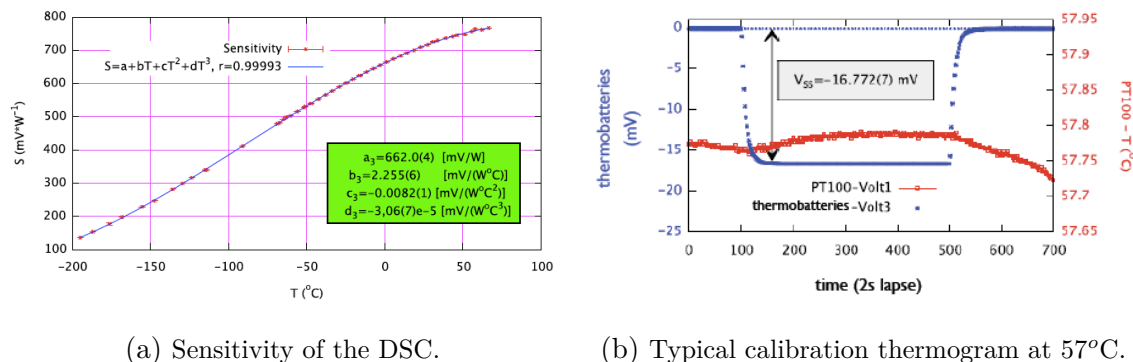
of thermal balance for the sample and the inert reference are:

$$\frac{dQ}{dt} = C_S \frac{dT_S}{dt} + J_S \quad (2.1)$$

$$0 = C_R \frac{dT_R}{dt} + J_R \quad (2.2)$$

where C_S , C_R , T_S , and T_R are the heat capacity (C) and the temperature (T) of the sample (S) and the reference (R), respectively, and J_S and J_R are the heat fluxes of the sample and the reference with regard to the thermostatic bloc (B).

Prior to the calculation of the $\langle \Delta S_{iso} \rangle$ from a calorimetric run using a DSC method, we should calibrate the set-up. For this purpose, it is represented an electric circuit on top of the figure 2.2b. When a current flows through the resistance, it dissipates a known heat that is used in order to calibrate the output of the DSC



(a) Sensitivity of the DSC.

(b) Typical calibration thermogram at 57°C.

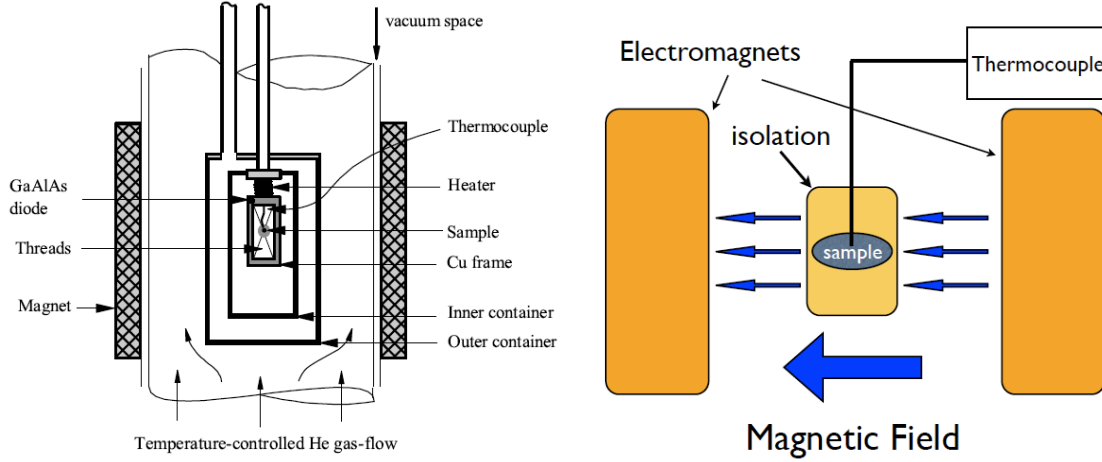
Figure 2.3: In (a) the Sensitivity is represented as a function of time. The solid line is a parabolic fit to the data that is also shown in the inset together with the error bars of the calibration. In (b) a typical calibration thermogram is represented showing the calorimetric output V_{SS} as a function of time.

–i.e., the V_{SS} – from the system of eqs. 2.1 and 2.2⁹.

In figure 2.3 are shown the thermobatteries differential-signal (V_{SS}) at a fixed temperature when it is dissipated a known heat [fig. 2.3b], and the sensitivity (S) of the DSC [fig. 2.3a]. In fig. 2.3b we show the high sensitivity of this kind of calorimeter, which is highly sensitive in comparison to the commercial ones.

Furthermore, we also performed direct ΔT_{ad} measurements. In figure 2.4 there appears a sketch of the the set-ups from both the University of Duisburg-Essen [fig. 2.4a] and the University of Barcelona [fig. 2.4b]. In Duisburg, the whole apparatus was placed into a helium cryostat which incorporates a superconducting magnet delivering fields up to 5 T. It was used Helium as exchange gas, and a calibrated and nearly field-insensitive GaAlAs diode thermometer (LakeShore TG-120-P) and the heater were used to measure and control the temperature of the copper frame.

⁹For more details about the DSC please check [108], but for more details about the thermal analysis of the calorimetric run check [109].



(a) Sketch of the set-up from Duisburg [110].

(b) Sketch of the set-up from Barcelona.

Figure 2.4: (a) Sketch of the low temperature part of the experimental setup for the direct adiabatic temperature-change measurements using a differential thermocouple from Duisburg [110]. (b) Schematic representation of the direct adiabatic temperature-change of the set-up from the Barcelona.

The space between the inner and outer containers is evacuated to obtain adiabatic conditions during a measurement on applying a magnetic field [110].

On the other hand, in Barcelona was performed a cheaper and easy set-up to obtain direct ΔT_{ad} measurements [see fig. 2.4b]. The whole set-up consists in an electromagnet, a calibrated PT100-sensor, a polystyrene insulator and the sample, which as schematized in figure 2.5. In fig. 2.5a it can be seen the good result in such a easy set-up¹⁰. This result can be explained in terms of adiabaticity. It is well-known the exponential Newton-law for thermal equilibrium: $T^{Sample} = T_{room-temp} + (T_0^{sample} - T_{room-temp})e^{-t/\tau}$, where $\langle\tau\rangle$ is the characteristic time of relaxation for the

¹⁰It should be noticed that similar experiments were carried out previously by PhD X. Moya, but on different materials [111].

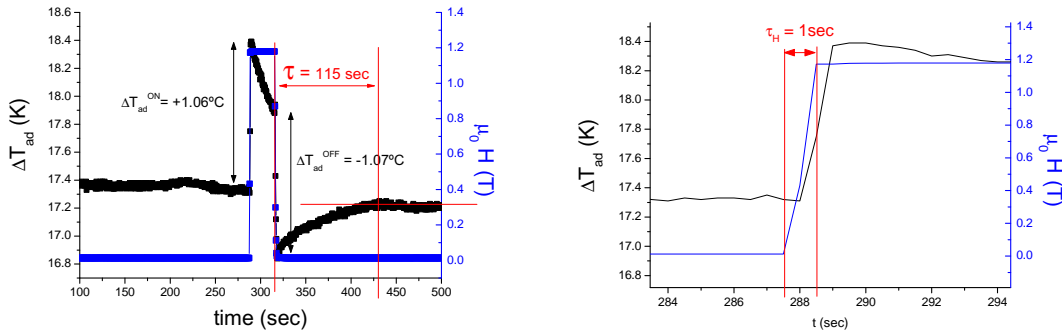
(a) Direct ΔT_{ad} measurement.(b) Timing of the direct ΔT_{ad} measurement.

Figure 2.5: Direct ΔT_{ad} measurements from the University of Barcelona in a $\text{Ni}_{49.26}\text{Mn}_{36.08}\text{In}_{14.66}$ alloy ($\text{mass}_{\text{NiMnIn}} \simeq 2.2$ g).

calorimeter, and $\ll t \gg$ -i.e., $t = \tau_H$ in fig. 2.5b- corresponds to the reaction time on applying the magnetic field. From fig. 2.5 we obtain the next relation $\ll t/\tau = 0.01 \gg$, so the exponential tends to one, and, therefore, it can be inferred that the environment does not affect the direct ΔT_{ad} measurement when applying the magnetic field. The key point in an adiabatic measurement is indeed the rate between the reaction time of the sample $\ll t \gg$ and the characteristic relaxation time of the ΔT_{ad} set-up.

2.2.2 Indirect Methods

Magnetometers

The magnetization measurements as a function of temperature $M(T)$ in external magnetic fields of 5mT and 5 T, and the magnetization as a function of magnetic field $M(H)$ up to 5 T were carried out in a SQUID (Superconducting Quantum Interference Device) MPMS XL magnetometer (Quantum Design) during a stay abroad in the University of Duisburg-Essen in order to characterize different samples [see



Figure 2.6: Picture of an Magnetic Property Measurement System (MPMS) system.

fig. 2.6]. Below are summarized the main characteristics of a representative set of magnetometers.

2.3 Ultrasonic Experiments

At the very beginning of my PhD, a set of ultrasonic experiments were carried out at the university of Barcelona for studying the wave propagation through the sample in order to obtain its elastic constants.

Herein are performed ultrasonic experiments through pulses propagation methods in order to use both transversal and longitudinal polarization for the characterization of the sample [see table 2.3]. In addition, this ultrasonic method enables the use of relatively small sample ($\sim \text{cm}^3$). The experimental technique that has been used for measuring the elastic constants is the so-called *pulse-echo* technique.

Table 2.2: A brief description of the different magnetometers.

Magnetometer	Temperature Range	Magnetic Field	Sensitivity (emu)	Frequency	Mechanism
VSM-PPMS	DC: 50K – 400K	± 3 T	10^{-6}	—	Faraday- induction law
PPMS	DC: 1.9K – 375K AC: 1.9K – 350K	± 9 T	DC: $2.5 \cdot 10^{-5}$ AC: $2 \cdot 10^{-8}$	DC: – AC: 10 Hz –10 kHz	Faraday- induction law
MPMS-SQUID	DC: 1.9K – 350K	± 5 T	10^{-8}	—	Josephon Effect

Table 2.3: Propagation modes used in ultrasonic measurements.

Propagation	Polarization	Elastic constants	Mode
[001]	[001]	C_{11}	Long.
	\perp [001]	C_{44}	Trans.
[110]	[110]	$C_L \equiv \frac{C_{11}+c_{12}+2C_{44}}{2}$	Long.
	[001]	C_{44}	Trans.
	[1 $\bar{1}$ 0]	$C' \equiv \frac{C_{11}-C_{12}}{2}$	Trans.
[111]	[111]	$(C_{11}+2C_{12}+4C_{44})/3$	Long.
	\perp [1 1 1]	$(C_{11}-C_{12}+C_{44})/3$	Trans.

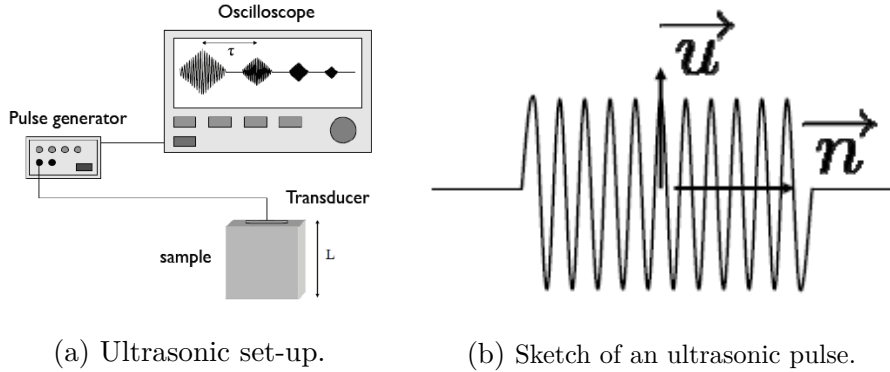


Figure 2.7: (a) Sketch of the ultrasonic set-up for measuring the elastic constants. (b) Schematic representation of an ultrasonic pulse, where \vec{u} is the polarization of the pulse, and \vec{n} is the pulse propagation direction [111].

We transmit an ultrasonic pulse ($1 - 2\mu s$ lapse time) through the stimulation of a piezoelectric transducer adhered to one side of the sample. Then, the wave propagates along the sample just before being reflected on the opposite side of the transducer in order to be detected. The pulse is partially reflected on the transducer, returning back to the opposite side and so on until the pulse vanishes.

Finally, we obtain a wavefront –i.e., echos– that present an exponential decay. The delay between two successive echos is the route-time along the sample, going and back, i.e., the round trip. If we know the time τ and the dimensions of the sample L , then we can compute the velocity of the wavefront ($v = 2L/\tau$). From the table 2.3 we can obtain the three elastic constants of the single-crystal (C_{11} , C_{12} and C_{44}), and combinations.

3.1 List of Contributions

TAL i com estipula la normativa reguladora dels procediments relatius a l'elaboració, defensa i avaluació de les tesis doctorals a la UB, d'acord amb la disposició addicional segona “Tesis doctorals presentades com a compendi de publicacions”, a continuació es presenten dos escrits on el director i tutor de la Tesi, el Dr. Lluís Mañosa i Carrera, fa constar: (1) El factor d'impacte de les publicacions que es recullen en la tesi [secció 3.2]; i en segon lloc, (2) al ser un treball en coautoria, redactat exhaustiu on s'especifica la participació del doctorand en la participació de cada article, tot manifestant la utilització d'algun d'aquests treballs en la realització d'alguna altra tesi [secció 3.3].

Un cop feta aquesta aclaració en les dues primeres seccions [seccions 3.2 i 3.3] del capítol 3 de la present tesi, s'introdueixen cadascuna de les publicacions amb el seu resum corresponent als resultats obtinguts a cada publicació.

3.2 Factor d'Impacte

Els resultats del treball de la tesi doctoral de David González Alonso s'han publicat en les revistes de més prestigi i impacte en les àrees de Física de la Matèria Condensada, Física Aplicada i Ciència de Materials, totes elles en el primer quartil de les esmentades àrees.

Dos dels treballs han estat publicats a la revista *Physical Review B*. Es pot considerar aquesta revista com la de més prestigi en l'especialització de Matèria Condensada on publicar treballs complets. El seu factor d'impacte és de 3.475 (any 2009) i 3.690 (any 2011).

La rellevància i urgència dels resultats corresponents a l'efecte elastocalòric d'aliatges amb memòria de forma va fer que aquest treball fos publicat en una revista d'alt impacte i de difusió molt ràpida com és *Applied Physics Letters*. Aquesta revista té un impacte de 3.820 (any 2010) i està a la zona alta del primer quartil de Física Aplicada (posició 14 sobre un total de 116 publicacions).

L'estudi de materials sota pressió hidrostàtica va donar lloc a uns resultats de gran rellevància. La primera evidència de materials amb efecte barocalòrics gegants va ser considerada d'interès prou important per a una audiència àmplia i va ser mereixedora de ser publicada en la revista líder en Ciència de Materials i Física de la Matèria Condensada, *Nature Materials*. Aquesta revista té un impacte de 29.897.

D'altra banda, l'efecte barocalòric invers també va representar un treball molt significatiu i va ser publicat en una de les revistes més prestigioses en Ciències Multidisciplinàries com és *Nature Communications*. Aquesta revista, amb un impacte de 7.4 està entre les més ben posicionades en aquesta àrea.

Finalment voldria esmentar que l'impacte dels resultats continguts a la tesi de David González es veu reflectit pel gran nombre de citacions que han rebut. Malgrat

tractar-se de resultats molt recents, en poc més de tres anys (2010-2013), aquests cinc articles han rebut ja més d'un centenar de cites (Web of Science).

3.3 Participació de David González Alonso en els articles de la seva tesi

3.3.1 Article 1: "Lattice dynamics in magnetic superelastic Ni-Mn-In alloys: Neutron scattering and ultrasonic experiments"

L'article presenta mesures de constants elàstiques i de corbes de dispersió de fonons en una mostra monocristal·lina de Ni-Mn-In.

El doctorand va participar en la caracterització de la mostra mitjançant tècniques calorimètriques. Va ser qui va realitzar tot el conjunt de mesures de les constants elàstiques utilitzant tècniques ultrasonores. Aquestes mesures es van realitzar en funció de la temperatura i del camp magnètic.

Les determinació de les corbes de dispersió de fonons es va realitzar a partir de mesures de dispersió de neutrons al reactor de Oak Ridge (Tennessee, US).

El doctorand va participar activament en l'anàlisi i la discussió de totes les dades experimentals.

3.3.2 Article 2: "Stress-and magnetic field-induced entropy changes in Fe-doped Ni-Mn-Ga shape-memory alloys"

L'article presenta mesures de deformació en funció de la temperatura per a diferents esforços aplicats i de calorimetria sota camp magnètic. Aquestes mesures permeten

determinar els canvis d'entropia associats als efectes elastocalòric i magnetocalòric d'un aliatge magnètic amb memòria de forma.

En David és responsable de la part referida a l'efecte magnetocalòric. Les mesures calorimètriques van requerir posar a punt i calibrar un calorímetre de flux diferencial que fos capaç de treballar sota camps magnètics. Amb aquest dispositiu el doctorand va realitzar el conjunt de mesures calorimètriques en funció de la temperatura per a una sèrie de valors del camp magnètic. També es va encarregar del corresponent tractament i anàlisi de les dades experimentals que va conduir a la determinació de l'efecte magnetocalòric d'aquest material.

Les mesures de deformació es van realitzar a l'IFIMAT de Mèxic on també es va fabricar la mostra utilitzada.

El doctorand va participar activament en l'anàlisi i la discussió de totes les dades experimentals.

3.3.3 Article 3: "Giant solid-state barocaloric effect in the Ni-Mn-In magnetic shape memory alloy"

L'article presenta mesures calorimètriques sota camp magnètic i sota pressió hidrostàtica per a un aliatge de Ni-Mn-In.

L'aliatge va ser fabricat a la Universitat de Duisburg-Essen (Alemanya). La preparació de les mostres per a les diferents tècniques calorimètriques, a partir del material rebut va ser responsabilitat del doctorand. Utilitzant el calorímetre sota camp magnètic que havia posat a punt, en David va realitzar el conjunt de mesures en funció de la temperatura i el camp magnètic que van permetre determinar l'efecte magnetocalòric del compost.

Les mesures calorimètriques sota pressió hidrostàtica es van realitzar al Departament

ment de Física de la UPC.

El doctorand va participar activament en l'anàlisi i la discussió de totes les dades experimentals.

3.3.4 Article 4: "Inverse barocaloric effect in the giant magnetocaloric La-Fe-Si-Co compound"

L'article presenta mesures de calorimetria sota pressió i de canvis de temperatura en un compost amb efecte magnetocalòric gegant de la família La-Fe-Si.

La mostra va ser preparada a IACS (Kolkata, India). La preparació de les mostres per a les tècniques calorimètriques, i per a les mesures directes del canvi de temperatura, a partir del material rebut va ser responsabilitat del doctorand. La part corresponent al creixement de mostres pot formar part de la tesi doctoral de Amitava Bhattacharyya.

Les mesures de calorimetria sota pressió es van realitzar al Departament de Física de la UPC.

Una part important del treball consisteix en fer mesures directes dels efectes calòrics a partir de la mesura del canvi de temperatura associat a aquests efectes. Per a tal fi, el doctorand va dissenyar, posar a punt i cal·librar un sistema experimental que permetés mesurar els canvis adiabàtics de temperatura en aplicar camps magnètics. Amb aquest sistema va mesurar els canvis de temperatura que es donen en el compost quan s'aplica un camp de 1T. Les mesures es van fer en un ampli rang de temperatures.

A més, la relació entre els canvis d'entropia determinats calorimètricament i els canvis de temperatura requereix conèixer la capacitat calorífica del material. En David va mesurar aquesta magnitud utilitzant un calorímetre modulad que va haver

de calibrar previament a les mesures.

El doctorand va participar activament en l'anàlisi i la discussió de totes les dades experimentals.

3.3.5 Article 5: "Caloric effects induced by magnetic and mechanical fields in a $\text{Ni}_{50}\text{Mn}_{25-x}\text{Ga}_{25}\text{Co}_x$ magnetic shape memory alloy"

L'article presenta mesures de deformació a través de la transformació magnetoestructural d'un aliatge magnètic amb memòria de forma subjecte a l'acció simultània de camps magnètics i esforços mecànics.

El gruix de les mesures experimentals es van realitzar al CIMAV (Mèxic), i una part del treball forma part de la tesi de P.O. Castillo-Villa. Al nostre laboratori de la UB es van realitzar les mesures de calorimetria sota camp magnètic.

En David va assistir al Dr. Daniel Soto-Parra en les mesures de calorimetria sota camp magnètic durant l'estada que aquest va realitzar al nostre departament. A més, l'experiència adquirida pel doctorand en els treballs anteriors, el va portar a una participació activa en l'anàlisi de les dades experimentals i en la posterior discussió que es va realitzar durant l'estada del Dr. Daniel Soto-Parra al nostre Laboratori.

3.4 Paper 1: Lattice dynamics in magnetic superelastic Ni–Mn–In alloys: Neutron scattering and ultrasonic experiments

Resum

La dispersió de neutrons y els ultrasons són dos mètodes que s'han emprat per a l'estudi de la dinàmica de xarxa de dos monocristalls tipus Heusler amb una composició propera a $\text{Ni}_{50}\text{Mn}_{34}\text{In}_{16}$, que presenta un comportament magnèticament superelàstic. El paper informa sobre la determinació experimental de l'afebliment de les corbes de dispersió de fonons y de les constants elàstiques per aquest sistema d'aliatges. Es va trobar que les freqüències de la branca TA_2 són relativament febles i que exhibeixen una petita deformació anòmala per al nombre d'ona $\xi_0 \approx 1/3$, la qual s'estova amb la disminució de temperatura. Associat amb l'estovament d'aquest fonó, també es va observar el reblaniment de la constant elàstica de cisalla $C' = (C_{11} - C_{12})/2$. Totes dues atenuacions son habituals dels sòlids amb una estructura bcc que experimenten una transformació martensítica, cosa que reflecteix la inestabilitat dinàmica de la xarxa cúbica sota deformacions de cisalla dels plans $\{110\}$ al llarg de les direccions $\langle 1\bar{1}0 \rangle$. A més, es mesura l'afebliment de la branca de dispersió de fonons i de les constants elàstiques sota l'aplicació d'un camp magnètic per a la caracterització de l'acoblament magnetoelàstic.

Lattice dynamics in magnetic superelastic Ni-Mn-In alloys: Neutron scattering and ultrasonic experiments

Xavier Moya,^{*} David González-Alonso, Lluís Mañosa,[†] and Antoni Planes
*Departament d'Estructura i Constituents de la Matèria, Facultat de Física, Universitat de Barcelona,
 Diagonal 647, E-08028 Barcelona, Catalonia, Spain*

V. O. Garlea, T. A. Lograsso, D. L. Schlagel, and J. L. Zarestky
Ames Laboratory, Iowa State University, Ames, Iowa 50011, USA

Seda Aksoy and Mehmet Acet
Fachbereich Physik, Experimentalphysik, Universität Duisburg-Essen, D-47048 Duisburg, Germany
 (Received 4 March 2009; revised manuscript received 2 June 2009; published 30 June 2009)

Neutron scattering and ultrasonic methods have been used to study the lattice dynamics of two single crystals of Ni-Mn-In Heusler alloys close to Ni₅₀Mn₃₄In₁₆ magnetic superelastic composition. The paper reports on the experimental determination of the low-lying phonon-dispersion curves and the elastic constants for this alloy system. We found that the frequencies of the TA₂ branch are relatively low and it exhibits a small dip anomaly at a wave number $\xi_0 \approx 1/3$, which softens with decreasing temperature. Associated with the softening of this phonon, we also observed the softening of the shear elastic constant $C' = (C_{11} - C_{12})/2$. Both temperature softenings are typical for bcc-based solids which undergo martensitic transformations and reflect the dynamical instability of the cubic lattice against shearing of {110} planes along $\langle 1\bar{1}0 \rangle$ directions. Additionally, we measured low-lying phonon-dispersion branches and elastic constants in applied magnetic fields aimed to characterize the magnetoelastic coupling.

DOI: [10.1103/PhysRevB.79.214118](https://doi.org/10.1103/PhysRevB.79.214118)

PACS number(s): 81.30.Kf, 63.20.-e, 64.70.K-, 62.20.de

I. INTRODUCTION

The search of magnetic shape memory alloys with more favorable mechanical properties than Ni₂MnGa has prompted in recent years the study of new Ni-Mn-based Heusler alloys, extending this alloy family to other elements of groups IIIA-VA.¹⁻⁴ Among them, Ni-Mn-In system has drawn much attention due to the large shift of the martensitic transition temperatures by an applied magnetic field observed in Ni₅₀Mn₃₄In₁₆ (~ 10 K/T), as a consequence of a strong spin-lattice coupling at a microscopic level.⁵ These large shifts allow for the application of moderate magnetic fields to induce the structural transition and lead to many functional properties such as the magnetic superelasticity,⁵ the large inverse magnetocaloric effects,⁶⁻⁸ and the magnetoresistance.⁹

From a fundamental point of view, many of the Ni-Mn based alloys exhibit singular lattice-dynamical behavior associated with the martensitic transition from a high-temperature cubic phase to a lower-symmetry martensitic phase. Specifically, in the case of Ni-Mn-Ga and Ni-Mn-Al alloys, it has been experimentally shown that the transverse TA₂ branch shows a dip at a particular wave number (anomalous phonon). The energy of such anomalous phonon softens with decreasing the temperature.¹⁰⁻¹⁵ The temperature dependence of the energy of the anomalous phonon parallels that of the elastic constant $C' = (C_{11} - C_{12})/2$, which also softens with decreasing temperature.¹⁶⁻¹⁹ The softening observed both with neutron scattering and ultrasonic methods is typical for bcc-based solids which undergo martensitic transformations and reflects the dynamical instability of the cubic lattice against shearing of {110} planes along the $\langle 1\bar{1}0 \rangle$

directions.²⁰ In addition, significant magnetoelastic coupling exists in these systems as evidenced by the enhancement of the anomalous phonon softening when the sample orders ferromagnetically^{12,13} and by the change in the elastic constants when a magnetic field is applied.^{19,21}

The study of the lattice dynamics of a broader class of Ni-Mn-based compounds is important for a deeper understanding of the physical mechanisms behind the multifunctional properties of martensitic Heusler alloys. Therefore, much effort has been devoted in recent years to extend the study of the lattice dynamics to alloys other than Ni-Mn-Ga and Ni-Mn-Al by means of first-principles calculations.^{22,23} In particular, Entel *et al.* showed that the application of a magnetic field leads to the gradual vanishing of the phonon instability in the low-lying TA₂ branch for stoichiometric Ni₂MnIn, thus stabilizing the high-temperature cubic phase.²³ The aim of the present work is to extend the experimental study of the lattice dynamics of this alloy family to the Ni-Mn-In system, both in the short-wavelength and the long-wavelength limits by measuring the phonon-dispersion branches and the elastic constants. Due to the strong interplay between magnetic and structural degrees of freedom typically exhibited by these compounds, we carried out both kinds of experiments in applied magnetic field.

The paper is organized as follows. In Sec. II we describe the details of single-crystal preparation and experimental techniques. Section III is devoted to the experimental results and is split into three sections, which describe the calorimetric (Sec. III A), the phonon dispersion (Sec. III B), and the elastic constants (Sec. III C) results. Finally, in Sec. IV we summarize and conclude.

II. EXPERIMENTAL DETAILS

A. Sample preparation

The single crystals were synthesized at the Materials Preparation Center, Ames Laboratory, U.S. DOE.²⁴ Two single crystals with similar compositions were prepared: one for neutron scattering experiments and another one for ultrasonic experiments. Appropriate quantities of high-purity nickel, manganese, and indium were used to make these alloys. The electrolytic manganese was prearc melted to outgas it before alloying it with the other metals. The metals were arc melted several times under an argon atmosphere, flipping the buttons each time. The buttons were then remelted and the alloy drop cast into a copper chill cast mold to ensure compositional homogeneity throughout the ingots. The crystals were grown in a resistance furnace from the as-cast ingots in an alumina Bridgman style crucible. The ingots were heated under a pressure of 5.0×10^{-6} torr up to 1000 and 900 °C, for the neutron scattering and the ultrasonic method samples, respectively, to degas the crucible and charge. The chamber was then backfilled to a pressure of 2.8×10^3 kPa with high-purity argon. This overpressurization was done near melting to diminish gas pockets from being trapped in the cone region of the crystal and also to minimize the amount of manganese evaporation from the melt during crystal growth. The ingots were further heated to 1250 and 1200 °C, for the neutron scattering and the ultrasonic measurements samples, respectively, and held at this temperature for 1 h to allow thorough mixing before withdrawing the samples from the heat zone at a rate of 5 mm/hr. The as-grown ingots were heat treated at 900 °C for 1 week and cooled at a rate of 10 °C/min. The average composition of the alloys were determined by energy dispersive x-ray analysis to be $\text{Ni}_{49.3}\text{Mn}_{34.2}\text{In}_{16.5}$ and $\text{Ni}_{48.8}\text{Mn}_{34}\text{In}_{17.2}$ (within ± 0.5 at. %) for the samples used in neutron scattering and ultrasonic experiments, respectively.

B. Calorimetric measurements

Structural and magnetic transitions of the samples were characterized by means of differential scanning calorimetry (DSC) measurements. Calorimetric measurements were carried out in the temperature range $150 \leq T \leq 375$ K in a DSC (TA Instruments MDSC 2920) at cooling and heating rates of 5 K/min. We have also used a second high-sensitivity calorimeter for measurements in the temperature range $100 \leq T \leq 350$ K. In this case, typical cooling and heating rates were 0.5 K/min.

C. Neutron scattering

The crystals used in the experiments were cut from a large boule to a size allowing mounting in the various sample environment systems. A side benefit of this was a larger surface-to-volume ratio, which is important because of the large absorption cross section of In for thermal neutrons (194 bn). The samples were still sizable (~ 4 and ~ 6 cm³) although not perfect single crystals. Rocking curves of the (220) Bragg reflections used for sample orientation showed, in one case, a secondary peak, which was very close to the

primary peak ($< 1^\circ$ away) and, in the other case, a secondary peak with much lower intensity than the primary peak ($\sim 20\%$). Peak widths of the (220) rocking curves were from 0.5° to 1° . The secondary peaks warranted caution in interpretation of the data but were not prohibitive in performing the experiments.

The inelastic neutron scattering experiments were performed using the HB1A triple-axis spectrometer at the High Flux Isotope Reactor of the Oak Ridge National Laboratory. The monochromator and analyzer used the (002) reflection of pyrolytic graphite (PG). Highly oriented PG filters were used to minimize higher-order contaminations of the beam. The HB1A spectrometer operates at a fixed incident energy of 14.6 meV requiring most scans to be performed with neutron-energy gain. Nominal collimations of $48' - 48' - 40' - 68'$ (or $136'$) were used and all scans were performed in the constant- Q mode while counting against neutron monitor counts.

The temperature-dependent dispersion-curve measurements were made in a closed-cycle helium refrigerator with a high-temperature interface unit enabling the sample to be warmed to temperatures above room temperature. The temperature control was better than ± 1 K and the accuracy, due to temperature sensor location, was $\sim \pm 5$ K. The magnetic-field measurements were made in a conventional superconducting cryomagnet with temperature control again to within ± 1 K. The sample location on the HB1A triple-axis spectrometer, which is near the massive and magnetic monochromator drum of the HB1 triple-axis spectrometer, requires limiting applied magnetic fields to ~ 4 T.

D. Ultrasonic methods

The single crystal was oriented in the austenite phase by Laue back reflection, and a parallelepiped specimen with dimensions of $5.0 \times 5.0 \times 3.7$ mm³ with faces parallel to the $(1\bar{1}0)$, (110) , and (001) planes, respectively, was spark cut from the oriented boule. The faces were ground parallel and flat using standard metallographic techniques.

The velocity of ultrasonic waves was determined by the pulse-echo technique. X- and Y-cut transducers with resonant frequencies of 10 MHz were used to generate and detect the ultrasonic waves. The transducers were acoustically coupled to the surface of the sample by means of Dow Corning Resin 276-V9 in the temperature range of 200–320 K and by Crystalbond509 (Aremco Products, Inc.) in the temperature range of 310–360 K. For high-temperature measurements (up to 360 K), the sample was placed into a copper sample holder, which was heated by means of a heating plate. For low-temperature measurements (down to 200 K), the sample and the sample holder were introduced into a Dewar glass containing liquid nitrogen. In both cases, the temperature was measured by a Ni-Cr/Ni-Al thermocouple attached to the sample.

The measurements of the magnetic-field dependence of the elastic constants were carried out in a purpose-built device that allows both isofield and isothermal measurements of the ultrasonic velocities in applied fields up to 1.3 T (details are given in Ref. 19). The measurements were carried

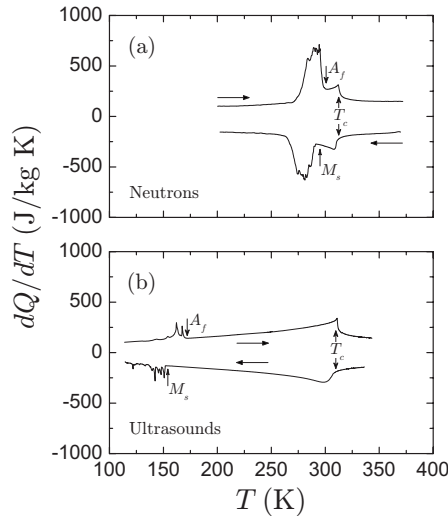


FIG. 1. Calorimetric curves for the samples used in (a) neutron scattering ($\text{Ni}_{49.3}\text{Mn}_{34.2}\text{In}_{16.5}$) and (b) ultrasonic measurements ($\text{Ni}_{48.8}\text{Mn}_{34}\text{In}_{17.2}$). Vertical arrows show the position of martensitic and Curie transition temperatures. Heating and cooling runs are shown with horizontal arrows.

out at constant temperature and the magnetic field was applied perpendicular to the propagation direction of the ultrasonic waves.

III. EXPERIMENTAL RESULTS AND DISCUSSION

A. Calorimetry

We carried out calorimetric measurements in order to characterize the samples to be studied in the neutron scattering and the ultrasonic experiments. Calorimetric studies were carried out on small pieces of samples cut using a low-speed diamond saw from the top and bottom of the large ingot (~ 7 cm long), which was used in the neutron scattering experiments. For the sample cut from the top of the ingot [Fig. 1(a)], calorimetric studies revealed both a ferromagnetic transition at the Curie temperature $T_C=312$ K and a martensitic transformation at a lower temperature with characteristic temperature $(M_s+A_f)/2 \approx 297$ K (M_s : martensite start; A_f : austenite finish). Measurements for the sample cut from the bottom yielded similar results with a shift of the transition temperatures of approximately 10 K to higher values—with the shift of the structural transitions being slightly larger than the shift of the Curie point. These discrepancies are ascribed to small changes on composition through the length of the ingot. Similar measurements carried out in the parallelepiped specimen used in the ultrasonic experiments revealed a ferromagnetic transition at $T_C=310$ K and a martensitic transformation at lower temperatures with characteristic temperature $(M_s+A_f)/2 \approx 161$ K [Fig. 1(b)].

B. Phonon dispersion

Figure 2 shows the phonon-dispersion curves determined from inelastic neutron scattering at 520 K along the high-symmetry directions $[\xi 0 0]$ and $[\xi \xi 0]$. Note that the plot of

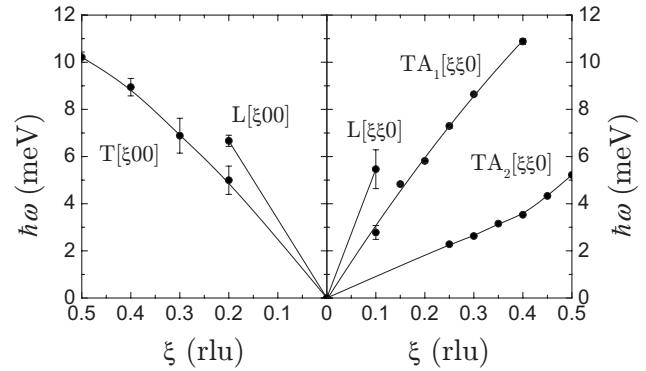


FIG. 2. Acoustic phonon-dispersion curves along the high-symmetry directions $[\xi 0 0]$ and $[\xi \xi 0]$ measured at 520 K. Solid lines are guides to the eye.

dispersion curves is restricted to half of the Brillouin-zone scheme. The measured phonon spectrum shows the features typical of bcc materials that undergo martensitic transformations, i.e., low energies of the phonons of the transverse $\text{TA}_2[\xi \xi 0]$ branch and a wiggle at $\xi_0 \approx 0.33$. A similar behavior has also been reported for the related systems Ni-Mn-Ga and Ni-Mn-Al with compositions close to stoichiometry.^{10–14} The existence of such an anomaly in the transverse TA_2 branch is ascribed to a strong electron-phonon coupling and the Kohn anomaly.²⁵

In order to study the temperature dependence of the anomaly observed in the transverse TA_2 branch, we measured this dispersion curve at several temperatures down to room temperature, i.e., just above the structural transition. The results are shown in Fig. 3. For the sake of clarity, measurements only at three temperatures are presented. As can be seen from the figure, as the temperature is reduced, the energy of the branch close to the anomalous phonon decreases, thus reflecting the dynamical instability of the cubic lattice against distortions of $\{110\}$ planes along $\langle 1\bar{1}0 \rangle$ direc-

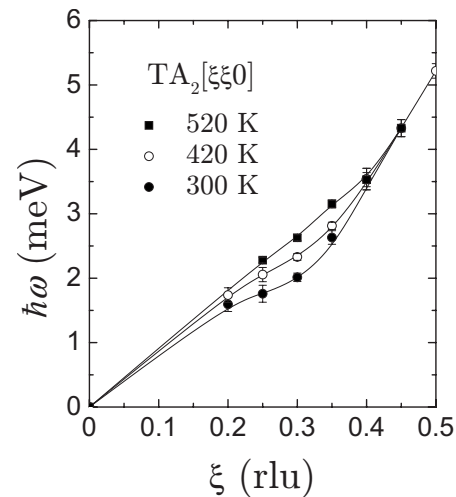


FIG. 3. Temperature dependence of the $\text{TA}_2[\xi \xi 0]$ branch. The wiggle at $\xi_0 \approx 0.33$ deepens with decreasing temperature thus reflecting the softening of the anomalous phonon. Solid lines are guides to the eye.

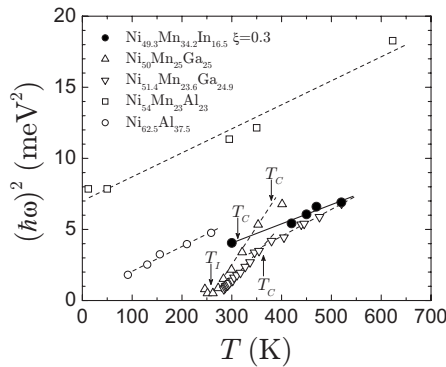


FIG. 4. Temperature dependence of the energy squared of the $TA_2[\xi\xi 0]$ phonon modes close to the anomalous phonon, $\xi=0.3$ (filled circles). Data from related systems Ni_2MnGa , $Ni_{54}Mn_{23}Al_{23}$, and $Ni_{62.5}Al_{37.5}$ are also shown for comparison. T_l represents the premartensitic transition temperature. The data for the latter systems were taken from Refs. 11, 12, 14, and 26 for $Ni_{50}Mn_{25}Ga_{25}$, $Ni_{51.4}Mn_{23.6}Ga_{24.9}$, $Ni_{54}Mn_{23}Al_{23}$, and $Ni_{62.5}Al_{37.5}$, respectively. Lines are linear fits to the experimental data.

tions. It should be noted that despite of the fact that the sample transforms martensitically near room temperature, the wiggle present at high temperatures does not develop into a marked dip even at 300 K. This behavior differs from that observed in Ni-Mn-Ga alloys^{10–13} but is similar to that previously reported in a Ni-Mn-Al alloy close to stoichiometry.¹⁴

In order to compare the behavior of the different Ni-Mn-based systems, we have plotted in Fig. 4 the energy squared of the anomalous phonons as a function of temperature for different compounds. Additionally, the data for the soft phonon in $Ni_{62.5}Al_{37.5}$ alloy are also plotted. As can be seen from the figure, the degree of softening in the studied sample is similar to that of $Ni_{62.5}Al_{37.5}$ and $Ni_{54}Mn_{23}Al_{23}$, although the energy values of the latter are higher, which is consistent with the fact that the Ni-Mn-Al sample does not transform martensitically within the studied temperature range. By contrast, Ni_2MnGa alloys show a more complex behavior. While the degree of softening in the paramagnetic state is similar to the studied sample and to the other related alloys, the softening below the Curie point is much stronger. This is due to strong spin-phonon coupling exhibited by these compounds in the ferromagnetic state.^{27,28} It should be noted that, despite the fact that the studied Ni-Mn-In sample is also ferromagnetic, changes in the degree of softening below T_C were not discernible due to the closeness of the magnetic and the structural transitions.

The measured dispersion curves are in good agreement with those obtained from *ab initio* calculations for the [110] direction in Ni_2MnIn ,²² except for the low energy transverse TA_2 branch, which exhibits complete softening in the range between $\xi=0.25$ and $\xi=0.45$. Experimental data are in agreement with such an instability and show that the minimum is located at $\xi_0 \approx 0.33$. However, it can be seen from Fig. 3 that the softening is not complete, i.e., the phonon frequency remains finite even at the lowest temperatures.

As mentioned above, the large shift of the structural martensitic transition with the applied magnetic field in these

compounds enables the phase transition to be induced by applying a magnetic field.⁵ The microscopic origin of such strong dependence of the transition temperature on the magnetic field is ascribed to a strong magnetoelastic coupling, which is responsible for the change in the relative stability of the martensitic and cubic phases when the field is applied. Actually, recent *ab initio* calculations at 0 K for cubic Ni_2MnIn have shown that increasing the magnetization due to an external magnetic field leads to a gradual vanishing of the phonon instability due to the coupling between vibrational and magnetic degrees of freedom.²³ We measured the transverse phonon branch TA_2 in the region close to the anomalous phonon at several applied magnetic fields and at temperatures slightly above the structural transition. Our results show no significant changes in the phonon energy with the applied field, so that, for these applied fields, the results cannot confirm the *ab initio* predictions. However, it should be noted that the magnetic fields involved in the calculations are considerably larger than the fields attainable experimentally in our measurements.²⁹ Moreover, it should be also noted that the close proximity of the magnetic and structural transitions in $Ni_{49.3}Mn_{34.2}In_{16.5}$ could inhibit the development of the necessary strong magnetoelastic coupling before the martensitic transformation takes place and, hence, prevent the observation of the predicted magnetic-field-induced behavior.

C. Elastic constants

In order to complement the study in the long-wavelength range, we have measured the elastic constants using the pulse-echo technique. The results of the temperature-dependent elastic constants measurements are shown in Fig. 5, where the thermal behavior of the three independent elastic constants C_{11} , C_L , and C_{44} is shown. These are computed from ultrasonic waves propagating along the [001] and the [110] directions down to temperatures close to the martensitic transformation. The data correspond to cooling (open circles) and heating (solid circles) runs and are obtained as an average over several independent runs. As can be seen from the figure, all three elastic constants increase with decreasing temperature reflecting the stiffening of the lattice as the temperature is lowered. C_{11} depends weakly on temperature, similar to the behavior reported for the related systems Ni-Mn-Ga (Ref. 18) and Ni-Mn-Al.¹⁹ Additionally, it should be noted that the elastic moduli show no significant changes at the Curie point, $T_C=310$ K. This behavior agrees with that reported in the ferromagnetic Ni-Mn-Ga alloys¹⁸ but differs from the behavior displayed by the antiferromagnetic Ni-Mn-Al system. In the latter case, antiferromagnetic ordering leads to a decrease in the elastic constants.¹⁹ We also note that similar features have been observed in other antiferromagnetic systems such as chromium,³⁰ Fe-Mn, and Co-Mn (Refs. 31 and 32) below their Néel temperatures. Thus, the type of magnetic order developed in the system appears to influence the elastic properties, although more studies are required in order to clarify this point.

From the complete set of measured elastic constants shown in Fig. 5, we can compute the temperature depen-

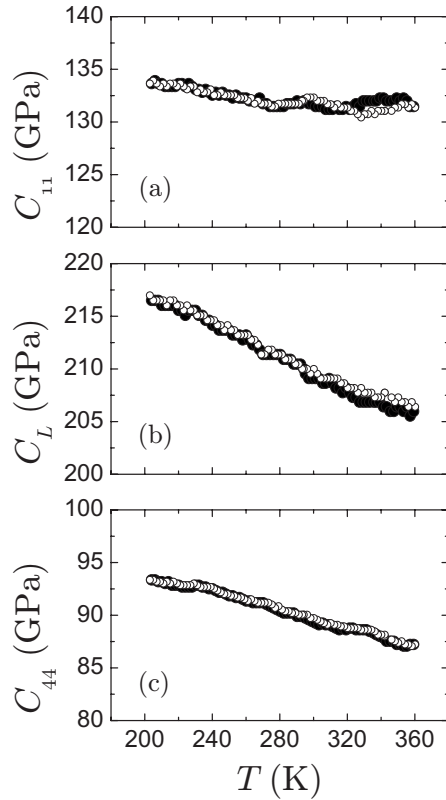


FIG. 5. Temperature dependence of the elastic moduli (a) C_{11} , (b) $C_L=(C_{11}+C_{12}+2C_{44})/2$, and (c) C_{44} . Open and solid symbols stand for cooling and heating runs, respectively.

dence of other relevant elastic moduli. Figure 6(a) shows the temperature dependence of the shear elastic constant C' computed as $C_{11}+C_{44}-C_L$. Owing to the strong attenuation of the shear waves associated with this mode, it was not possible to obtain reliable echoes and therefore to measure C' directly. As can be seen from Fig. 6(a), C' exhibits a low value and softens with decreasing temperature. Again, these features reflect the dynamical instability of the cubic lattice against shearing of $\{110\}$ planes along $\langle 1\bar{1}0 \rangle$ directions. Additionally, Fig. 6(b) shows the temperature dependence of the elastic anisotropy calculated as $A=C_{44}/C'$. The elastic anisotropy at room temperature is similar to those reported for the related systems Ni-Mn-Ga (Ref. 18) and Ni-Mn-Al,¹⁹ but significantly lower than for Cu-based shape memory alloys.³³

Up to now, we have discussed the behavior of the elastic constants of the Ni-Mn-In alloy obtained from ultrasonic methods. Elastic constants can also be derived from the initial slope ($\xi \rightarrow 0$) of the acoustic phonon branches reported in Sec. III B. Table I summarizes the elastic constants obtained from both experiments. As can be seen, both methods agree well on the values of C_{44} and C' . There is less agreement on the values for the longitudinal constants C_{11} and C_L , which correspond to the initial slope of the $L[\xi 00]$ and the $L[\xi\xi 0]$ branches, respectively, for which the values obtained from the dispersion branches are affected by a large error due to limited experimental data. Additionally, our experimental results are in good agreement with elastic constants obtained from first-principles calculations in the stoichiometric

TABLE I. Elastic constants obtained both from ultrasonic methods at 300 K and from the initial slopes of the acoustic phonon branches ($\xi \rightarrow 0$) at 520 K. Values determined experimentally show the associated uncertainty. The calculated values, corresponding to the stoichiometric Ni₂MnIn sample, were estimated from the phonon branches obtained from *ab initio* calculations (Ref. 22).

	Ultrasounds (GPa)	Neutrons (GPa)	<i>Ab initio</i> (GPa)
C_{11}	132 ± 8	190 ± 15	121
C_L	210 ± 10	260 ± 50	207
C_{44}	90 ± 3	90 ± 15	101
C'	12	12 ± 4	15

Ni₂MnIn.²² Again, discrepancies may arise from the definition of the initial slope, but note that these can also arise from changes in sample composition and temperature.

Finally, to investigate further the interplay between elastic and magnetic properties, we measured the elastic constants as a function of applied magnetic field at constant temperature. Results presented in Fig. 7 show the magnetic-field dependence of the relative change in the elastic constants at $T=260$ K with respect to the zero-field value. The temperature is located well below the Curie point of the studied sample, $T_C=310$ K. Note that, in this case, the ferromagnetic and the structural transitions are well separated [Fig. 1(b)] and thus significant magnetoelastic coupling is expected in contrast to the case for the sample studied by means of neutron scattering experiments (Sec. III B). As can be seen from Fig. 7, all elastic constants increase up to a saturation value with increasing magnetic field. This behavior is similar to that reported for the prototypical ferromag-

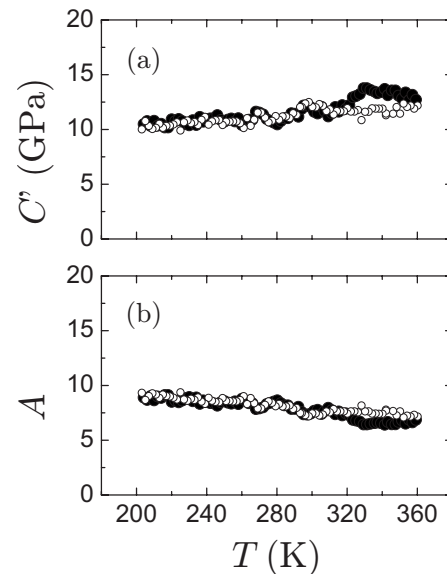


FIG. 6. (a) Temperature dependence of the shear elastic constant C' ($=C_{11}+C_{44}-C_L$) and (b) the elastic anisotropy $A=C_{44}/C'$ calculated from the complete set of measured elastic constants (shown in Fig. 5). Open and solid symbols stand for cooling and heating runs, respectively.

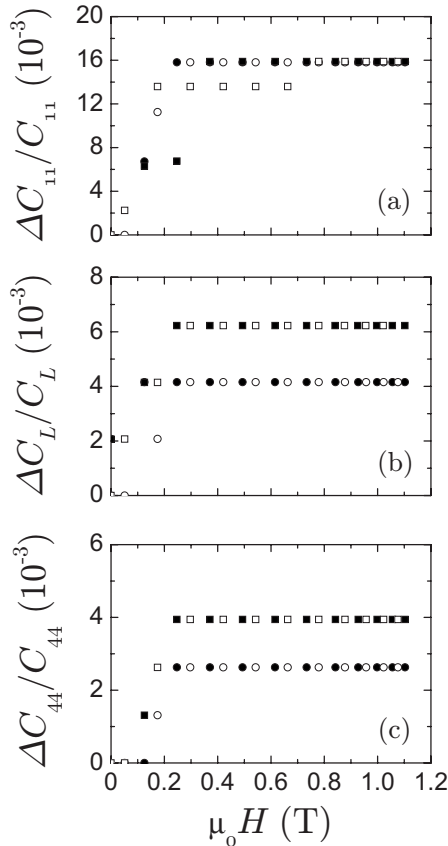


FIG. 7. Magnetic-field dependence of the relative change in the elastic constants with respect to the value at zero field at $T = 260$ K. (a) C_{11} versus applied magnetic field along $[110]$ (circle symbols) and $[1\bar{1}0]$ (square symbols). (b) C_L versus applied magnetic field along $[001]$ (circle symbols) and $[110]$ (square symbols). (c) C_{44} versus applied magnetic field along $[001]$ (circle symbols) and $[1\bar{1}0]$ (square symbols). Solid and open symbols correspond to increasing and decreasing magnetic-field runs, respectively.

netic shape memory alloy Ni-Mn-Ga (Ref. 21) but differs from the observed behavior in the antiferromagnetic Ni-Mn-Al system, which shows an anisotropic magnetoelastic coupling.¹⁹ As discussed before, the type of magnetic order present in the different compounds of the Ni-Mn-based family influences their elastic properties, as reflected by the different temperature dependence of the elastic constants across the magnetic transition.^{18,19} Additionally, the magnetic-field dependence of the elastic moduli further evidences the dependence of the elastic properties on the type of magnetic ordering indicating that the magnetic order also determines the magnetoelastic response of these alloy systems.^{19,21}

IV. SUMMARY AND CONCLUSIONS

We have carried out neutron scattering and ultrasonic experiments in order to study in detail the lattice dynamics of Ni-Mn-In Heusler alloys with composition close to the $\text{Ni}_{50}\text{Mn}_{34}\text{In}_{16}$ magnetic superelastic alloy. In order to study the interplay between dynamical and magnetic degrees of freedom, we performed both kinds of experiments in applied magnetic fields. The most relevant outcomes from this study are

(i) The values obtained for the elastic constants from both neutron scattering and ultrasonic experiments are in good agreement with each other. In addition, the data reported for the stoichiometric Ni_2MnIn from *ab initio* calculations are consistent with the measured values.

(ii) The TA_2 phonon branch exhibits a wiggle in the vicinity of $\xi_0 \approx 1/3$ at temperatures well above the Curie point. Upon cooling, this anomaly is enhanced but even at temperatures close to the martensitic transition the dip is less pronounced than in Ni-Mn-Ga.

(iii) The elastic constant C' also softens with decreasing temperature down to the martensitic transition. Both the anomalous phonon energy and C' have finite values at the transition temperature. The monotonic decrease in the anomalous phonon energy and in the elastic constant indicates the absence of a premartensitic phase (associated with the condensation of the anomalous phonon) in this alloy system.

(iv) Within experimental errors, the development of ferromagnetic order at the Curie point does not modify the rate of softening.

(v) While no magnetic-field dependence of phonon energies has been measured for fields up to 4 T, all elastic constants increase with increasing magnetic field, thus evidencing the existence of magnetoelastic coupling at the long-wavelength limit.

ACKNOWLEDGMENTS

This work received financial support from the CICYT (Spain) Project No. MAT2007-62100 and from the Deutsche Forschungsgemeinschaft (Grant No. SPP 1239). X.M. acknowledges support from Comissionat per a Universitats i Recerca (CUR) del Departament d'Innovació, Universitat i Empresa de la Generalitat de Catalunya. Experiments at Oak Ridge National Laboratory's High Flux Isotope Reactor were sponsored by the Scientific User Facilities Division, Office of Basic Energy Sciences, U.S. Department of Energy. Work at the Ames Laboratory was supported by the Office of Basic Energy Sciences U.S. DOE under Contract No. DE-AC02-07CH11358.

*Present address: Department of Materials Science and Metallurgy, University of Cambridge, Pembroke Street, Cambridge CB2 3QZ, UK.

†lluis@ecm.ub.es

¹Y. Sutou, Y. Imano, N. Koeda, T. Omori, R. Kainuma, K. Ishida, and K. Oikawa, *Appl. Phys. Lett.* **85**, 4358 (2004).

²T. Krenke, M. Acet, E. F. Wassermann, X. Moya, L. Mañosa, and A. Planes, *Phys. Rev. B* **72**, 014412 (2005).

- ³T. Krenke, M. Acet, E. F. Wassermann, X. Moya, L. Mañosa, and A. Planes, *Phys. Rev. B* **73**, 174413 (2006).
- ⁴T. Krenke, E. Duman, M. Acet, E. F. Wassermann, X. Moya, L. Mañosa, and A. Planes, *Nature Mater.* **4**, 450 (2005).
- ⁵T. Krenke, E. Duman, M. Acet, E. F. Wassermann, X. Moya, L. Mañosa, A. Planes, E. Suard, and B. Ouladdiaf, *Phys. Rev. B* **75**, 104414 (2007).
- ⁶Z. D. Han, D. H. Wang, C. L. Zhang, S. L. Tang, B. X. Gu, and Y. W. Du, *Appl. Phys. Lett.* **89**, 182507 (2006).
- ⁷X. Moya, L. Mañosa, A. Planes, S. Aksoy, M. Acet, E. F. Wassermann, and T. Krenke, *Phys. Rev. B* **75**, 184412 (2007).
- ⁸A. Planes, L. Mañosa, and M. Acet, *J. Phys.: Condens. Matter* **21**, 233201 (2009).
- ⁹V. K. Sharma, M. K. Chattopadhyay, K. H. B. Shaeb, A. Chouhan, and S. B. Roy, *Appl. Phys. Lett.* **89**, 222509 (2006).
- ¹⁰A. Zheludev, S. M. Shapiro, P. Wochner, A. Schwartz, M. Wall, and L. E. Tanner, *Phys. Rev. B* **51**, 11310 (1995).
- ¹¹A. Zheludev, S. M. Shapiro, P. Wochner, and L. E. Tanner, *Phys. Rev. B* **54**, 15045 (1996).
- ¹²U. Stuhr, P. Vorderwisch, V. V. Kokorin, and P.-A. Lindgrård, *Phys. Rev. B* **56**, 14360 (1997).
- ¹³L. Mañosa, A. Planes, J. Zarestky, T. Lograsso, D. L. Schlagel, and C. Stassis, *Phys. Rev. B* **64**, 024305 (2001).
- ¹⁴X. Moya, L. Mañosa, A. Planes, T. Krenke, M. Acet, V. O. Garlea, T. A. Lograsso, D. L. Schlagel, and J. L. Zarestky, *Phys. Rev. B* **73**, 064303 (2006).
- ¹⁵T. Mehaddene, J. Neuhaus, W. Petry, K. Hradil, P. Bourges, and A. Hiess, *Phys. Rev. B* **78**, 104110 (2008).
- ¹⁶J. Worgull, E. Petti, and J. Trivisonno, *Phys. Rev. B* **54**, 15695 (1996).
- ¹⁷L. Mañosa, A. González-Comas, E. Obradó, A. Planes, V. A. Chernenko, V. V. Kokorin, and E. Cesari, *Phys. Rev. B* **55**, 11068 (1997).
- ¹⁸M. Stipcich, L. Mañosa, A. Planes, M. Morin, J. Zarestky, T. Lograsso, and C. Stassis, *Phys. Rev. B* **70**, 054115 (2004).
- ¹⁹X. Moya, L. Mañosa, A. Planes, T. Krenke, M. Acet, M. Morin, J. L. Zarestky, and T. A. Lograsso, *Phys. Rev. B* **74**, 024109 (2006).
- ²⁰A. Planes and L. Mañosa, *Solid State Phys.* **55**, 159 (2001).
- ²¹A. González-Comas, E. Obradó, L. Mañosa, A. Planes, V. A. Chernenko, B. J. Hattink, and A. Labarta, *Phys. Rev. B* **60**, 7085 (1999).
- ²²A. T. Zayak, P. Entel, K. M. Rabe, W. A. Adeagbo, and M. Acet, *Phys. Rev. B* **72**, 054113 (2005).
- ²³P. Entel, M. E. Gruner, W. A. Adeagbo, and A. T. Zayak, *Mater. Sci. Eng., A* **481-482**, 258 (2008).
- ²⁴Materials Preparation Center, Ames Laboratory, Ames IA 50011, USA, see www.mpc.ameslab.gov
- ²⁵Y. Lee, J. Y. Rhee, and B. N. Harmon, *Phys. Rev. B* **66**, 054424 (2002).
- ²⁶S. M. Shapiro, B. X. Yang, Y. Noda, L. E. Tanner, and D. Schryvers, *Phys. Rev. B* **44**, 9301 (1991).
- ²⁷A. Planes, E. Obradó, A. González-Comas, and L. Mañosa, *Phys. Rev. Lett.* **79**, 3926 (1997).
- ²⁸M. A. Uijttewaal, T. Hickel, J. Neugebauer, M. E. Gruner, and P. Entel, *Phys. Rev. Lett.* **102**, 035702 (2009).
- ²⁹M. E. Gruner (private communication).
- ³⁰W. C. Muir, J. M. Perz, and E. Fawcett, *J. Phys. F: Met. Phys.* **17**, 2431 (1987).
- ³¹M. Cankurtaran, G. A. Saunders, P. Ray, Q. Wang, U. Kawald, J. Pelzl, and H. Bach, *Phys. Rev. B* **47**, 3161 (1993).
- ³²U. Kawald, O. Mitze, H. Bach, J. Pelzl, and G. A. Saunders, *J. Phys.: Condens. Matter* **6**, 9697 (1994).
- ³³A. Planes, L. Mañosa, and E. Vives, *Phys. Rev. B* **53**, 3039 (1996).

3.5 Paper 2: Stress- and field-induced entropy changes in Fe-doped Ni–Mn–Ga shape-memory alloys

Resum

En el límit d'esforços baixos i camps magnètics febles, s'ha mesurat el canvi d'entropia isotherm induït per esforç i per camp magnètic en un aliatge de Ni–Mn–Ga dopat amb Fe. S'ha obtingut que en aquest límit l'efecte elastocalòric és convencional, donant lloc a un increment d'entropia quan s'aplica un esforç, mentre que el magnetocalòric és invers, el que significa que l'entropia disminueix degut a l'aplicació d'un camp magnètic. Aquest efecte invers és conseqüència de l'acoblament magnetoestructural motivat per la transformació martensítica.

Stress- and magnetic field-induced entropy changes in Fe-doped Ni–Mn–Ga shape-memory alloys

D. E. Soto-Parra,^{1,a)} Eduard Vives,¹ David González-Alonso,¹ Lluís Mañosa,¹ Antoni Planes,^{1,a)} Ricardo Romero,² J. A. Matutes-Aquino,³ R. A. Ochoa-Gamboa,³ and H. Flores-Zúñiga^{3,b)}

¹Departament d'Estructura i Constituents de la Matèria, Facultat de Física, Universitat de Barcelona, Diagonal, 647, E-08028 Barcelona, Catalonia, Spain

²IFIMAT, Universidad Nacional del Centro de la Provincia de Buenos Aires and CICPBA, Pinto 399, 7000 Tandil, Argentina

³Centro de Investigación en Materiales Avanzados, S.C. Miguel de Cervantes 120, Complejo industrial Chihuahua, 31109 Chihuahua, Mexico

(Received 15 December 2009; accepted 13 January 2010; published online 18 February 2010)

Isothermal stress- and magnetic field-induced entropy changes in a Fe-doped Ni–Mn–Ga alloy have been measured in the limits of low applied stress and magnetic field. We have obtained that in this limit while elastocaloric is conventional, giving rise to an increase of entropy when a stress is applied, magnetocaloric effect is inverse, which means that entropy decreases by application of an applied magnetic field. This inverse effect is a consequence of the magnetostructural coupling driven by the martensitic transition. © 2010 American Institute of Physics. [doi:10.1063/1.3309755]

Ni–Mn–Ga close to the 2-1-1 stoichiometric composition is the archetypical Heusler alloy which shows a martensitic transformation with associated shape-memory properties.¹ The interest in this material arises from the fact that a large response to external stimuli is found in the vicinity of the transition. Actually, the coupling of magnetic and structural degrees of freedom enables a cross-variable response which means that both stress and magnetic field are effective in inducing the transition, giving rise to large deformations and changes of magnetization.² These changes provide additional fascinating properties to this class of materials such as elastocaloric³ and magnetocaloric⁴ properties, which are of interest for near-room-temperature refrigeration applications.⁵ Therefore, understanding magnetostructural coupling is not only important at a fundamental level, but, indeed, has important technological implications.

In the present letter we compare isothermal stress- and magnetic field-induced changes of entropy in Fe-doped Ni–Mn–Ga which have been obtained from thermomechanical and calorimetric (under applied magnetic field) measurements. Ni–Mn–Ga alloys are brittle materials, but Fe-addition enables improvement of its toughness without sacrificing its magnetic and thermoelastic properties.^{6,7} Entropy changes provide relevant information on the magnetostructural coupling mechanism and enable us to quantify elastocaloric and magnetocaloric effects in the studied material.

A polycrystalline Ni_{52.6}Mn_{21.9}Ga_{24.2}Fe_{1.3} ingot was obtained by arc melting pure metals under argon atmosphere. Slices cut from the ingot were encapsulated under vacuum in quartz glass and annealed at 1073 K for 72 h and quenched in ice water. The slices were then spark-machined into samples for thermomechanic and calorimetric measurements.

The studied alloy undergoes a martensitic transition at $M_s=327$ K (in the absence of applied stress and magnetic field). We checked the crystallographic structure by means of x-ray diffraction which revealed that the martensitic phase has a modulated (monoclinic) 14M structure.

Stress-induced entropy changes have been estimated from measurements of the elongation L of the sample during the temperature induced martensitic transition (L versus T) by keeping an applied uniaxial force F constant. For these experiments we used a standard flat specimen for tensile test experiments. The length of the sample gauge was $l=5.90$ mm and its cross-section $\phi=3.51$ mm². Special grips were designed to adapt to the specimen. The upper grip was attached to a load cell and the lower grip held a dead load (which enabled control of the applied force). Elongation was measured by a strain gauge attached to the sample. The setup was placed inside a cryofurnace in order to control temperature. In Fig. 1 we show examples of the measured L versus T curves during the forward martensitic transition on cooling at selected values of the force F corresponding to a stress $\sigma=F/\phi$ (the cross-section ϕ is assumed constant). From these curves the isothermal stress-induced entropy change is obtained using the expression

$$\Delta S(T, \sigma) = \int_0^\sigma \left(\frac{\partial S}{\partial \sigma} \right)_T d\sigma = \int_0^{F=\sigma\phi} \left(\frac{\partial L}{\partial T} \right)_F dF, \quad (1)$$

where the Maxwell relation

$$(\partial S / \partial \sigma)_T = V(\partial \varepsilon / \partial T)_\sigma = \phi(\partial L / \partial T)_F$$

($\varepsilon=L/l$ and $V=\phi l$ is the gauge volume) is taken into account. From data in Fig. 1, numerical computation of the above integral yields the stress-induced entropy changes⁸ depicted in Fig. 2. We obtain that application of a stress induces an entropy reduction (conventional elastocaloric behavior). This is indeed the expected behavior consistent with the fact that the martensitic transition is shifted to a higher temperature by application of a stress (see inset of Fig. 1). The magnitude of the entropy reduction increases with the applied

^{a)}Electronic addresses: enrique.soto.parra@gmail.com and antoniplanes@ub.edu.

^{b)}Permanent address: Instituto Potosino de Investigación Científica y Tecnológica, Camino a la Presa San José 2055. Col. Lomas 4 sección, 78216 San Luis Potosí, S.L.P. Mexico.

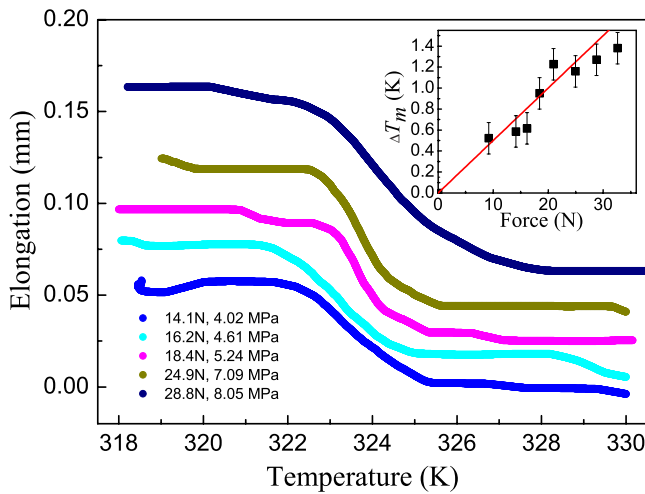


FIG. 1. (Color online) Elongation $L(T, \sigma)$ as a function of temperature in the region of the martensitic transition for selected values of the applied force. The inset shows the temperature change ΔT_m of the inflection point of the elongation curves as a function of the applied force.

stress and, for a given stress, shows a maximum close to the temperature T_m of the inflection point of the L versus T curves.

Isothermal magnetic field-induced entropy changes were obtained from calorimetric measurements. We have used a specially designed differential scanning calorimeter that enables application of magnetic fields up to 1 T, while temperature is swept at rates of ~ 0.5 K/min.⁹ A small sample of mass $m_c = 0.125$ g was used for these experiments. From the calorimetric curves the excess of entropy of the high-temperature phase was obtained as $S(T, H) = \int_{T_i}^T (1/T) (dq/dT) dT$, where dq/dT is the heat released per unit temperature and T is a temperature in the range between the start (M_s) and finish (M_f) of the martensitic transition and T_i is a temperature close to M_f . Entropy curves for selected values of the applied field are shown in Fig. 3. The isothermal magnetic field-induced entropy change is then computed as

$$\Delta S(T, H) = S(T, H) - S(T, H = 0). \quad (2)$$

The obtained entropy changes as a function of temperature for selected values of the magnetic field are given in Fig. 4. In this case application of a magnetic field induces an en-

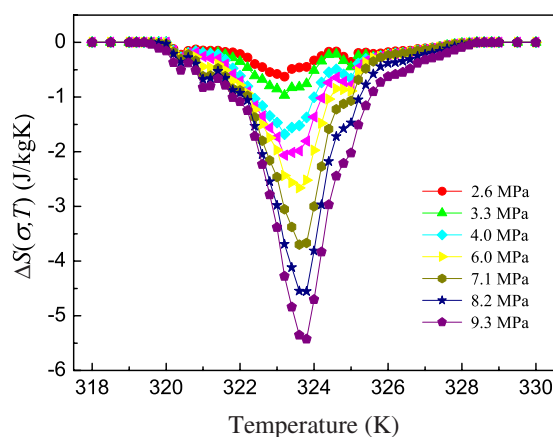


FIG. 2. (Color online) Stress-induced changes of entropy as a function of temperature for selected values of the applied force.

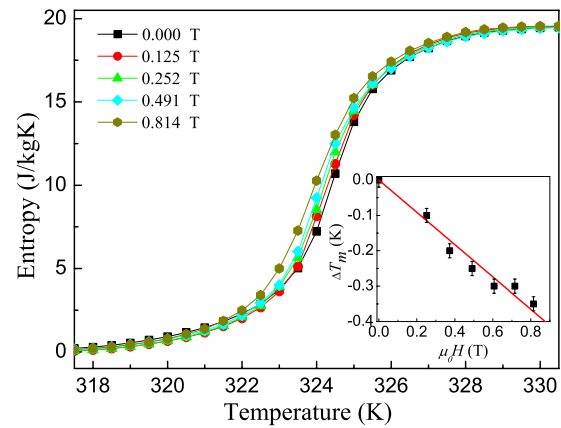


FIG. 3. (Color online) Entropy $S(T, \sigma)$ (referred to the entropy of the cubic phase) as a function of temperature in the region of the martensitic transition for selected values of the applied magnetic field. The inset shows the temperature change ΔT_m of the inflection point (calorimetric peak) as a function of the applied field.

trophy increase corresponding to an inverse magnetocaloric effect.⁴ Indeed this increase of entropy is consistent with the decrease of T_m (defined as the temperature of the calorimetric peak) with H (see inset of Fig. 3).

The obtained elastocaloric and magnetocaloric effects in the studied Fe-doped Ni-Mn-Ga alloys have their origin in the large changes of L and magnetization M which simultaneously occur at the martensitic transition. They are, respectively, quantified by the derivatives $(\partial L / \partial T)_{F, H}$ and $(\partial M / \partial T)_{H, F}$. In Fig. 5 we show the peak values ΔS_{\max} of the stress- and magnetic field-induced entropy change curves as a function of stress and magnetic field, respectively. In the studied range of applied generalized forces, both fields have the opposite effect on the corresponding induced entropy changes. A linear variation with rates $\Delta S_{\max} / \sigma \approx -0.5$ J/MPa K kg and $\Delta S_{\max} / \mu_0 H \approx 4.4$ J/T K kg is found. The maximum available induced entropy change associated with the martensitic transition should correspond to $\Delta S_c (= 19.5$ J/K kg). Linear extrapolations of data in Fig. 5 indicate that in the case of the elastocaloric effect this maximum entropy content should be reached for stresses $\sigma \geq 39$ MPa, while in the case of the magnetocaloric effect a magnetic field $\mu_0 H \geq 4.4$ T should be required. In this last case, however, linear extrapolation is not expected to provide a good estimation since it is well

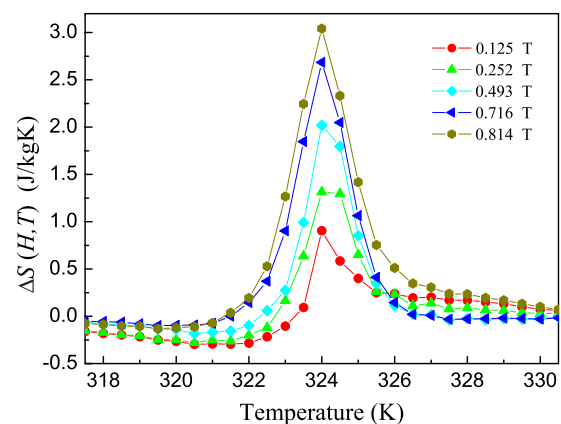


FIG. 4. (Color online) Magnetic field-induced changes of entropy as a function of temperature for selected values of the applied magnetic field.

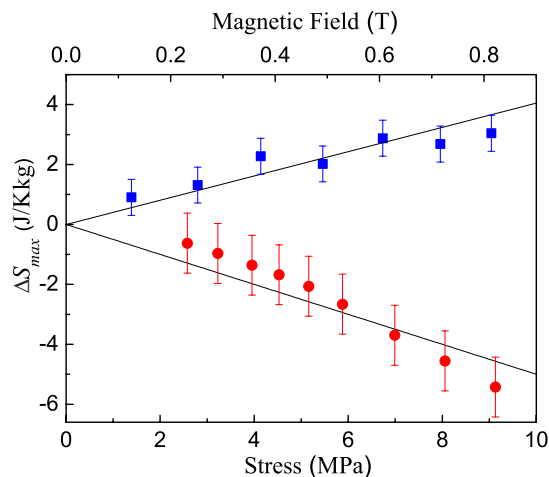


FIG. 5. (Color online) Peak values of the stress- and magnetic field-induced changes of entropy as a function of the applied stress and the applied magnetic field.

known that for high enough fields dT_m/dH becomes positive for alloys of composition close to the composition of the present studied system. For an alloy $\text{Ni}_{46.2}\text{Mn}_{20.2}\text{Ga}_{25.0}\text{Fe}_{1.0}$, it has been reported⁶ that for fields $\mu_0 H \geq 1.5$ T the transition temperature increases with the field at a rate $dT_m/d\mu_0 H \approx 0.78$ K/T. Therefore, the magnetic field-induced entropy change in this range of applied fields is expected to rise with increasing field. As in nearly stoichiometric Ni–Mn–Ga (Ref. 10) and Ni–Fe–Ga,¹¹ the inverse magnetocaloric effect observed in Fe-doped Ni–Mn–Ga for low applied fields is a consequence of an anomalous magnetization behavior due to the magnetostructural coupling. While in most systems undergoing magnetostructural transitions, the coupling between structure and magnetism arises from modifications of exchange interactions resulting from changes in lattice parameters,¹² in nearly stoichiometric Ni–Mn–Ga the coupling is, to a large extent, controlled by the symmetry induced change of magnetic anisotropy at the transition. This coupling is responsible for the magnetic shape-memory effect displayed by these materials.² Systems showing 10M and 14M martensitic structure (as present Fe-

doped Ni–Mn–Ga), are almost magnetically isotropic in the high temperature cubic phase and show large uniaxial anisotropy in the martensitic phase (with the easy axis along the short *c*-axis). This change of magnetic anisotropy gives rise to a reduction of the magnetization when the transition occurs at low applied fields. This reduction is responsible for the small decrease of transition temperature with magnetic field and thus for the inverse magnetocaloric effect, as obtained in the studied Fe-doped Ni–Mn–Ga alloy. A comparable small decrease of transition temperature at low applied magnetic fields was also reported in Ref. 13 for Ni–Mn–Ga transforming to a 14M structure.

This work was supported by CICYT (Spain) under Project No. MAT-2007-61200 and from CONACYT (44786-SEP-CONACYT 2003). The authors acknowledge O. Toscano from IFIMAT for experimental assistance.

¹K. Ullakko, J. K. Huang, C. Kantner, R. C. O'Handley, and V. V. Kokorin, *Appl. Phys. Lett.* **69**, 1966 (1996).

²O. Söderberg, A. Sozinov, Y. Ge, S.-P. Hannula, and V. K. Lindroos, in *Handbook of Magnetic Materials*, edited by K. H. J. Buschow (Elsevier, Amsterdam, 2006), pp. 1–39.

³E. Bonnot, R. Romero, L. Mañosa, E. Vives, and A. Planes, *Phys. Rev. Lett.* **100**, 125901 (2008).

⁴A. Planes, L. Mañosa, and M. Acet, *J. Phys.: Condens. Matter* **21**, 233201 (2009).

⁵K. A. Gschneidner, V. K. Pecharsky, and A. O. Tsokol, *Rep. Prog. Phys.* **68**, 1479 (2005).

⁶A. A. Cherechukin, I. E. Dikshtein, D. I. Ermakova, A. V. Glebova, V. V. Koledova, D. A. Kosolapov, V. G. Shavrov, A. A. Tulaikova, E. P. Krasnoperov, and T. Takagi, *Phys. Lett. A* **291**, 175 (2001).

⁷H. B. Wang, F. Chen, Z. Y. Gao, W. Cai, and L. C. Zhao, *Mater. Sci. Eng., A* **438-440**, 990 (2006).

⁸Entropy changes per unit mass are given using the mass of the sample gauge ρV . A mass density $\rho = 7.6$ g/cm³ has been estimated.

⁹The calorimeter used in the present study is a simplified version, adequate for near-room-temperature measurements, of the calorimeter described in J. Marcos, F. Casanova, X. Batlle, A. Labarta, A. Planes, and L. Mañosa, *Rev. Sci. Instrum.* **74**, 4768 (2003).

¹⁰J. Marcos, L. Mañosa, A. Planes, F. Casanova, X. Batlle, and A. Labarta, *Phys. Rev. B* **68**, 094401 (2003).

¹¹V. Recarte, J. I. Pérez-Landazábal, C. Gómez-Polo, E. Cesari, and J. Dutkiewicz, *Appl. Phys. Lett.* **88**, 132503 (2006).

¹²C. P. Bean and D. S. Rodbell, *Phys. Rev.* **126**, 104 (1962).

¹³J. Kim, F. Inaba, T. Fukuda, and T. Kakeshita, *Acta Mater.* **54**, 493 (2006).

3.6 Paper 3: Giant solid-state barocaloric effect in the Ni–Mn–In magnetic shape-memory alloy

Resum

La recerca de materials amb grans efectes calòrics a prop de temperatura ambient ha esdevingut un desafiament per a la física moderna de materials i s'espera que aquest tipus de materials proporcionin una manera de renovar els actuals dispositius de refrigeració basats en la compressió de vapor de gasos nocius. Fins ara, els materials més prometedors són materials magnetocalòrics gegants. El descobriment de materials amb un gran efecte magnetocalòric a temperatures properes a l'ambient ha obert la possibilitat d'usar-los per a la refrigeració. Per efectes calòrics volem dir el canvi d'entropia isoterm aconseguit mitjançant l'aplicació d'un camp extern, diversos efectes calòrics poden tenir lloc al variar diferents paràmetres externs, tal com ara la pressió i el camp elèctric. De fet, l'aparició de grans efectes electrocalòrics i elastocalòrics han estat recentment ressenyats. Aquí mostrem que l'aplicació d'una pressió hidrostàtica moderada a un aliatge amb memòria de forma magnètica dóna lloc a un efecte calòric d'una magnitud comparable a l'efecte magnetocalòric gegant ressenyada en aquest tipus de materials. Nosaltres anticipem que efectes barocalòrics similars ocorren en molts materials amb un efecte magnetocalòric gegant, tot experimentant transicions magnetoestructurals que impliquin un canvi de volum.

Giant solid-state barocaloric effect in the Ni-Mn-In magnetic shape-memory alloy

Lluís Mañosa^{1*}, David González-Alonso¹, Antoni Planes¹, Erell Bonnot², Maria Barrio², Josep-Lluís Tamarit², Seda Aksoy³ and Mehmet Acet³

The search for materials showing large caloric effects close to room temperature has become a challenge in modern materials physics and it is expected that such a class of materials will provide a way to renew present cooling devices that are based on the vapour compression of hazardous gases. Up to now, the most promising materials are giant magnetocaloric materials. The discovery of materials showing a giant magnetocaloric effect at temperatures close to ambient has opened up the possibility of using them for refrigeration^{1–3}. As caloric effects refer to the isothermal entropy change achieved by application of an external field, several caloric effects can take place on tuning different external parameters such as pressure and electric field. Indeed the occurrence of large electrocaloric^{4,5} and elastocaloric⁶ effects has recently been reported. Here we show that the application of a moderate hydrostatic pressure to a magnetic shape-memory alloy gives rise to a caloric effect with a magnitude that is comparable to the giant magnetocaloric effect reported in this class of materials. We anticipate that similar barocaloric effects will occur in many giant-magnetocaloric materials undergoing magnetostructural transitions involving a volume change.

The barocaloric effect refers to the isothermal entropy change or adiabatic temperature change on the application or withdrawal of an external pressure. This effect is used in most present cooling technologies that are based on the compression and expansion cycles of gases. On the other hand, barocaloric effects in the solid state have received little attention because the thermal effects were expected to be small. For example, the application of hydrostatic pressures of 5 kbar in a mixed crystalline compound ($\text{Pr}_{1-x}\text{La}_x\text{NiO}_3$) resulted in an effective cooling that was in competition with the elastic heating⁷. Application of uniaxial pressure slightly improved the measured values, but they were still close to those of elastic heating⁸. Here, we report a barocaloric effect of $24.4 \text{ J kg}^{-1} \text{ K}^{-1}$ under a hydrostatic pressure of 2.6 kbar, at temperatures close to room temperature. This value is 20 times larger than the value resulting from elastic heating. Moreover, the magnitude found for the barocaloric effect compares well to the best values reported in giant magnetocaloric materials^{9,10}, which are nowadays being considered as alternatives for room-temperature refrigeration.

Giant caloric effects are expected to occur when a material undergoes a first-order phase transition. The possibility of inducing the transition by varying external fields such as magnetic, electric and stress gives rise to the reported giant magnetocaloric, electrocaloric and elastocaloric effects. Recently, it

has been theoretically predicted^{11,12} that some giant magnetocaloric materials would also show giant barocaloric effects. On the other hand, experiments have shown that hydrostatic pressure affects the magnetocaloric properties of several materials^{13,14}. Here we directly measure the barocaloric effect resulting from the application of a hydrostatic pressure to a giant magnetocaloric material such as Ni–Mn–In.

Ni–Mn–Z (Z = Ga, In, Sn and Sb) alloys with compositions close to the stoichiometric Ni_2MnZ undergo a martensitic transformation from a high-temperature cubic (Heusler) structure to a close-packed martensitic phase¹⁵ of lower crystallographic symmetry. In relation to the martensitic transition, several important functional properties such as inverse magnetocaloric effects³, metamagnetic shape memory¹⁶, magnetic superelasticity¹⁷ and giant magnetoresistance¹⁸ have been reported in this alloy family. We recently studied the influence of hydrostatic pressure on the magnetic and structural properties of Ni–Mn–In shape-memory alloys¹⁹, and found that the properties of the martensitic transition were strongly affected by the application of hydrostatic pressure. This finding suggests that this material is a good candidate to show large barocaloric effects. As will be shown below, the physical origin of the large barocaloric effect found in this compound is the same as that reported for the inverse magnetocaloric effect: the large entropy change accompanying the structural (martensitic) transition, which can be induced either by magnetic field or by hydrostatic pressure, or even by a combination of both (multicaloric effect). In magnetocaloric materials it has been pointed out that the entropy of a structural transition has a key role in the appearance of the giant magnetocaloric effect²⁰. Our results suggest that such a situation should also hold for the appearance of other giant caloric effects.

In magnetic shape-memory alloys the martensitic transition temperature strongly depends on composition¹⁵. For the present study we selected a sample with a martensitic transition temperature close to room temperature, so that the desired caloric effect occurs in a temperature range useful for practical applications. Figure 1 shows low-field magnetization data recorded in zero-field-cooling, field-cooling and field-heating sequences. On cooling there is a sharp increase in magnetization at the ferromagnetic ordering temperature of the cubic phase, which is followed by a decrease at the martensitic transition. The small thermal hysteresis between field-cooling and field-heating sequences is associated with the first-order character of the martensitic transition, whereas the splitting between zero-field-cooling and field-cooling curves is indicative of the coexistence of antiferromagnetic and ferromagnetic exchange correlations in the martensitic state²¹.

¹ Departament d'Estructura i Constituents de la Matèria, Facultat de Física, Universitat de Barcelona, Diagonal 647, Barcelona Knowledge Campus (BKC), 08028 Barcelona, Catalonia, ²Departament de Física i Enginyeria Nuclear, ETSEIB, Universitat Politècnica de Catalunya, Diagonal 647 and Center for Research in NanoEngineering, Pascual i Vila, 15, Barcelona Knowledge Campus (BKC), 08028 Barcelona, Catalonia, ³Experimentalphysik, Universität Duisburg-Essen, D-47048 Duisburg, Germany. *e-mail: lluis@ecm.ub.es.

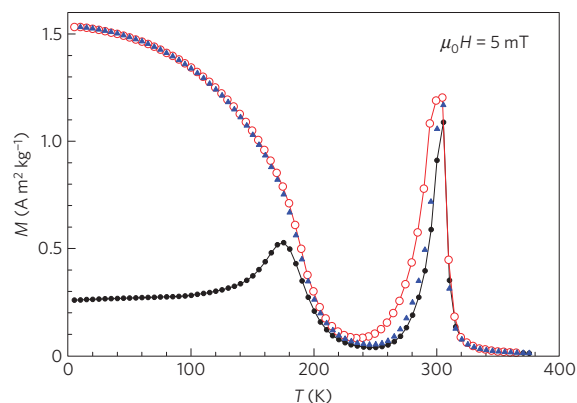


Figure 1 | Temperature dependence of the magnetization. Low-field magnetization as a function of temperature. Data are taken in the zero-field-cooling (filled circles), field-cooling (open circles) and field-heating (triangles) sequences.

Caloric effects are usually quantified by isothermal entropy changes, which are computed using the Maxwell relations from measurements of an extensive quantity (magnetization, polarization and so on) while its conjugated thermodynamic generalized field (magnetic, electric and so on) is isothermally swept. In the study of the solid-state barocaloric effect this method is not readily feasible because the involved volume changes are small and they cannot be measured with the precision required to obtain reliable entropy data. The best-suited method is to directly measure the entropy change by a calorimetric technique. This technique has been shown to be very appropriate in the study of the magnetocaloric effect in giant magnetocaloric materials^{22,23}. We have used a purpose-built calorimeter that operates under hydrostatic pressures up to 3 kbar. To study the magnetocaloric effect and relate the data to the barocaloric effect, we have used a second purpose-built calorimeter that operates under magnetic fields up to 1 T. Figure 2 shows the thermal curves as a function of temperature, obtained during cooling at selected values of the hydrostatic pressure (Fig. 2a) and magnetic field (Fig. 2b). A clear exothermal peak is observed corresponding to the latent heat of the martensitic transition. For conciseness, only results during cooling runs will be presented in this work. On heating, an endothermal peak is obtained at about 300 K (not shown here). From the calorimetric data, the entropy (S) change (referenced to a given state at T_0), is computed as²⁴:

$$S(T, Y) - S(T_0, Y) = \int_{T_0}^T \frac{1}{T} \frac{\dot{Q}(Y)}{\dot{T}} dT$$

where $\dot{Q}(Y)$ is the heat flux, \dot{T} is the cooling rate and Y refers either to hydrostatic pressure p or to magnetic field H . The results obtained are shown in Fig. 3a,b ($T_0 = 300$ K). When the material undergoes the transition from the cubic to the martensitic phase, the entropy smoothly decreases down to a plateau close to $-27 \pm 3 \text{ J kg}^{-1} \text{ K}^{-1}$. This value is the martensitic transition entropy change obtained by conventional differential scanning calorimetry at atmospheric pressure and in the absence of a magnetic field. There is a systematic shift of the entropy curves towards higher temperatures as the hydrostatic pressure increases, whereas they shift to lower temperatures with increasing magnetic field. Such a shift is more clearly seen in the insets of Fig. 3a and b, which show the temperature of the peak in the calorimetric curves (Fig. 2a and b) as a function of pressure and magnetic field, respectively. It is found that hydrostatic pressure stabilizes the martensitic phase whereas magnetic field stabilizes the cubic phase. From the insets in Fig. 3 we obtain the following changes in the transition

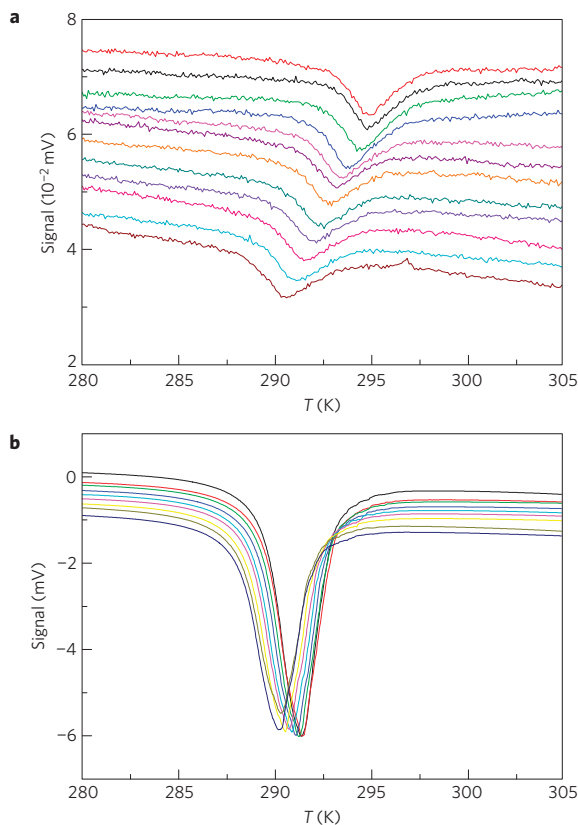


Figure 2 | Calorimetric signal as a function of temperature.

a,b. Calorimetric curves at selected values of hydrostatic pressure (**a**) and magnetic field (**b**). The curves have been vertically displaced for clarity. From top to bottom the curves correspond to 2.6, 2.45, 2.3, 2.0, 1.8, 1.6, 1.4, 1.2, 1.0, 0.8, 0.4 and 0.2 kbar in **a** and 0, 0.19, 0.27, 0.36, 0.47, 0.59, 0.70, 0.87 and 0.94 T in **b**.

temperature with pressure and field: $dT/dp = 1.8 \pm 0.2 \text{ K kbar}^{-1}$ and $dT/d(\mu_0 H) = -1.4 \pm 0.2 \text{ K T}^{-1}$.

The caloric effect at each temperature (ΔS) is calculated as the difference between the data at different pressure and magnetic-field values in Fig. 3a and b, respectively. Results are presented in Fig. 4a for the barocaloric effect and 4b for the magnetocaloric effect. It is worth noting that the isothermal application of pressure results in a decrease of entropy whereas application of a magnetic field results in an entropy increase. This result is consistent with the fact that pressure stabilizes the martensitic phase whereas magnetic field stabilizes the cubic phase. In spite of the small scatter of the data at low temperature, it is apparent that a large caloric effect is obtained in both cases. The values found for the entropy change compare well to those reported in other giant caloric materials such as giant magnetocaloric materials, electrocaloric and elastocaloric materials. On the other hand, it is important to note that the value found for the barocaloric effect at 2.6 kbar ($24.4 \text{ J kg}^{-1} \text{ K}^{-1}$) is about 20 times larger than the effect corresponding to elastic heating ($\approx \beta v \Delta p = 1.2 \text{ J kg}^{-1} \text{ K}^{-1}$), where $\beta = 3.7 \times 10^{-5} \text{ K}^{-1}$ is the thermal expansion and $v = 1.22 \times 10^{-4} \text{ m}^3 \text{ kg}^{-1}$ is the specific volume²⁵.

The peak values of ΔS in Fig. 4a,b, systematically increase (in absolute value) with increasing pressure and field. The maximum value for the external-field-induced entropy change would correspond to the transition entropy change ($27 \text{ J kg}^{-1} \text{ K}^{-1}$). The values achieved by moderate pressures of 2.6 kbar are already very close to the maximum attainable barocaloric effect. The temperature change associated with an adiabatic sweep of the

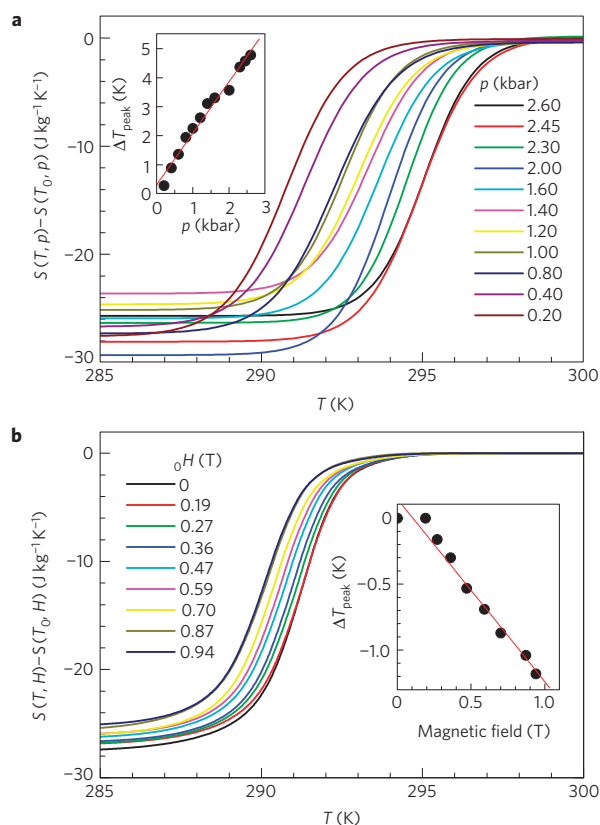


Figure 3 | Entropy as a function of temperature. **a, b**, Entropy values, referred to the value at ambient temperature, for selected values of hydrostatic pressure (**a**) and magnetic field (**b**). The insets show the shift in the temperature of the peak in the calorimetric curves as a function of hydrostatic pressure (**a**) and magnetic field (**b**).

external field can be computed from the shift in the curves shown in Fig. 3. For a hydrostatic pressure of 2.6 kbar, $\Delta T \approx 4.5$ K is obtained, and for a magnetic field of 0.94 T, $\Delta T \approx 1.3$ K. These values are comparable to 6–7 K for the prototype giant magnetocaloric material Gd–Si–Ge (magnetic field of 2 T; ref. 9) or 12 K for the electrocaloric material $\text{PbZr}_{0.95}\text{Ti}_{0.05}\text{O}_3$ (electric field of 480 kV cm^{-1} ; ref. 4). A significant figure of merit for cooling applications is the refrigerating cooling power ($RCP \approx \nu^{-1} \Delta S \Delta T$), which is expressed in terms of energy per volume⁹. From the barocaloric data at 2.6 kbar, $RCP \approx 1 \text{ J cm}^{-3}$. It is worth noting that to achieve a similar RCP value, magnetic fields around 3.5 T would be required, which are not readily available with permanent magnets, whereas pressures up to 3 kbar are accessible by present technologies.

The large barocaloric effect found in Ni–Mn–In is a consequence of the volume and entropy discontinuities at a magnetostructural transition. This material also shows a large magnetocaloric effect. Actually, we can anticipate that large barocaloric effects will also be encountered in many giant magnetocaloric materials. In all of these materials, the large entropy content arises from magnetic first-order phase transitions. In magnetic systems showing time-reversal symmetry (which implies invariance under magnetization inversion) the first-order character of the transition requires a coupling to a secondary field²⁸, which is typically achieved through the coupling of magnetic exchange energy and interatomic distances. In the Ni–Mn–In alloy studied in this work, exchange interactions have been shown to be of Ruderman–Kittel–Kasuya–Yosida type^{29,30}, which are sensitive to changes in the atomic

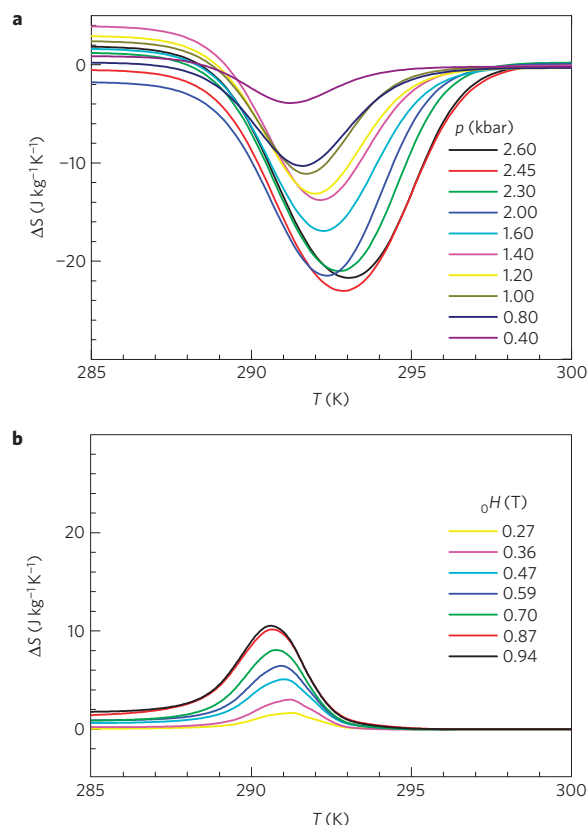


Figure 4 | Caloric effects in Ni–Mn–In. **a, b**, Barocaloric (**a**) and magnetocaloric (**b**) effects as a function of temperature, associated with the isothermal application of selected hydrostatic pressures (from $p = 0.2$ kbar up to the indicated value) and magnetic fields (from $H = 0$ up to the indicated value), respectively.

distances. In particular, the crystallographic symmetry reduction just below the martensitic transition is accompanied by a symmetry increase in the magnetic configuration. This is associated with an increase in the magnetic entropy, and can occur only in connection with the large volume decrease, which is responsible for the large barocaloric effect. Note also that the magnetic symmetry increase at the transition is at the origin of the inverse magnetocaloric effect shown by Ni–Mn–In. We anticipate that the reported barocaloric effect will inspire commercial applications for efficient and accurate solid-state refrigerating devices at ambient temperature. For instance, as both barocaloric and magnetocaloric effects occur in a single material, an accurate control of the temperature change could be achieved by fine tuning several external parameters. This advantage should result in more efficient and accurate cooling devices.

Methods

Ingot was prepared by arc melting the pure metals under argon atmosphere in a water-cooled copper crucible; the composition was determined by energy-dispersive X-ray photoluminescence analysis to correspond to $\text{Ni}_{49.26}\text{Mn}_{36.08}\text{In}_{14.66}$. The sample was encapsulated under argon in quartz glass and annealed at 1,273 K for two hours and subsequently quenched in an ice–water mixture. Magnetization measurements were carried out using a superconducting quantum interference device magnetometer. Calorimetric measurements were carried out using purpose-built calorimeters. Hydrostatic pressure calorimetry was carried out in a calorimeter similar to that described in ref. 26. The calorimetric block, made of a copper–beryllium alloy, is surrounded by an external heating and cooling vessel for temperature control. The temperature of the calorimeter is controlled by a Pt-100 thermometer embedded into the block. Samples were mixed with an inert perfluorinated liquid before they were hermetically sealed into Sn cells to ensure

pressure transmission and to ascertain that in-cell volumes were free from residual air. Thermal sensors consist of type-K (chromel–alumel) thermocouples deeply inserted into the Sn sample and reference cells. The pressure into the calorimetric block was transmitted by compressing a cryogenic liquid and measured by calibrated Bourdon gauges with an accuracy better than 5 bar. Calorimetry under magnetic field was carried out in a calorimeter adapted from that described in ref. 27. The thermal sensors are batteries of thermocouples differentially connected. The sample is directly placed in contact with one of the sensors and a dummy sample is placed on the second sensor. The body of the calorimeter (copper block) is placed within the poles of an electromagnet, and is in thermal contact with a copper cylinder. The temperature of the calorimeter is controlled by a Pt-100 thermometer embedded into the block. A cryogenic fluid circulates through the copper cylinder and enables temperature control within the range 200–350 K. All heating and cooling runs were carried out at typical rates of about 1 K min^{-1} , and acquisition rates were 0.2 Hz and 0.5 Hz for the runs under pressure and magnetic field, respectively.

Received 18 December 2009; accepted 23 February 2010;
published online 4 April 2010

References

- Pecharsky, V. K. & Gschneidner, K. A. Jr Giant magnetocaloric effect in $\text{Gd}_5\text{Si}_2\text{Ge}_2$. *Phys. Rev. Lett.* **78**, 4494–4497 (1997).
- Tegus, O., Brück, E., Buschow, K. H. J. & de Boer, F. R. Transition-metal-based magnetic refrigerants for room-temperature applications. *Nature* **415**, 150–152 (2002).
- Krenke, T. *et al.* Inverse magnetocaloric effect in ferromagnetic Ni–Mn–Sn alloys. *Nature Mater.* **4**, 450–454 (2005).
- Mischenko, A. S., Zhang, Q., Scott, J. F., Whatmore, R. W. & Mathur, N. D. Giant electrocaloric effect in thin-film $\text{PbZr}_{0.95}\text{Ti}_{0.05}\text{O}_3$. *Science* **311**, 1270–1271 (2006).
- Neese, B. *et al.* Large electrocaloric effect in ferroelectric polymers near room temperature. *Science* **321**, 821–823 (2008).
- Bonnot, E., Romero, R., Mañosa, L., Vives, E. & Planes, A. Elastocaloric effect associated with the martensitic transition in shape-memory alloys. *Phys. Rev. Lett.* **100**, 125901 (2008).
- Müller, K. A. *et al.* Cooling by adiabatic pressure application in $\text{Pr}_{1-x}\text{La}_x\text{NiO}_3$. *Appl. Phys. Lett.* **73**, 1056–1058 (1998).
- Strässle, Th., Furrer, A., Hossain, Z. & Geibel, Ch. Magnetic cooling by application of external pressure in rare-earth compounds. *Phys. Rev. B* **67**, 054407 (2003).
- Gschneidner, K. A., Pecharsky, V. K. & Tsokol, A. O. Recent developments in magnetocaloric materials. *Rep. Prog. Phys.* **68**, 1479–1539 (2005).
- Brück, E. Developments in magnetocaloric refrigeration. *J. Phys. D* **38**, R381–R391 (2005).
- de Oliveira, N. A. Entropy change upon magnetic field and pressure variations. *Appl. Phys. Lett.* **90**, 052501 (2007).
- de Medeiros, L. G., de Oliveira, N. A. & Troper, A. Barocaloric and magnetocaloric effects in $\text{La}(\text{Fe}_{0.89}\text{Si}_{0.11})_{13}$. *J. Appl. Phys.* **103**, 113909 (2008).
- Morellón, L. *et al.* Pressure enhancement of the giant magnetocaloric effect in $\text{Tb}_5\text{Si}_2\text{Ge}_2$. *Phys. Rev. Lett.* **93**, 137201 (2004).
- Lyubina, J., Nenkov, K., Schultz, L. & Gutfleisch, O. Multiple metamagnetic transitions in the magnetic refrigerant $\text{La}(\text{Fe}, \text{Si})_{13}\text{H}_x$. *Phys. Rev. Lett.* **101**, 177203 (2008).
- Planes, A., Mañosa, L. & Acet, M. Magnetocaloric effect and its relation to shape-memory properties in ferromagnetic Heusler alloys. *J. Phys. Condens. Matter* **21**, 233201 (2009).
- Kainuma, R. *et al.* Magnetic-field-induced shape recovery by reverse phase transformation. *Nature* **439**, 957–960 (2006).
- Krenke, T. *et al.* Magnetic superelasticity and inverse magnetocaloric effect in Ni–Mn–In. *Phys. Rev. B* **75**, 104414 (2007).
- Sharma, V. K., Chattopadhyat, M. K., Shaeb, K. H. B., Chouhan, A. & Roy, S. B. Large magnetoresistance in $\text{Ni}_{50}\text{Mn}_{34}\text{In}_{16}$ alloy. *Appl. Phys. Lett.* **89**, 222509 (2006).
- Mañosa, L. *et al.* Effects of hydrostatic pressure on the magnetism and martensitic transition of Ni–Mn–In magnetic superelastic alloys. *Appl. Phys. Lett.* **92**, 012515 (2008).
- Pecharsky, V. K. & Gschneidner, K. A. Jr. in *Magnetism and Structure in Functional Materials* (eds Planes, A., Mañosa, L. & Saxena, A.) 199–222 (Springer Series in Materials Science, 2005).
- Aksoy, S., Acet, M., Deen, P. P., Mañosa, L. & Planes, A. Magnetic correlations in martensitic Ni–Mn-based Heusler shape-memory alloys: Neutron polarization analysis. *Phys. Rev. B* **79**, 212401 (2009).
- Casanova, F. *et al.* Direct observation of the magnetic-field-induced entropy change in $\text{Gd}_5(\text{Si}_x\text{Ge}_{1-x})_4$ giant magnetocaloric alloys. *Appl. Phys. Lett.* **86**, 262504 (2005).
- Mañosa, L., Planes, A. & Moya, X. Comment on ‘The magnetocaloric effect of $\text{LaFe}_{11.6}\text{Si}_{1.4}$, $\text{La}_{0.8}\text{Nd}_{0.2}\text{Fe}_{11.5}\text{Si}_{1.5}$, and $\text{Ni}_{43}\text{Mn}_{46}\text{Sn}_{11}$ compounds in the vicinity of the first-order phase transition’. *Adv. Mater.* **21**, 3725–3726 (2009).
- Planes, A. & Mañosa, L. Vibrational properties of shape memory alloys. *Solid State Phys.* **55**, 159–267 (2001).
- Krenke, T. PhD thesis, Univ. Duisburg-Essen (2007).
- Wurflinger, A. Differential thermal-analysis under high-pressure. 4. Low-temperature DTA of solid–solid and solid–liquid transitions of several hydrocarbons up to 3 kbar. *Ber. Bunsen Gesell. Phys. Chem. Chem. Phys.* **79**, 1195–1201 (1975).
- Marcos, J. *et al.* A high-sensitivity differential scanning calorimeter with magnetic field for magnetostructural transitions. *Rev. Sci. Instr.* **74**, 4768–4771 (2003).
- Tolédano, J. C. & Tolédano, P. *The Landau Theory of Phase Transitions* (World Scientific, 1987).
- Sasioglu, E., Sandratskii, L. M. & Bruno, P. Role of conduction electrons in mediating exchange interactions in Mn-based Heusler alloys. *Phys. Rev. B* **77**, 064417 (2008).
- Buchelnikov, V. D. *et al.* Monte Carlo study of the influence of antiferromagnetic exchange interactions on the phase transitions of ferromagnetic Ni–Mn–X alloys (X = In, Sn, Sb). *Phys. Rev. B* **78**, 184427 (2008).

Acknowledgements

This work was supported by CICYT (Spain), projects MAT2007-62100, and FIS2008-00837 and by Deutsche Forschungsgemeinschaft, grant No. SPP 1239. D.G. acknowledges support from DGIcYT (Spain).

Author contributions

L.M. and A.P. planned the experiments in collaboration with J.T. and M.A. Sample preparation and magnetization measurements were carried out by S.A. and M.A. Calorimetric measurements under pressure were carried out by E.B. and M.B., and under magnetic field, by D.G. All authors discussed the results and analysed the data. The manuscript was prepared by L.M. in collaboration with A.P., J.T. and M.A.

Additional information

The authors declare no competing financial interests. Reprints and permissions information is available online at <http://npg.nature.com/reprintsandpermissions>. Correspondence and requests for materials should be addressed to L.M.

3.7 Paper 4: Inverse barocaloric effect in the giant magnetocaloric La–Fe–Si–Co compound

Resum

L'aplicació d'una pressió hidrostàtica en condicions adiabàtiques provoca un canvi en la temperatura de tota substància. Aquest efecte es conegut com l'efecte barocalòric i la gran majoria de materials s'escalfen quan són comprimits adiabàticament, i es refreden quan la pressió és alliberada (efecte barocalòric convencional). Hi ha, però, materials que presenten un efecte barocalòric invers: es refreden en aplicar una pressió, i s'escalfen quan aquesta és alliberada. Materials amb un efecte barocalòric invers són poc freqüents. Aquí es ressenya un efecte barocalòric invers en el compost intermetàl·lic La–Fe–Co–Si, essent un dels candidats més prometedors per a la refrigeració magnètica, degut al seu efecte magnetocalòric gegant. S'ha trobat que l'aplicació d'una pressió de només 1 kbar provoca un canvi de temperatura d'uns 1,5 K. Aquest valor és més gran que l'efecte magnetocalòric trobat en aquest mateix compost però ara aplicant camps magnètics, això sí, a l'abast d'imants permanents.

ARTICLE

Received 20 Jul 2011 | Accepted 22 Nov 2011 | Published 20 Dec 2011

DOI: 10.1038/ncomms1606

Inverse barocaloric effect in the giant magnetocaloric La-Fe-Si-Co compound

Lluís Mañosa¹, David González-Alonso¹, Antoni Planes¹, Maria Barrio², Josep-Lluís Tamarit², Ivan S. Titov³, Mehmet Acet³, Amitava Bhattacharyya⁴ & Subham Majumdar⁴

Application of hydrostatic pressure under adiabatic conditions causes a change in temperature in any substance. This effect is known as the barocaloric effect and the vast majority of materials heat up when adiabatically squeezed, and they cool down when pressure is released (conventional barocaloric effect). There are, however, materials exhibiting an inverse barocaloric effect: they cool when pressure is applied, and they warm when it is released. Materials exhibiting the inverse barocaloric effect are rather uncommon. Here we report an inverse barocaloric effect in the intermetallic compound La-Fe-Co-Si, which is one of the most promising candidates for magnetic refrigeration through its giant magnetocaloric effect. We have found that application of a pressure of only 1 kbar causes a temperature change of about 1.5 K. This value is larger than the magnetocaloric effect in this compound for magnetic fields that are available with permanent magnets.

¹ Departament d'Estructura i Constituents de la Matèria. Facultat de Física. Universitat de Barcelona. Diagonal 645. Barcelona Knowledge Campus (BKC), 08028 Barcelona, Catalonia, Spain. ² Departament de Física i Enginyeria Nuclear. ETSEIB. Universitat Politècnica de Catalunya. Diagonal 647 and Center for Research in NanoEngineering, Pascual i Vila, 15. Barcelona Knowledge Campus (BKC), 08028 Barcelona, Catalonia, Spain. ³ Experimentalphysik, Universität Duisburg-Essen, D-47048 Duisburg, Germany. ⁴ Department of Solid State Physics. Indian Association for the Cultivation of Science. Jadavpur, Kolkata 700 032, India. Correspondence and requests for materials should be addressed to L.M. (email: lluis@ecm.ub.es).

The need for environmentally friendly cooling technologies has boosted research in solid-state refrigerant materials. In most cases, refrigeration relies on the temperature change caused by the adiabatic application (or removal) of an external field (caloric effects). Under normal circumstances, temperature changes are small, but when the material is close to a phase transition, moderate variations in the external field can provoke temperature changes of several degrees and give rise to so-called giant caloric effects. The tuning parameter for the caloric effect (external field) can be any generalized thermodynamic force, provided that the change in the conjugated generalized thermodynamic displacement is large enough. Hence, giant caloric effects have already been reported for magnetic field (magnetocaloric effect)^{1–3}, electric field (electrocaloric effect)^{4,5}, uniaxial stress (elastocaloric effect)⁶ and hydrostatic pressure (barocaloric effect)^{7,8}.

In a recent work⁷, we postulated that most giant magnetocaloric materials would also exhibit large barocaloric effects. This claim is also supported by recent theoretical studies^{9,10}. Here we report on the barocaloric effect of the giant magnetocaloric material $\text{LaFe}_{11.33}\text{Co}_{0.47}\text{Si}_{1.2}$. $\text{La}(\text{Fe},\text{Si})_{13}$, and the derived quaternary compounds are considered nowadays to be the most promising working materials for magnetic refrigeration technology^{11,12}. They feature relatively large entropy changes with a very low hysteresis and do not contain toxic materials. Materials with reduced hysteresis are highly desirable because irreversibilities associated with such a hysteresis cause a reduction in the refrigerant capacity^{13,14}. $\text{LaFe}_{13-x}\text{Si}_x$ compounds are stable with the cubic NaZn_{13} structure (space group $Fm\bar{3}c$) in a concentration range $1.2 \leq x \leq 2.5$ (ref. 15). Below the Curie temperature T_C in the range 200–260 K, the compound orders ferromagnetically, and above T_C an itinerant-electron metamagnetic transition is induced by an external field¹⁶. Such an itinerant-electron metamagnetic transition originates from a magnetic-field-induced change in the density of states of the 3d electrons at the Fermi level¹⁷. A strong magnetovolume effect originates from the existence of a peak in the electronic density of states, close to the Fermi level, that yields a negative contribution from spin fluctuations to the magnetostriction, resulting in a volume increase on cooling from the paramagnetic to the ferromagnetic state. Two alternative methods have been reported to bring the transition temperature to values close to room temperature without significant modification in the magnetocaloric properties¹¹. One method is to add interstitial hydrogen that expands the crystalline lattice and modifies the exchange interaction between iron atoms. Another method is to replace some Fe atoms by other magnetic transition metals. It has been found that replacing Fe by only a few percent of Co enables a fine tuning of the critical temperature, and it has already been possible to produce industrially meaningful quantities (kilograms) of La–Fe–Co–Si material with good magnetocaloric properties around room temperature¹⁸. The paramagnetic to ferromagnetic transition in La–Fe–Si (and Co-doped) compounds is accompanied by a sizeable volume change of about 1% (ref. 19). There is no change in the crystal symmetry, but the sample isotropically expands as it transforms from the high-temperature paramagnetic to the low-temperature ferromagnetic phase. Such a volume change makes the compound highly sensitive to the application of an external hydrostatic pressure; and indeed the effect of pressure on the magnetic and magnetocaloric properties has been reported^{16,20}. The volume change reported for La–Fe–Si is one of the largest for magnetocaloric materials undergoing magnetostructural transitions. Therefore, this compound is an excellent candidate for exhibiting large barocaloric effects associated with its magnetostructural transition.

We have used calorimetry under hydrostatic pressure to obtain the pressure-induced entropy change, and direct temperature measurements to obtain the adiabatic temperature change. These are the two key parameters characterizing a caloric effect. The results are complemented by the measurement of the magnetic field-induced

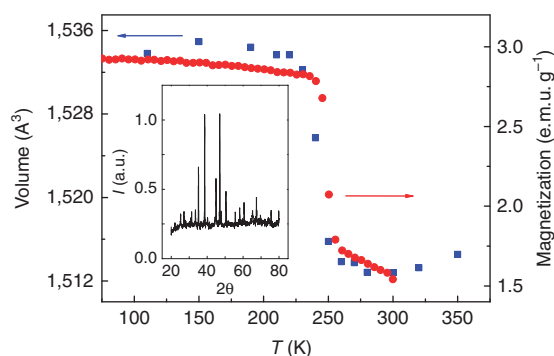


Figure 1 | Temperature dependence of the volume and the magnetization in $\text{LaFe}_{11.33}\text{Co}_{0.47}\text{Si}_{1.2}$. Unit cell volume (squares) and low-field magnetization (circles) as a function of temperature. Inset: room temperature X-ray diffraction pattern. The peak at $\sim 45^\circ$ corresponds to α -iron.

temperature and entropy changes associated with the magnetocaloric effect. The giant barocaloric effect for the material is inverse: that is, we find that the sample warms when pressure is adiabatically released (the entropy decreases under isothermal conditions). The magnetocaloric effect is conventional (the sample warms up when magnetic field is applied and cools down when it is removed).

Results

Structural and magnetic characterization. The sample studied in this investigation is a polycrystalline $\text{LaFe}_{11.33}\text{Co}_{0.47}\text{Si}_{1.2}$ alloy. X-ray diffraction data (inset in Fig. 1) confirm that at room temperature the alloy crystallizes in the NaZn_{13} structure (space group $Fm\bar{3}c$) with a lattice parameter of 11.48 Å. When cooled in the absence of an external field, the sample orders ferromagnetically below a temperature $T_C \sim 250$ K with a concomitant isotropic expansion in the unit cell volume of about 1%, as illustrated in Figure 1. The most widely used method to compute the entropy change associated with a field-induced caloric effect is from isothermal measurements of the generalized displacement vs force curves. Although this method turns out to be very convenient for determining the magnetocaloric effect, where the magnetization can be measured to high precision using superconducting quantum interference device magnetometry, the method is not readily applicable for determining the barocaloric effect because the involved volume changes are small, and they cannot be measured easily with enough precision. An alternative method is to measure directly the heat exchanged when the transition is thermally induced under an external constant field. It requires the use of purpose-built calorimetric devices, and it has been shown to provide reliable results for various caloric effects.

Caloric effects. Examples of calorimetric curves at selected values of hydrostatic pressure are shown in the inset of Figure 2. The curves correspond to heating runs, and have been corrected for the baseline drift. An endothermic feature associated with the ferromagnetic–paramagnetic transition is clearly observed. The transition shifts towards lower temperatures as the pressure is increased. This is consistent with pressure enhancing the stability of the lower volume phase, which is the high-temperature phase. The computed entropy changes (integrated entropy curves) at selected values of the hydrostatic pressure are shown in Figure 2 (details of the computation can be found on Methods section). On heating, the entropy increases by $11.4 \text{ J kg}^{-1} \text{ K}^{-1}$. It must be taken into account that the base-line correction subtracts a background entropy increase, so that the measured increase in entropy is solely due to the occurrence of the phase transition. Numerical subtraction of the integrated entropy curves

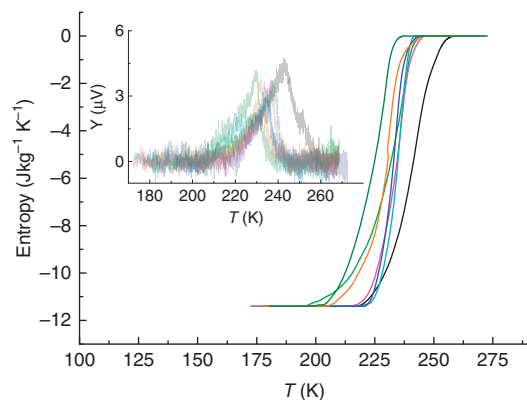


Figure 2 | Entropy as a function of temperature in $\text{LaFe}_{11.33}\text{Co}_{0.47}\text{Si}_{1.2}$. Entropy values, referred to the value at ambient temperature, for selected values of hydrostatic pressure. The inset shows calorimetric curves at selected values of the hydrostatic pressure. Curves appear noisy owing to the weakness of the detected signal, associated with the small mass of the sample. Black lines correspond to 0 kbar; green, 0.8 kbar; magenta, 1 kbar; cyan, 1.2 kbar; blue, 1.4 kbar; orange, 1.7 kbar and olive, 2.1 kbar.

renders the pressure-induced entropy change (barocaloric effect) at each temperature. Results are shown in Figure 3a. The most relevant feature is the positive values of the entropy change, which corresponds to the uncommon inverse barocaloric effect. The magnitude of the barocaloric effect increases with increasing pressures, and a value of $8.6 \text{ J kg}^{-1} \text{ K}^{-1}$ is obtained for $p = 2095$ bar. This value is 75% of the maximum expected value corresponding to the whole transition entropy change. Although the required pressures are larger than typical pressures in domestic fridges (based on compression of a cryogenic gas), they are still readily accessible by conventional hydraulic technologies.

In the studied sample, both magnetocaloric and barocaloric effects originate from the same physical mechanism: the strong magnetovolume interplay occurring at the para-ferromagnetic phase transition that encompasses concomitant changes in magnetization and volume. Therefore, it is interesting to compare the barocaloric with the magnetocaloric properties. To this end, we have measured isothermal magnetization curves at selected values of the temperature from which we have numerically computed the entropy change associated with the magnetocaloric effect. The results are consistent with data reported for alloys with compositions close to the studied sample²¹. The magnetocaloric effect is conventional (that is, decrease in entropy on applying a magnetic field), and the magnetic field-induced entropy change at 5 T ($-9.2 \text{ J kg}^{-1} \text{ K}^{-1}$) amounts to $\sim 80\%$ of the whole transition entropy change.

Although entropy change is a good quantity to characterize caloric effects, any practical application requires knowledge of the adiabatic temperature change. Direct measurements of the adiabatic temperature change when pressure is rapidly released are shown in Figure 3b for pressures of 1 and 2 kbar. The first evident result is the confirmation of the inverse character of the barocaloric effect: the sample warms when pressure is released. The temperature dependence of ΔT is in good agreement with that of ΔS (Fig. 3a). The adiabatic temperature change can be estimated from isothermal entropy data using $\Delta T \simeq -(T/C)\Delta S$, where C is the heat capacity. Although a correct evaluation requires measuring C at different values of p , a rough estimation using C_p data measured at atmospheric pressure (inset in Fig. 4) shows that the measured values of ΔT are lower than the estimated ones. This difference must be mainly ascribed to a lack of perfect adiabatic conditions in the measurements under pressure due to changes in sample surroundings. Therefore, the actual

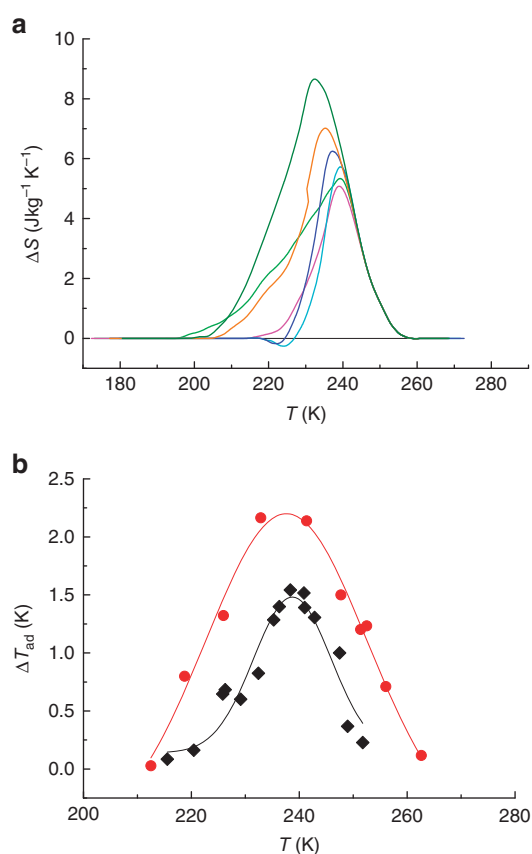


Figure 3 | Barocaloric effects in $\text{LaFe}_{11.33}\text{Co}_{0.47}\text{Si}_{1.2}$. (a) Isothermal entropy change as a function of temperature associated with the isothermal application of selected hydrostatic pressures. Black lines correspond to 0 kbar; green, 0.8 kbar; magenta, 1 kbar; cyan, 1.2 kbar; blue, 1.4 kbar; orange, 1.7 kbar and olive, 2.1 kbar. (b) Adiabatic temperature change on fast release of hydrostatic pressure. Diamonds correspond to 1 kbar and circles to 2 kbar (lines are guides to the eye).

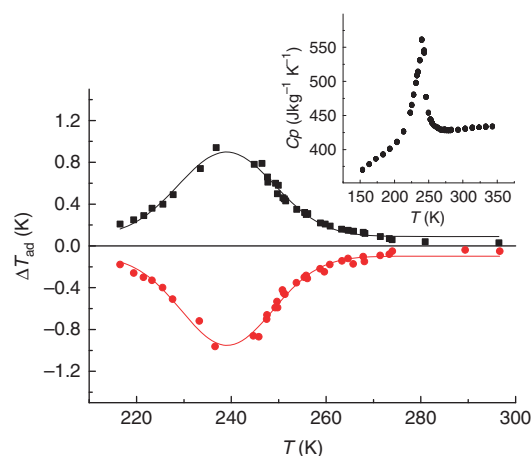


Figure 4 | Magnetocaloric effect in $\text{LaFe}_{11.33}\text{Co}_{0.47}\text{Si}_{1.2}$. Adiabatic temperature measurements on applying (ΔT^{on} , squares) and removing (ΔT^{off} , circles) a 1 T magnetic field. Lines are guides to the eye. The inset shows the temperature dependence of the heat capacity at atmospheric pressure and in the absence of magnetic field.

temperature change is expected to be larger than the data presented in Figure 3b. For comparison we have also directly measured the temperature change associated with the application, ΔT^{on} , and

removal, ΔT^{off} , of a magnetic field of 1 T (Fig. 4). The excellent coincidence of $|\Delta T^{\text{on}}|$ and $|\Delta T^{\text{off}}|$ is an indication of the negligible irreversible losses for this compound. As a consequence of the good adiabatic conditions in magnetic measurements and low hysteretic losses, the values estimated for ΔT agree fairly well with measured ones.

Discussion

In La–Fe–Si (and doped compounds), the total entropy is due to the magnetic contribution from the itinerant $3d$ electrons and a contribution from the lattice (the electronic contribution from the sp conduction electrons is smaller). It has been established that hydrostatic pressure affects both contributions: on the one hand, pressure increases the width of the effective $3d$ bands, thus opposing to the onset of the ordered magnetic state. On the other hand, lattice contribution is also affected by pressure through a strong magnetoelastic coupling that modifies phonon frequencies, which can be expressed in terms of a renormalized Debye temperature⁹.

In systems undergoing a phase transition involving interplay between different material properties (volume and magnetization in the case of present study), caloric effects associated with each of these properties may be of opposite sign. Actually, in the absence of frustration effects, the primary property providing the dominant change in entropy at the transition should be associated with a conventional caloric effect whereas secondary properties may provide conventional or inverse effects depending on specific features of their coupling to the primary property. For instance, on cooling, Ni–Mn–In magnetic shape-memory alloys undergo a structural transition which involves changes of symmetry and volume and is accompanied by a decrease of the magnetization. Therefore, in this material, the barocaloric effect must be conventional. The decrease in magnetization is a consequence of the interplay of magnetism and structure and originates from the antiferromagnetism associated with the change of distances between Mn atoms induced by the structural transition. This feature explains the well-known inverse magnetocaloric effect in these materials²². By contrast, in the La–Fe–Si compounds, the transition is essentially of magnetic nature, and, therefore, the magnetocaloric effect is conventional. Because spin fluctuations induce a volume increase at the transition, the barocaloric effect in this material is inverse.

A good parameter to assess the usefulness of a given material for refrigeration purposes is the relative cooling power (RCP) that quantifies the energy absorbed in a refrigerating cycle. A suitable estimation of RCP is provided by the area below the ΔS vs T curve (see Fig. 3a). The computed values for the magnetocaloric ($45 \text{ J kg}^{-1} \text{ T}^{-1}$) and barocaloric ($90 \text{ J kg}^{-1} \text{ kbar}^{-1}$) effects compare well with data for the best giant magnetocaloric materials. Moreover, although magnetic fields stronger than 1 T are difficult to implement, pressures much larger than those used here can be applied (using clamp cells, for instance), and, therefore, the barocaloric effect appears more advantageous because RCP is expected to substantially increase, as a result of a much broader peak resulting from the shift in the transition temperature.

In summary, we have identified the occurrence of the barocaloric effect in one of the technologically most promising giant magnetocaloric materials. The barocaloric effect has been found to be inverse, and direct temperature measurements prove that the material heats up on removal of hydrostatic pressure. The magnitude of the barocaloric effect for moderate pressures is larger than the magnetocaloric effect for magnetic fields reachable with permanent magnets, and, therefore, the reported effect is potentially useful for eco-friendly solid-state refrigeration purposes. Finally, it is worth mentioning that the inverse barocaloric effect arises from the volume increase on cooling through the phase transition. Such a volume increase gives rise to a negative thermal expansion (NTE) within a certain temperature range. Materials exhibiting colossal NTE resulting

from phase transitions are receiving considerable interest²³. From thermodynamic arguments, it can be expected that these materials with NTE will also exhibit inverse barocaloric effects.

Methods

Thermodynamic background. For any material subjected to hydrostatic pressure (p), magnetic field (H) and temperature (T) changes, the general expression for an entropy change reads

$$dS = \frac{C}{T} dT + \left(\frac{\partial M}{\partial T} \right)_{p,H} dH - \beta v dp \quad (1)$$

where we have used the Maxwell relations:

$$\left(\frac{\partial S}{\partial H} \right)_{p,T} = \left(\frac{\partial M}{\partial T} \right)_{p,H}, \quad \left(\frac{\partial S}{\partial p} \right)_{H,T} = - \left(\frac{\partial v}{\partial T} \right)_{p,H} = -\beta v \quad (2)$$

where β is the thermal expansion.

This expression shows that large entropy changes are expected when either volume or magnetization change drastically with temperature under constant external H and p . This situation typically occurs in the vicinity of phase transitions.

The sign of the entropy change is determined by the temperature derivatives of M and v . At constant pressure, application of a magnetic field will reduce entropy in those systems for which magnetization decreases with increasing temperature. As this is the most commonly found situation, this effect is termed as conventional magnetocaloric effect. By contrast, in those materials where magnetization increases with increasing temperature, application of a magnetic field will increase the entropy, resulting in an inverse magnetocaloric effect. The equivalent reasoning also holds for hydrostatic pressure: materials for which volume increases with increasing temperature give rise to a conventional barocaloric effect (entropy decreases with application of pressure) whereas those with a decreasing volume with increasing temperature show an inverse barocaloric effect.

It is also worth noticing that at constant magnetic field, materials with negative thermal expansion (β) will exhibit inverse barocaloric effect (equation (1)).

Experimental details. Ingots were prepared by arc melting the pure elements under argon atmosphere in the stoichiometric ratio. The composition was determined by energy-dispersive X-ray photoluminescence analysis to correspond to $\text{LaFe}_{11.33}\text{Co}_{0.47}\text{Si}_{1.2}$. The sample was annealed at 1,323 K for 15 days and quenched. Room temperature powder X-ray diffraction patterns were recorded using a Bruker AXS diffractometer (Cu $K\alpha$ radiation, 2θ range from 20° to 80° with a step size of 0.02°). Temperature-dependent high-resolution X-ray powder diffraction measurements were performed on a transmission mode diffractometer using Debye–Scherrer geometry equipped with horizontally mounted INEL cylindrical position sensitive detectors containing 4,096 channels (0.029° 2θ step) and by using monochromatic Cu $K\alpha$ radiation. Temperature was controlled by means of a liquid nitrogen 700 series Oxford Cryosystem Cooler. The heating rate between the measurements was 1.3 K min^{-1} and, before data collection, the sample temperature was stabilized for 15 min.

Magnetization measurements were carried out using a superconducting quantum interference device magnetometer. From these data, the magnetic-field-induced entropy change was numerically computed, taking into account the procedures described in (ref. 24), to avoid undesired overestimated values. Specific heat was measured using a modulated differential scanning calorimeter.

Hydrostatic pressure calorimetry was carried out in a purpose-built calorimeter described in (ref. 7). From calorimetric curves at selected values of the hydrostatic pressure p , the entropy change (referenced to a given state at T_0) is computed as:

$$S(T, p) - S(T_0, p) = \int_{T_0}^T \frac{1}{T} \dot{Q}(p) dT, \quad (3)$$

where $\dot{Q}(p)$ is the heat flux and \dot{T} is the heating/cooling rate.

For direct adiabatic temperature measurements, a chromel–alumel thermocouple was embedded into the sample. In pressure measurements, the sample was placed into the calorimeter and it was first cooled down under applied pressure to a temperature low enough to ensure that the whole sample was in the low-temperature phase. Then, it was heated (keeping the applied pressure) up to the measuring temperature. After thermalization, the pressure was rapidly released and the output of the thermocouple was recorded at a rate of 1 Hz. This procedure was repeated for each measuring temperature. The effect of thermal losses to the surroundings was quantified by performing experiments at temperatures well above and well below the transition. For magnetic measurements, the device described in (ref. 25) was used. The sample was first brought to a temperature high enough to ensure that it was on the high-temperature phase. Then, it was cooled down to the desired temperature, allowed to thermalize, and magnetic field was rapidly applied (at a rate 1 T s^{-1}) while the output of the thermocouple was recorded at a rate 0.5 Hz. After 30 s, the field was removed (at a rate 1 T s^{-1}). This procedure was repeated for each measuring temperature.

References

- Pecharsky, V. K. & Gschneidner, K. A. Jr. Giant Magnetocaloric effect in $\text{Gd}_5\text{Si}_2\text{Ge}_2$. *Phys. Rev. Lett.* **78**, 4494 (1997).
- Tegus, O., Brück, E., Buschow, K. H. J. & de Boer, F. R. Transition-metal-based magnetic refrigerants for room-temperature applications. *Nature* **415**, 150–152 (2002).
- Krenke, T. *et al.* Inverse magnetocaloric effect in ferromagnetic Ni–Mn–Sn alloys. *Nat. Mater.* **4**, 450–454 (2005).
- Mischenko, A. S., Zhang, Q., Scott, J. F., Whatmore, R. W. & Mathur, N. D. Giant electrocaloric effect in thin-film $\text{PbZr}_{0.95}\text{Ti}_{0.05}\text{O}_3$. *Science* **311**, 1270–1271 (2006).
- Neese, B. *et al.* Large electrocaloric effect in ferroelectric polymers near room temperature. *Science* **321**, 821–823 (2008).
- Bonnot, E., Romero, R., Mañosa, L., Vives, E. & Planes, A. Elastocaloric effect associated with the martensitic transition in shape-memory alloys. *Phys. Rev. Lett.* **100**, 125901 (2008).
- Mañosa, L. *et al.* Giant solid-state barocaloric effect in the Ni–Mn–In magnetic shape-memory alloy. *Nat. Mater.* **9**, 478–481 (2010).
- Gorev, M., Bogdanov, E., Flerov, I. & Laptash, N. Thermal expansion, phase diagrams and barocaloric effects in $(\text{NH}_4)_2\text{NbOF}_5$. *J. Phys. Condens. Matter* **22**, 185901 (2010).
- de Medeiros, L. G., Jr., de Oliveira, N. A. & Troper, A. Barocaloric and magnetocaloric effects in $\text{La}(\text{Fe}_{0.89}\text{Si}_{0.11})_{13}$. *J. Appl. Phys.* **103**, 113909 (2008).
- de Oliveira, N. A. & von Ranke, P. J. Theoretical aspects of the magnetocaloric effect. *Phys. Rep.* **489**, 89–159 (2010).
- Shen, B. G., Sun, J. R., Hu, F. X., Zhang, H. W. & Cheng, Z. H. Recent progress in exploring magnetocaloric materials. *Adv. Mater.* **21**, 4545–4564 (2009).
- Gutfleisch, O. *et al.* Magnetic materials and devices for the 21st century: stronger, lighter, and more energy efficient. *Adv. Mater.* **23**, 821–842 (2011).
- Provenzano, V., Shapiro, A. J. & Shull, R. D. Reduction of hysteresis losses in the magnetic refrigerant $\text{Gd}_2\text{Ge}_2\text{Si}_2$. *Nature* **429**, 853–857 (2004).
- Shamberger, P. J. & Ohuchi, F. S. Hysteresis of the martensitic phase transition in magnetocaloric-effect Ni–Mn–Sn alloys. *Phys. Rev. B* **79**, 144407 (2009).
- Palstra, T. T. M., Mydosh, J. A., Nieuwenhuys, G. J., van der Kraan, A. M. & Buschow, K. J. Study of the critical-behaviour of the magnetization and electrical-resistivity in cubic $\text{La}(\text{Fe,Si})_{13}$ compounds. *J. Magn. Magn. Mater.* **36**, 290–296 (1983).
- Fujita, A., Fujieda, S., Hasegawa, Y. & Fukamichi, K. Itinerant-electron metamagnetic transition and large magnetocaloric effects in $\text{La}(\text{Fe}_x\text{Si}_{1-x})_{13}$ compounds and their hydrides. *Phys. Rev. B* **67**, 104416 (2003).
- Fujita, A., Fukamichi, K., Wang, J.-T. & Kawazoe, Y. Large magnetovolume effects and band structure of itinerant-electron metamagnetic $\text{La}(\text{Fe}_x\text{Si}_{1-x})_{13}$ compounds. *Phys. Rev. B* **68**, 104431 (2003).
- Katter, M., Zellmann, V., Reppel, G. W. & Uestuener, K. Magnetocaloric properties of $\text{La}(\text{Fe,Co,Si})_{13}$ bulk material prepared by powder metallurgy. *IEEE Trans. Magn.* **44**, 3044 (2008).
- Fujita, A., Fujieda, S., Fukamichi, K., Mitamura, H. & Goto, T. Itinerant-electron metamagnetic transition and large magnetovolume effects in $\text{La}(\text{Fe}_x\text{Si}_{1-x})_{13}$ compounds. *Phys. Rev. B* **65**, 014410 (2001).
- Lyubina, J., Nenkov, K., Schultz, L. & Gutfleisch, O. Multiple metamagnetic transitions in the magnetic refrigerant $\text{La}(\text{Fe,Si})_{13}\text{H}_x$. *Phys. Rev. Lett.* **101**, 177203 (2008).
- Hu, F. *et al.* Very large magnetic entropy change near room temperature in $\text{LaFe}_{11.2}\text{Co}_{0.7}\text{Si}_{1.1}$. *Appl. Phys. Lett.* **80**, 826–828 (2002).
- Planes, A., Mañosa, L. & Acet, M. Magnetocaloric effect and its relation to shape-memory properties in ferromagnetic Heusler alloys. *J. Phys. Condens. Matter* **21**, 233201 (2009).
- Azuma, M. *et al.* Colossal negative thermal expansion in BiNiO_3 induced by intermetallic charge transfer. *Nat. Commun.* **2**, 347 (2011).
- Caron, L. *et al.* On the determination of the magnetic entropy change in materials with first-order transitions. *J. Magn. Magn. Mat.* **321**, 3559–3566 (2009).
- Moya, X. *et al.* Cooling and heating by adiabatic magnetization in the $\text{Ni}_{50}\text{Mn}_{34}\text{In}_{16}$ magnetic shape-memory alloy. *Phys. Rev. B* **75**, 184412 (2007).

Acknowledgements

This work was supported by CICYT (Spain), projects MAT2010-15114, and FIS2008-00837 (Spain). Critical reading of the manuscript by N.D. Mathur and A. Saxena is acknowledged.

Author contributions

L.M. and A.P. planned the experiments in collaboration with J.T. and M.A. Sample preparation was carried out by A.B. and S.M. X-ray measurements were carried out by J.T., M.B., A.B. and S.M. Measurements in magnetic field were carried out by D.G., I.T. and M.A. Measurements under pressure were carried out by M.B. and J.T. All authors discussed the results and analysed the data. The manuscript was prepared by L.M. in collaboration with A.P., J.T., M.A. and S.M.

Additional information

Competing financial interests: The authors declare no competing financial interests.

Reprints and permission information is available online at <http://npg.nature.com/reprintsandpermissions/>

How to cite this article: Mañosa, L. *et al.* Inverse barocaloric effect in the giant magnetocaloric La–Fe–Si–Co compound. *Nat. Commun.* **2**:595 doi: 10.1038/ncomms1606 (2011).

3.8 Paper 5: Caloric effects induced by magnetic and mechanical fields in a $\text{Ni}_{50}\text{Mn}_{25-x}\text{Ga}_{25}\text{Co}_x$ magnetic shape memory alloy

Resum

Hem estudiat l'efecte elastocalòric en un aliatge tipus Heusler de Ni-Mn-Ga dopat amb Co, que presenta memòria de forma magnètica en les proximitats de la seva transició martensítica. També s'han dut a terme mesures del canvi de longitud en funció de la temperatura com a resultat d'experiments de compressió-esforç i sota camp magnètic aplicat, al llarg de la temperatura de transició de la mostra. A més, els canvis isoterms d'entropia induïts per esforç s'han calculat a partir de les dades experimentals. Els resultats evidencien un efecte elastocalòric significatiu associat amb el gran canvi d'entropia de la transició de fase estructural. L'aliatge també presenta un efecte magnetocalòric per a camps magnètics febles. Es pot veure que l'aplicació d'un camp magnètic per sota d'1T, incrementa la potència relativa de refrigeració estimada per a l'efecte elastocalòric al voltant d'un 20%. Una comparació entre les propietats elastocalòriques i magnetocalòriques del material, indica que sota l'aplicació de 10MPa o 0.8T es pot aconseguir un poder relatiu de refrigeració similar.

Caloric effects induced by magnetic and mechanical fields in a $\text{Ni}_{50}\text{Mn}_{25-x}\text{Ga}_{25}\text{Co}_x$ magnetic shape memory alloy

P. O. Castillo-Villa, D. E. Soto-Parra, J. A. Matutes-Aquino, and R. A. Ochoa-Gamboa
*Centro de Investigación en Materiales Avanzados, S.C. Miguel de Cervantes 120, Complejo Industrial Chihuahua,
 31109 Chihuahua, México*

Antoni Planes, Lluís Mañosa, and David González-Alonso
*Departament d'Estructura i Constituents de la Matèria, Facultat de Física, Universitat de Barcelona, Diagonal 647,
 E-08028 Barcelona, Catalonia, Spain*

Marcelo Stipcich
*IFIMAT, Universidad Nacional del Centro de la Provincia de Buenos Aires, Pinto 399, 7000 Tandil and Consejo Nacional de
 Investigaciones Científicas y Técnicas, A. Rivadavia 1917, Buenos Aires, Argentina*

Ricardo Romero
IFIMAT, Universidad Nacional del Centro de la Provincia de Buenos Aires and CICPBA, Pinto 399, 7000 Tandil, Argentina

D. Ríos-Jara and H. Flores-Zúñiga
Instituto Potosino de Investigación Científica y Tecnológica, Camino a la Presa, 2055 Col. Lomas 4a CP, 78216 San Luis Potosí, México
 (Received 22 December 2010; revised manuscript received 19 February 2011; published 16 May 2011)

We have studied the elastocaloric effect in a Co-doped Ni-Mn-Ga magnetic Heusler shape memory alloy in the vicinity of its martensitic transition. Measurements of the length change as a function of temperature have been carried out across the transition under applied compression stresses and magnetic fields. The isothermal stress-induced entropy changes have been computed from the experimental data. Results evidence a significant elastocaloric effect associated with the large entropy change of the structural phase transition. The alloy also exhibits a magnetocaloric effect at low applied magnetic fields. It is shown that application of a magnetic field below 1 T increases the estimated elastocaloric relative cooling power by about 20%. A comparison of elastocaloric and magnetocaloric properties indicates that a similar relative cooling power is reached under application of 10 MPa or 0.8 T.

DOI: [10.1103/PhysRevB.83.174109](https://doi.org/10.1103/PhysRevB.83.174109)

PACS number(s): 81.30.Kf, 64.60.My, 75.30.Sg

I. INTRODUCTION

Caloric effects originating from the thermal response to changes of external fields such as mechanic, electric, or magnetic fields are inherent to every material.¹ They are typically quantified either by the adiabatic temperature change or by the isothermal entropy change that occurs upon application or removal of an external field.² Materials displaying large caloric effects are recently receiving a great deal of attention since they are promising candidates for environmental-friendly refrigeration techniques.³⁻⁶ At present, the most studied caloric effect is the magnetocaloric effect. After the discovery in the mid-1990s of materials displaying giant magnetocaloric effect in the vicinity of room temperature⁷ a large amount of research has been carried out on this topic.⁸⁻¹¹ In addition, in recent years other caloric effects such as the electrocaloric,¹² elastocaloric,^{13,14} and barocaloric¹⁵ effects have received increasing attention. A key feature common to most materials showing a giant caloric effect is the occurrence of a first-order phase transition. The expected large (discontinuous) change of the order parameter at the transition involves a large entropy content (associated with the latent heat) which is at the origin of the giant caloric effect. In addition, strong coupling between different degrees of freedom such as structural, magnetic, electric, etc. enables the transition to be driven by the different fields conjugated to the corresponding extensive

property, and several caloric effects are expected to occur in an interdependent way.

In the present paper we focus on the influence of a magnetic field on the mechanic-caloric effects in Heusler shape memory alloys. These systems are ferromagnetic materials that undergo a martensitic transition responsible for shape memory properties.¹⁶ They display strong coupling between structural and magnetic properties that enables large deformations to be induced by application of moderate magnetic fields.¹⁷⁻²⁰ Therefore, in the vicinity of the structural transition, large changes of entropy are expected to occur under application of mechanical and magnetic fields. Typically, the mechanical field corresponds to an applied hydrostatic pressure or to a uniaxial stress. In the former case, the caloric effect is called barocaloric, while in the second case it is denoted as the elastocaloric effect. An interesting feature regards the fact that in these magnetic shape memory materials the interplay between structure and magnetism occurs at two well-separated length scales.^{16,21} At the scale of the martensitic variants it is controlled by the increase of magnetocrystalline anisotropy taking place at the transition from the high to the low symmetry phases. At a more microscopic length scale, it is controlled by the corresponding change of the effective magnetic exchange. The first contribution is essentially responsible for the magnetic shape memory effect, while the second makes magnetic

superelasticity feasible (possibility of magnetically inducing the structural transition^{19,20}). Both contributions are expected to give rise to the caloric properties of this kind of materials.

The present work is aimed at studying the elastocaloric properties of a Ni-Mn-Ga-Co Heusler alloy and their relation to its magnetocaloric properties from magnetothermomechanical and calorimetric experiments. Special emphasis has been devoted to the analysis of the influence of the magnetostructural coupling in these caloric properties. The studied alloy has a composition close to the line Ni₅₀Mn_{25-x}Ga₂₅Co_x. In this family the effect of Co substitution is to increase the temperature of the martensitic transition which becomes closer to the Curie point. Interestingly, this substitution keeps the entropy difference between the parent and martensitic phases almost unaffected.²²

The paper is organized as follows. In Sec. II we briefly develop the thermodynamics equations describing caloric effects in systems with magnetostructural coupling. In Sec. III the experimental setup, sample characteristics, and methods are described. The obtained experimental results are presented and briefly discussed in Sec. IV. Finally, in Sec. V the main conclusions are summarized.

II. THERMODYNAMICS

Let a generic thermodynamic closed system be described by temperature, T , and generalized forces, $\{y_i\}_{i=1..n}$, as independent variables. Differential changes of these variables lead to a differential change of entropy that can be written as

$$dS(T, \{y_i\}) = \frac{C}{T}dT + \sum_{i=1}^n \left(\frac{\partial S}{\partial y_i} \right)_{T, \{y_{j \neq i}\}} dy_i, \quad (1)$$

where we have taken into account the definition of the heat capacity $C = T(\partial S/\partial T)_{\{y_i\}}$. On the other hand, from Maxwell's equations we know that

$$\left(\frac{\partial S}{\partial y_i} \right)_{T, \{y_{j \neq i}\}} = \left(\frac{\partial X_i}{\partial T} \right)_{\{y_i\}}, \quad (2)$$

where $\{X_i\}$ are the generalized displacements thermodynamically conjugated of the forces $\{y_i\}$. The caloric effect associated with the property X_i can be quantified as the isothermal entropy change and the adiabatic temperature change associated with a variation of the conjugated field y_i (for instance, from 0 to a given finite value). These changes can be written as

$$\begin{aligned} \Delta S(0 \rightarrow y_i) &= S(T, y_i, \{y_{j \neq i}\}) - S(T, 0, \{y_{j \neq i}\}) \\ &= \int_0^{y_i} \left(\frac{\partial X_i}{\partial T} \right)_{\{y_i\}} dy_i, \end{aligned} \quad (3)$$

and

$$\begin{aligned} \Delta T(0 \rightarrow y_i) &= T(T_{in}, y_i, \{y_{j \neq i}\}) - T(y_i = 0, \{y_{j \neq i}\}) \\ &= - \int_0^{y_i} \frac{T}{C} \left(\frac{\partial X_i}{\partial T} \right)_{\{y_i\}} dy_i, \end{aligned} \quad (4)$$

where T_{in} is the initial temperature of the adiabatic process.

In the present paper, the generalized forces of interest are the magnetic field $\mu_0 H$ (where μ_0 is the magnetic permeability of free space) and the uniaxial stress σ and thus, the

corresponding thermodynamically conjugated displacements are the magnetization M and the strain ε .²³ In this case, let $\delta S(\sigma, H)$ be the difference between the stress-induced entropy change at a constant applied field H and the corresponding change at zero applied magnetic field,

$$\begin{aligned} \delta S(\sigma, H) &= [S(T, \sigma, H) - S(T, 0, H)] \\ &\quad - [S(T, \sigma, 0) - S(T, 0, 0)]. \end{aligned} \quad (5)$$

This equation indicates that the magnetic field-induced entropy change at a given constant applied stress is given by

$$\begin{aligned} S(T, \sigma, H) - S(T, \sigma, 0) &= \delta S(\sigma, H) \\ &\quad + [S(T, 0, H) - S(T, 0, 0)], \end{aligned} \quad (6)$$

where the last term in the above equation is the magnetic field-induced entropy change in the absence of applied stress. Therefore, we obtain that the effect of the magnetostructural coupling is accounted for by $\delta S(\sigma, H)$.

III. EXPERIMENTAL DETAILS

A polycrystalline Ni_{50.5}Mn_{21.7}Ga_{24.7}Co_{3.1} (with an electron to atom ratio $e/a = 7.589$) ingot was obtained by arc melting pure metals under an argon atmosphere. Slices cut from the ingot were encapsulated under vacuum in quartz glass, they were annealed at 1073 K for 72 h, and they were subsequently quenched in iced water. From the annealed slices, specimens were spark machined for length change and calorimetric measurements. The sample for length change measurements was a parallelepiped with length $L_0 = 4.39$ mm and cross section $\phi = 4.05$ mm² ($m \sim 0.14$ g). A small sample of mass 88.6 mg was used for calorimetric measurements.

The studied alloy undergoes a martensitic transition on cooling starting at $M_s = (272 \pm 1)$ K (in the absence of applied mechanical and magnetic fields).

In Fig. 1 we show ac-magnetic susceptibility and calorimetric (inset) data recorded during heating and cooling runs. On cooling, a sharp decrease of susceptibility is observed at the martensitic transition which reflects the increase of

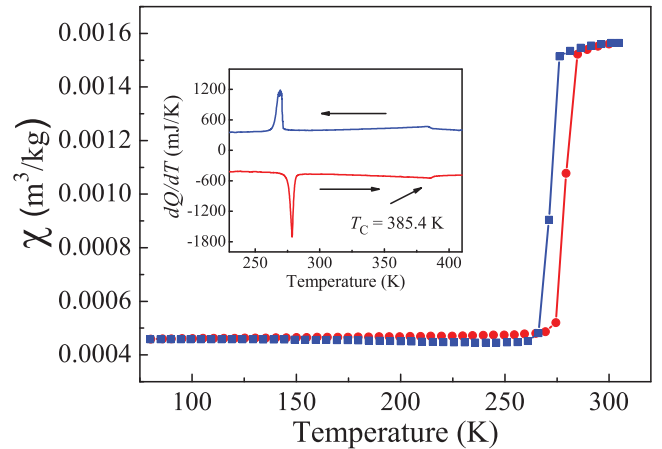


FIG. 1. (Color online) Ac-magnetic susceptibility versus temperature recorded during cooling (solid squares) and heating (solid circles) runs. The inset shows calorimetric curves during cooling and heating.

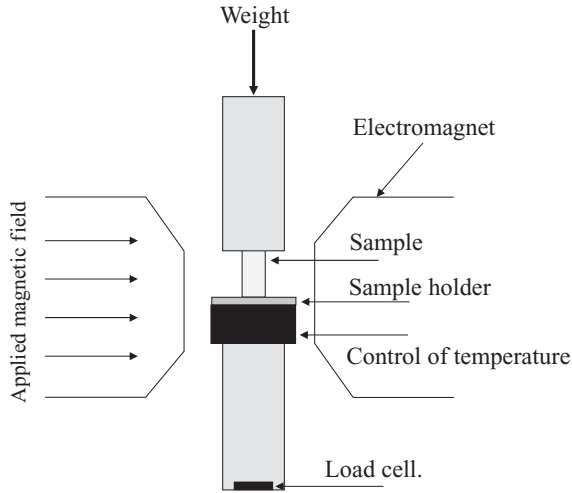


FIG. 2. Schematic representation of the experimental setup, consisting of an electromagnet and temperature-controlled sample holder. The compression stress is applied by means of a weight put on top of the upper rod.

magnetocrystalline anisotropy of the low temperature phase. The transition occurs with a relatively low hysteresis of about 10 K. From the calorimetric data we have computed an entropy change at the martensitic transition (in the absence of externally applied fields) of $\Delta S = (15.8 \pm 0.3)$ J/kg K. The small peak observed on the calorimetric curves at high temperature corresponds to the paramagnetic-ferromagnetic transition at the Curie point, $T_C = 385.4 \pm 0.2$ K.

The experimental setup used to measure length change versus temperature under applied compression stress and magnetic field is schematically shown in Fig. 2. A temperature-controlled sample holder is placed between two cylindrical rods made of a high strength polyamide nylon (nylamid 6/6). The upper rod is in direct contact with the upper surface of the sample. The sample is located between the poles of an electromagnet with a gap of 55 mm that enables the application of magnetic fields up to 1 T. The whole assembly is conveniently kept aligned and uniaxial compressive forces are applied (perpendicular to the magnetic field) by placing weights of controlled mass on the top end of the upper rod. The load was measured by a load cell at the bottom end of the lower rod, which lies on the surface of the bench. A capacitive strain gauge is attached to the upper (mobile) rod to measure length changes. The weight of the rods, sample, and sample holder was taken into account by proper calibration. The transition is thermally induced at given values of the applied magnetic field H and compression force F , which are kept constant during the run.

Stress-induced entropy changes have been computed by taking into account Eq. (3) and for each applied magnetic field, an isothermal stress-induced entropy change has been obtained as

$$\begin{aligned} \Delta S(T, \sigma, H) &= \frac{1}{\rho} \int_0^\sigma \left(\frac{\partial \varepsilon}{\partial T} \right)_\sigma d\sigma \\ &= \frac{1}{m_0} \int_0^F \left(\frac{\partial L}{\partial T} \right)_F dF, \end{aligned} \quad (7)$$

where $m_0 = \rho \Omega_0$ is the mass of the gauge portion of the sample and $\Omega_0 = \phi L_0$, the corresponding volume. The cross section ϕ is assumed constant. $F = \phi \sigma$ is the applied force and σ the applied stress. The strain is given by $\varepsilon = \Delta L / L_0$, with $\Delta L = L - L_0$, where L is the actual gauge length and L_0 the corresponding length in the absence of applied fields. It is worth noting that the polycrystalline nature of the studied sample and the anisotropic deformation of the martensitic variants lead to an inhomogeneous stress distribution inside the sample. For that reason, the suitable thermodynamic variables to evaluate elastocaloric properties are the macroscopic length change and the applied force which conveniently describe any thermodynamic system subjected to a uniaxial force regardless of the microscopic mechanism responsible for the change in length.

Length change measurements were complemented with calorimetric measurements under an applied magnetic field that enables estimation of magnetic field-induced isothermal changes of entropy. To this end, we have used a specially designed differential scanning calorimeter that enables application of magnetic fields up to 1 T, while temperature is swept at rates of ~ 0.5 K/min.²⁴ From the calorimetric curves the variation of entropy along the transition referred to the entropy of the low-temperature phase is obtained as $S(T, H) = \int_{T_i}^T \frac{1}{T} \frac{dq}{dT} dT$, where dq/dT is the heat released (or absorbed) per unit temperature and T is a temperature in the range over which the transition extends. T_i is either the starting transition temperature on heating or the finishing transition temperature on cooling.

IV. RESULTS AND DISCUSSION

Figure 3 illustrates a typical example of a measured length as a function of temperature for a magnetic field of 0.36 T, and selected applied stresses up to ~ 10 MPa.²⁵ For temperatures above and below the transition region, the length linearly increases with temperature. The shrinkage associated with

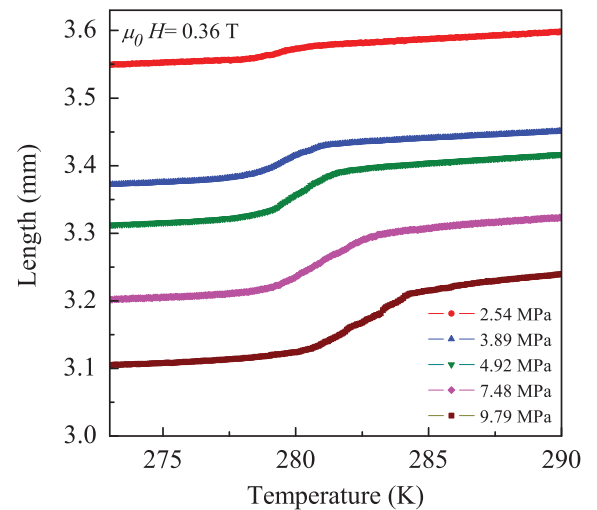


FIG. 3. (Color online) Example of curves giving the measured length vs temperature obtained during heating runs at the indicated values of the applied compression stress and for an applied magnetic field of 0.36 T. See Ref. 25.

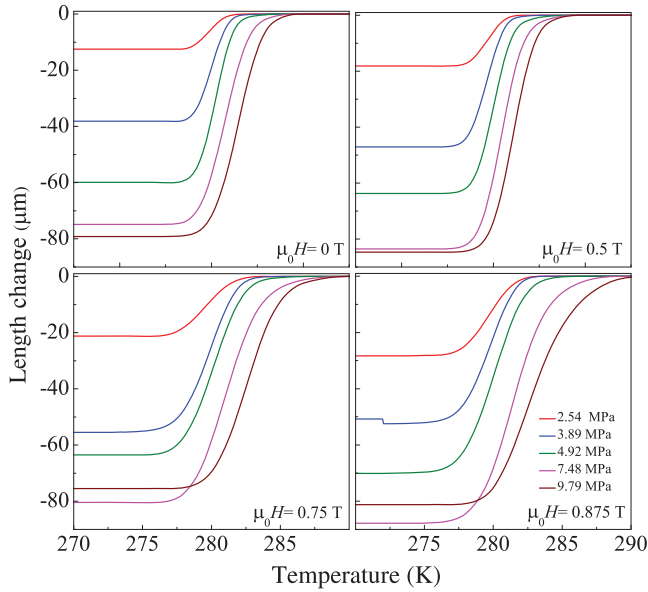


FIG. 4. (Color online) Length change vs temperature curves after correction from the temperature dependence away from the transition region. For convenience, the origin has been taken in the high-temperature parent phase.

the martensitic transition can be obtained by suppression of the temperature change outside the transition region. Results at different magnetic fields and selected applied stresses are shown in Fig. 4. A first evident effect of increasing the compression stress is to increase the stability of the martensitic phase thereby shifting the transition to higher temperatures. On the other hand, the total shrinkage associated with the transition also increases with increasing applied stress. This result reflects the tendency of the stress to break the degeneracy associated with the symmetry-allowed martensitic variants which are equivalent in the absence of applied external magnetic and mechanical fields. Hence, within each grain, the increase of applied stress gives rise to a gradual increase in the fraction of martensitic variants which are crystallographically oriented in a direction energetically favorable to the direction of the applied uniaxial stress.

From the data shown in Fig. 4 we computed the isothermal stress-induced entropy changes as a function of temperature and stress using Eq. (7). Results are shown in Fig. 5 for the selected applied fields. There is a decrease in entropy (negative values for the stress-induced entropy changes) under the application of compressive stress. Such an entropy decrease would result in a temperature increase of the sample [see Eqs. (3) and (4)] for an adiabatically applied stress. This is the most commonly found situation for the several caloric effects for which cooling is achieved upon removing the external field. In this sense the elastocaloric effect found here is conventional. It is worth noting that conventional caloric effects will be found in the cases when the transition temperature increases with external field. Conversely, a decrease in the transition temperature with external field yields to the so-called inverse caloric effect for which the sample cools down under adiabatically applying an external field.

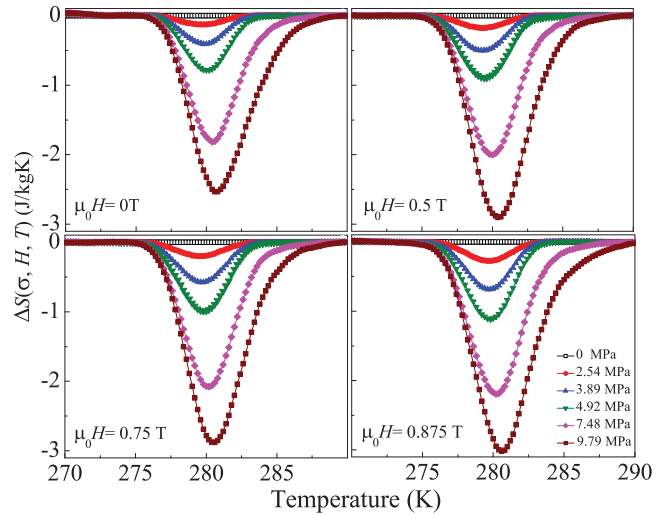


FIG. 5. (Color online) Stress-induced entropy changes at different values of the stress and selected values of the applied magnetic field. Data correspond to heating runs.

The effect of magnetic field on the elastocaloric effect is illustrated in Fig. 5. The magnetic field enhances the elastocaloric effect: The absolute value of the entropy change for a given stress increases with increasing magnetic field. For the ranges of stresses and magnetic fields investigated, the entropy changes associated with the elastocaloric effect are significantly lower than the whole available entropy content (the transition entropy change) of about 15 J/kg K. Such a low value is a consequence of the fact that the transition is spread over a relatively broad range of temperatures (see Fig. 4) and therefore relatively large fields (stress and magnetic) are required to induce the whole transition. These kinds of large stresses cannot be applied to magnetic Heusler shape memory alloys owing to their brittleness. In contrast, for nonmagnetic ductile shape memory alloys it has been shown that larger stresses induce the transformation of the whole sample and the entropy change associated with the elastocaloric effect coincides with the transition entropy change.¹³

A meaningful parameter for practical applications of caloric effects is the relative cooling power (RCP).³ For the elastocaloric effect it can be estimated as

$$RCP = \int_{\Delta T} \Delta S(\sigma, H, T) dT, \quad (8)$$

where the range over which the integral is performed, ΔT , corresponds to the extension of the peaks giving the stress-induced entropy changes shown in Fig. 5. In Fig. 6 we plot the obtained RCP as a function of the applied stress for selected values of the applied magnetic fields. Again, the effect of magnetic field is to enhance the elastocaloric effect by increasing the RCP . It is remarkable that after a moderate increase at very low stresses, the RCP increases very steeply with applied stress. Such an increase is due to two contributions. On the one hand, by increasing stress a larger amount of the sample transforms isothermally to martensite thus giving rise to larger stress-induced entropy changes. For large enough stresses this contribution is expected to saturate when the whole sample transforms to martensite. On the other

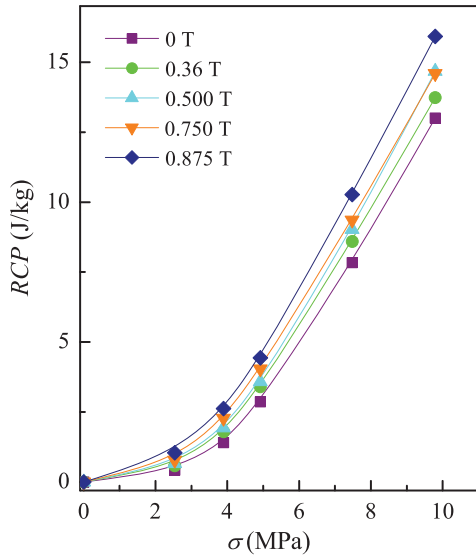


FIG. 6. (Color online) Relative cooling power as a function of the applied compression stress for selected values of the applied magnetic field. Continuous lines are a guide to the eye.

hand, the integration range ΔT in Eq. (8) also increases with stress mainly due to the shift in the transition temperature with stress.

At this stage it is interesting to compare the obtained results for the elastocaloric properties of the studied Ni-Mn-Ga-Co system with its magnetocaloric properties. For such a purpose, we estimated magnetic field-induced isothermal changes of entropy at zero-applied stress from differential temperature-scanning calorimetric measurements performed at applied selected magnetic fields up to 1 T. It is worth noticing that DSC calorimetry under a magnetic field has been successfully used to determine entropy changes associated with first-order magnetostructural phase transitions.^{24,26–28} Figure 7 shows the obtained magnetic field-induced entropy changes (magnetocaloric effect) as a function of temperature, for selected values of the magnetic field. These data are obtained by subtraction of the transition entropy vs temperature curves at constant field, shown on the inset. The magnetocaloric effect for Ni-Mn-Ga-Co samples with composition close to the one studied here have been reported from magnetization data in Ref. 29. At low fields a small positive entropy change of about 1.2 J/kg K for 1 T was reported. This value decreased for larger magnetic fields and was attributed to be due to the larger magnetocrystalline anisotropy of the martensite. The magnetocaloric effect for the investigated sample is significantly larger (~ 6 J/kg K for about 1 T) and conventional: negative entropy values over all range of studied magnetic fields. This is consistent with the increase in transition temperature with magnetic field (see inset of Fig. 7). It is worth noticing that the situation is similar to that found for the elastocaloric effect: the range of studied magnetic fields is not large enough to fully induce the transformation of the whole sample and consequently the values found for the magnetic field-induced entropy change are lower than the transition entropy change. The magnetocaloric effect for the largest available magnetic field (~ 1 T) is larger than the

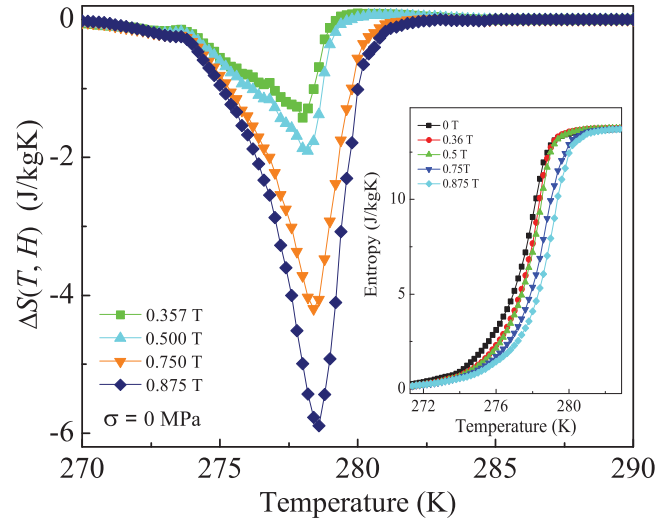


FIG. 7. (Color online) Magnetic field-induced isothermal entropy change as a function of temperature for selected applied magnetic fields and zero compression stress. The inset shows the entropy curves obtained from the calorimetric measurements during heating at the corresponding applied magnetic fields.

elastocaloric at ~ 10 MPa, but is still only a fraction of the overall entropy change. The larger value of the magnetocaloric effect is simply a consequence of the fact that the transition occurs in a narrower range of temperatures in the sample used for calorimetric measurements (the range is approximately half of the range obtained in length change measurements). Therefore, the estimated RCP is rather comparable in both cases. Actually, the same RCP is obtained at $\sigma = 10$ MPa and $H = 0$, and for an applied field of 0.8 T and zero stress.

V. SUMMARY AND CONCLUSIONS

We have reported on the elastocaloric effect in magnetic shape memory alloys. We have also investigated the influence of applied magnetic fields on this effect, and a comparative study with the magnetocaloric effect exhibited by the alloy was performed. Both the elastocaloric and magnetocaloric effects are a consequence of the martensitic transition undergone by the alloy. The effect of a compressive stress and of a magnetic field is to increase the stability of the martensitic phase, thereby leading to an increase of the transition temperature with stress and magnetic field. Consistent with this finding, both elastocaloric and magnetocaloric effects are conventional (i.e., isothermal application of an external field causes a reduction in the entropy of the sample).

The entropy values associated with the elastocaloric effect for relatively low applied stresses (about 10 MPa) are only a fraction of the whole available entropy content owing to the fact that the investigated range of stresses is not large enough to induce the transformation of the whole sample. Actually the brittleness of magnetic shape memory alloys is one of the major drawbacks for the practical application of the magnetic shape memory effect, and efforts are devoted to finding materials with improved mechanical performances. An increase in the

range of applied stresses will result in an enhancement of the elastocaloric effect in magnetic shape memory materials.

The effect of magnetic field is to enhance the elastocaloric effect, particularly for the cooling capacity associated with this effect. It has been found that the cooling capacity increases steeply with applied stress, and therefore this quantity is expected to be significantly increased in the event of finding

magnetic shape memory materials with improved mechanical properties.

ACKNOWLEDGMENTS

This work was supported by CICYT (Spain) under Project No. MAT2010-15114.

-
- ¹J. F. Nye, *Physical Properties of Crystals* (Oxford University Press, New York, 1957).
- ²A. M. Tishin and Y. I. Spichkin, *The Magnetocaloric Effect and Its Applications* (Institute of Physics, Bristol and Philadelphia, 2003).
- ³K. A. Gschneidner, V. K. Pecharsky, and A. O. Tsokol, *Rep. Prog. Phys.* **68**, 1479 (2005).
- ⁴E. Brück, in *Handbook of Magnetic Materials*, Vol. 17, edited by K. H. J. Buschow (Elsevier, Amsterdam, 2007), p. 235.
- ⁵S. G. Lu and Q. M. Zhang, *Adv. Mater.* **21**, 1983 (2009).
- ⁶N. A. de Oliveira and P. J. von Ranke, *Phys. Rep.* **489**, 89 (2010).
- ⁷V. K. Pecharsky and K. A. Gschneidner, *Phys. Rev. Lett.* **78**, 4494 (1997).
- ⁸O. Tegus, E. Brück, K. H. J. Buschow, and F. R. de Boer, *Nature (London)* **415**, 150 (2002).
- ⁹V. Provenzano, A. J. Shapiro, and R. D. Schull, *Nature (London)* **429**, 853 (2004).
- ¹⁰T. Krenke, E. Duman, M. Acet, E. F. Wassermann, X. Moya, L. Mañosa, and A. Planes, *Nature Mater.* **4**, 450 (2005).
- ¹¹S. B. Shen, J. R. Sun, F. X. Hu, H. W. Zhang, and Z. H. Chen, *Adv. Mater.* **21**, 4545 (2009).
- ¹²A. S. Mischenko, Q. Zhang, J. F. Scott, R. W. Whatmore, and N. D. Mathur, *Science* **311**, 1270 (2006).
- ¹³E. Bonnot, R. Romero, L. Mañosa, E. Vives, and A. Planes, *Phys. Rev. Lett.* **100**, 125901 (2008).
- ¹⁴D. E. Soto-Parra, E. Vives, D. González-Alonso, L. Mañosa, A. Planes, R. Romero, J. A. Matutes-Aquino, R. A. Ochoa-Gamboa, and H. Flores-Zúñiga, *Appl. Phys. Lett.* **96**, 071912 (2010).
- ¹⁵L. Mañosa, D. González-Alonso, A. Planes, E. Bonnot, M. Barrio, J.-L. Tamarit, S. Aksoy, and M. Acet, *Nature Mater.* **9**, 478 (2010).
- ¹⁶A. Planes, L. Mañosa, and M. Acet, *J. Phys. Condens. Matter* **21**, 233201 (2009).
- ¹⁷K. Ullakko, J. K. Huang, C. Kantner, R. C. O'Handley, and V. V. Kokorin, *Appl. Phys. Lett.* **69**, 1966 (1996).
- ¹⁸A. Sozinov, A. A. Likhacher, N. Lanska, and K. Ullakko, *Appl. Phys. Lett.* **80**, 1746 (2002).
- ¹⁹R. Kainuma, Y. Imano, W. Ito, Y. Sutou, H. Morito, S. Okamoto, S. Kitakami, O. Oikawa, A. Fujita, T. Kanomata, and K. Ishida, *Nature (Londnon)* **439**, 957 (2006).
- ²⁰T. Krenke, E. Duman, M. Acet, E. F. Wassermann, X. Moya, L. Mañosa, A. Planes, E. Suard, and B. Ouladdiaff, *Phys. Rev. B* **75**, 104414 (2007).
- ²¹J. Marcos, L. Mañosa, A. Planes, F. Casanova, X. Batlle, and A. Labarta, *Phys. Rev. B* **68**, 094401 (2003).
- ²²D. E. Soto-Parra, X. Moya, L. Mañosa, H. Flores-Zúñiga, F. Alvarado Hernández, R. A. Ochoa-Gamboa, J. A. Matutes-Aquino, and D. Ríos-Jara, *Philos. Mag.* **90**, 2771 (2010).
- ²³Notice that H and σ should have vectorial and tensorial (rank 2) character, respectively. However, we will assume them as scalars and thus the generalized displacements M and ε will be the components corresponding to these fields.
- ²⁴The calorimeter used in the present study is a simplified version, adequate for near-room-temperature measurements, of the calorimeter described in J. Marcos, F. Casanova, X. Batlle, A. Labarta, A. Planes, and L. Mañosa, *Rev. Sci. Instrum.* **74**, 4768 (2003).
- ²⁵Since the length is obtained from the displacement of the upper rod, it is measured with respect to an arbitrary origin. Its variation with temperature takes into account the length change of the specimen due to the transition.
- ²⁶T. Plackowski, Y. Wang, and A. Junod, *Rev. Sci. Instrum.* **73**, 2755 (2002).
- ²⁷S. Jeppesen, S. Linderoth, N. Pryds, L. Theil Kuhn, and J. Buch Jensen, *Rev. Sci. Instrum.* **79**, 083901 (2008).
- ²⁸V. Basso, C. Sasso, and M. Küpferling, *Rev. Sci. Instrum.* **81**, 113904 (2010).
- ²⁹A. M. Gomes, M. Khan, S. Stadler, N. Ali, I. Dubenko, A. Y. Takeuchi, and A. P. Guimarães, *J. Appl. Phys.* **99**, 08Q106 (2006).

CHAPTER 4

RESUM DELS RESULTATS I CONCLUSIONS

EN aquesta tesi es presenta una col·lecció de cinc articles publicats en revistes científiques revisades per parells, tots ells reunits per tal d'acabar en que consisteix l'acoblament magneto-estructural que presenten una gran varietat de materials magnètics. En particular, en aquesta tesi s'han estudiat amb més detall aquells materials magnètics que com a resposta a un estímul extern demostren l'acoblament magneto-estructural a través d'efectes calòrics. Amb aquesta finalitat, s'han estudiat diferents aliatges Heusler, com ara el Ni-Mn-In, el Ni-Mn-Ga dopat amb Fe i Co; com també s'ha estudiat un aliatge de la família La-Fe-Si, però dopat amb Co. En el primer cas, els aliatges Heusler a més d'un efecte de memòria de forma també presenten un efecte calòric, on tots dos efectes són conseqüència de l'acoblament magneto-estructural en aquest tipus d'aliatges.

Per a la família d'aliatges La-Fe-Si, en canvi, és l'acoblament magneto-elàstic el responsable dels efectes calòrics que exhibeixen.

En el primer article [87] s'estudia la dinàmica de xarxa en dos monocristalls su-

perelàstics de Ni-Mn-In i de composició similar. En aquest article, estudiem les constants elàstiques i les corbes de dispersió dels fonons per mitjà de tècniques d'ultrasons i de dispersió de neutrons, respectivament. Les mesures de les constants elàstiques es van dur a terme a la Universitat de Barcelona; però en canvi, les mesures de dispersió de neutrons es van dur a terme al High Flux Reactor d'Isòtops del Laboratori Nacional d'Oak Ridge, Tennessee, USA. Si bé les diferències en la composició entre tots dos monocristalls modifica la transformació estructural, el punt de Curie es manté gairebé constant. Malgrat les diferències en la composició, els valors de les constants elàstiques en tots dos mètodes, d'ultrasons i de dispersió de neutrons, estan d'acord. A més, aquests resultats són consistents en comparació amb càlculs *ab initio* per l'aliatge Heusler estequiomètric Ni₂MnIn. Hem observat efectes premartensítics com ara una disminució de l'energia en la branca transversal TA₂ [ξξ0], a prop de ξ ≈ 0,33. L'energia d'aquestes fonons disminueix a mesura que les temperatures arriben a la transformació martensítica. En la transformació directa-*refredant*- aquesta anomalia s'accentua, però, fins i tot, per a temperatures properes a la transició martensítica la caiguda és menys pronunciada que en l'aliatge amb memòria de forma magnètica prototípic de Ni-Mn-Ga. Aquest fenomen es basa en l'estovament del fonó anòmal, cosa que reflecteix la inestabilitat dinàmica de la xarxa cúbica contra distorsions dels plans {110} al llarg de la direcció ⟨11̄0⟩. També hem observat com la constant elàstica de cisalla C' disminueix a mesura que la temperatura s'aproxima a la transició martensítica. A més, la disminució monòtona en la constant elàstica C' juntament amb la disminució monòtona del fonó anòmal, són indicatius de l'absència d'una fase premartensítica en aquest aliatge. Finalment, encara que no s'ha mesurat cap dependència en les energies dels fonons per a camps magnètics de fins a 4 T, l'acoblament magneto-elàstic es revela en el límit de longitud d'ona llarga a través de la dependència de les constants elàstiques per a camps

magnètics baixos.

En els següents dos articles hem treballat amb dos aliatges policristal·lins, basats en l'aliatge NiMnGa, per estudiar els seus diversos efectes calòrics. A l'article [12], vàrem dopar l'aliatge de Ni-Mn-Ga amb Fe per reduir no només la fragilitat de la mostra, i per tant, poder realitzar les mesures de tensió, sinó també per augmentar la temperatura de la transformació martensítica. Les mesures de calorimetria es van realitzar en els límits de tensió i de camp magnètic aplicat baix. S'ha de mencionar que les mesures de tensió es van realitzar en un dispositiu especialment dissenyat per poder controlar la força aplicada. Dins d'aquests límits, els canvis d'entropia induïts sota esforç i camp magnètic són convencional i invers, respectivament. Aquests comportaments són consistents amb el fet que la transformació martensítica es desplaça a una temperatura més alta per l'aplicació d'una tensió, mentre que la transformació martensítica disminueix a mesura que el camp aplicat augmenta. No obstant això, és ben sabut que en aquests sistemes i per a camps prou grans, l'efecte magnetocalòric invers esdevé convencional. Sistemes amb martensites modulades dels tipus 10M i 14M, com en el present cas, són magnèticament gairebé isotròpiques a la fase cúbica d'alta temperatura -austenita-, però en canvi, tenen una gran anisotropia uniaxial en la fase martensítica. Per a camps aplicats baixos, quan l'aliatge transforma a martensita, sorgeix l'MCE invers com a conseqüència de la reducció de la magnetització al punt de transició. Per tant, per a camps prou alts, la fase austenita ordena els seus moments magnètics. Com a resultat, l'MCE esdevé convencional. De fet, per a una composició similar ja es va informar d'un canvi de temperatura positiu per a camps magnètics de $\mu_0 H \geq 1.5$ T. En resum, podem dir que per a camps aplicats baixos i amb una composició pròxima a l'estequiomètrica, l'MCE invers dels aliatges de Ni-Mn-Ga es fruit d'un acoblament magneto-estructural a escala mesoscòpica entre els dominis magnètics i les variants martensítiques.

A l'article [15] hem estudiat un aliatge policristal·lí de Ni-Mn-Ga dopat amb Co per tal d'augmentar el punt de transició a través de l'addició de Co. Tant l'efecte elastocalòric (ECE) com l'efecte magnetocalòric (MCE) són fruit de la transició martensítica que pateix l'aliatge. A diferència del primer cas [12], en aquest darrer cas l'aliatge dopat amb Co presenta un MCE i un ECE convencionals, és a dir, la temperatura de transició augmenta amb el camp magnètic i amb l'esforç aplicat, respectivament. Per tant, tots dos camps estableixen la fase martensítica. A més, els valors d'entropia associats amb l'efecte elastocalòric per a tensions relativament baixes (aproximadament 10 MPa) és només una fracció de tot el contingut de l'entropia disponible, a causa del fet que l'interval de tensions estudiat no és prou gran com per induir totalment la transformació. La fragilitat dels aliatges amb memòria de forma magnètics és un dels principals inconvenients per a l'aplicació pràctica de l'efecte de memòria de forma magnètic. Així els esforços es dediquen a la recerca de nous materials amb millors prestacions mecàniques. Finalment, s'ha observat que l'aplicació d'un camp magnètic per sota d'1 T augmenta la potència relativa de refredament elastocalòric estimat al voltant d'un 20%. Una comparació de les propietats elastocalòriques i magnetocalòriques indica que una potència de refredament relatiu similar s'aconseguiria a l'aplicar 10 MPa o 0,8 T.

En els dos últims treballs [13, 14] hem utilitzat un calorímetre expressament fabricat per treballar sota pressions hidrostàtiques de fins a 3 kbar, a fi d'observar els efectes de la pressió en la resposta tèrmica de la mostra. L'aplicació d'una pressió hidrostàtica en condicions adiabàtiques provoca un canvi en la temperatura de qualsevol substància, aquest efecte es coneix com a efecte barocalòric (BCE). Hem estat els primers en informar sobre mesures calorimètriques directes en un aliatge amb memòria de forma sotmès a una pressió hidrostàtica [13]. A més, hem observat que l'aplicació d'una pressió hidrostàtica moderada en un aliatge amb memòria de forma

magnètica dóna lloc a un BCE comparable a l'efecte MCE gegant típic d'aquest tipus de materials, és a dir, un BCE de $24,4 \text{ J/kg}\cdot\text{K}$ sota una pressió hidrostàtica de 2.6 kbar. En el Ni-Mn-In [13], cal assenyalar que l'aplicació d'una pressió en condicions isoterms dóna com a resultat una disminució en l'entropia, és a dir, un BCE convencional; mentre que l'aplicació d'un camp magnètic en condicions isoterms resulta en un augment de l'entropia, és a dir, un MCE invers. Aquest resultat és consistent amb el fet que la pressió estabilitza la fase martensítica, mentre que el camp magnètic estabilitza la fase cúbica. Per a l'BCE convencional, en la transformació directa –refredant– l'aliatge pateix un canvi de volum negatiu com a conseqüència del menor volum de la fase martensita en comparació amb l'austenita. Per contra, l'MCE invers és el resultat de la disminució de la magnetització en la transformació directe, cosa que reflecteix l'acoblament magneto-estructural.

D'altra banda, l'aliatge de La-Fe-Si [14], que va ser dopat amb Co per tal d'augmentar el seu punt de transició sense canviar els seus efectes tèrmics, exhibeix un BCE invers i un MCE convencional. A diferència de l'acoblament magneto-estructural per el cas de l'aliatge Ni-Mn-In, l'aliatge de La-Fe-Co-Si pateix un acoblament magneto-elàstic, és a dir, no canvia d'estructura cristal·lina a banda i banda de la transició. En refredar, l'BCE invers, que exhibeix l'aliatge de LaFeCoSi, és el resultat de l'expansió de la cel·la unitat a través de la transició, és a dir, un increment de volum. Però l'MCE convencional és causat pel fet que en refredar, la magnetització en la fase de baixa temperatura és més important que la magnetització en la fase d'alta temperatura, cosa que reflecteix l'acoblament magneto-elàstic que pateix. També hem fet mesures directes del canvi de temperatura en condicions adiabàtiques, presentant un bon acord entre les mesures calorimètriques directes i les mesures directes de canvi de temperatura. Finalment, val la pena assenyalar que l'BCE per a pressions moderades –amb un valor de $8,6 \text{ J/kg}\cdot\text{K}$ per a una pressió

aproximada de 2 kbar– és més gran que l'MCE per a camps magnètics assolibles amb imants permanents.

En resum, podriem dir que tots els materials magnètics estudiats dins d'aquesta tesi són potencialment útils per a la refrigeració ecològica d'estat sòlid.

CHAPTER 5

SUMMARY AND CONCLUSIONS

IN this thesis we present a collection of five papers published in peer-reviewed scientific journals, all of them gathered in order to shed light on the magneto-structural coupling that is present in a variety of magnetic materials. In particular, within this thesis we have studied in more detail those magnetic materials that show magneto-structural coupling through thermal effects in response to an external stimulus, i.e., Caloric Effects. For this purpose, herein, a variety of alloys has been studied ranging from the Heusler alloys such as Ni–Mn–In, the Fe-doped Ni–Mn–Ga and the Co-doped Ni–Mn–Ga, to the Co-doped La–Fe–Si family of alloys. In the former case, Heusler alloys exhibit a shape memory effect as well as a caloric effect, both being a consequence of a magneto-structural coupling, which lies beneath its Caloric Effects. But in the latter case, the magneto-elastic coupling is responsible for the caloric effects that exhibit the La–Fe–Si family of alloys.

The first paper [87] deals with the lattice dynamics in two magnetic superelastic Ni–Mn–In single-crystals of similar composition. There, we report both elastic

constants and phonon-dispersion curves measurements through ultrasonic and neutron scattering methods, respectively. The elastic constants measurements were performed at the University of Barcelona, and the neutron scattering measurements were carried out at the High Flux Isotope Reactor of the Oak Ridge National Laboratory, Tennessee, U.S.A. The differences in the composition between both single-crystals modifies the structural transformation, while the Curie-point remains almost the same. Despite the differences in composition, the values for the elastic constants from both ultrasonic and neutron scattering methods are in good agreement. In addition, these results are consistent compared to *ab initio* calculations for the stoichiometric Ni₂MnIn Heusler alloy. We have observed premartensitic effects such as a lowering in the energy in the transverse TA₂ [$\xi\xi 0$] branch close to $\xi \approx 0.33$. The energy of these phonons decreases as the temperatures attains to the martensitic transformation. In the forward transformation –upon cooling– this anomaly is enhanced, but even at temperatures close to the martensitic transition the dip is less pronounced than in the prototypical magnetic shape memory alloy Ni–Mn–Ga. This phenomenon relies on the *softening* of the anomalous phonon, thus reflecting the dynamical instability of the cubic lattice against distortions of {110} planes along $\langle 1\bar{1}0 \rangle$ directions. We have also observed that the shear elastic constant C' also decreases as temperature approaches the martensitic transition. In addition, the monotonous decrease in the elastic constant C' together with the monotonous decrease in the anomalous phonon indicates the absence of a premartensitic phase in this alloy system. Finally, although no magnetic-field dependence of phonon energies has been measured for fields up to 4 T, the magneto-elastic coupling is revealed at the long-wavelength limit through the elastic constants dependence on a magnetic field which saturates at low magnetic fields.

In the next two papers we have considered two NiMnGa–based polycrystalline

alloys for studying their diverse caloric effects. In the paper [12] we doped the Ni–Mn–Ga alloy with Fe not only to reduce the fragility of the sample and be consequently able to perform the stress measurements, but also to increase the martensitic transformation. The temperature measurements were carried out in the limits of low applied stress and magnetic field. It should be noticed that the stress measurements were performed in a purpose-built device which enabled control of the applied force. The stress- and magnetic field-induced entropy changes obtained in these limits are conventional and inverse, respectively. These are the expected behaviors consistent with the fact that the martensitic transformation is shifted to a higher temperature by the application of a stress, while the martensitic transformation decreases as the applied field rises. Nevertheless, it is well known that in these systems for high enough fields the inverse magnetocaloric effect becomes conventional. Systems showing 10M and 14M modulated martensites, as in the present case, are almost magnetically isotropic in the high temperature cubic –austenite– phase, in contrast to the large uniaxial anisotropy in the martensitic phase. But when the alloy undergoes the martensitic transition at low applied fields the inverse MCE arises in consequence of the reduction in the magnetization associated with such a large magnetic anisotropy through the transition point. Thus, for high enough fields in the austenite phase the magnetic moments become ordered. As a result, the MCE becomes conventional. For a similar composition indeed it was already reported a positive temperature change for fields $\mu_0 H \geq 1.5$ T. In summary, for a nearly stoichiometric Ni–Mn–Ga composition, the inverse MCE for low applied fields is consequence of a mesoscopic magneto-structural coupling between magnetic domains and martensitic variants.

In the paper [15] we have studied a Co-doped Ni–Mn–Ga polycrystalline alloy to increase the transition point through adding Co. Both the elastocaloric (ECE) and magnetocaloric (MCE) effects are indeed a consequence of the martensitic transition

undergone by the alloy. In contrast to the former case [12], the Co-doped Ni–Mn–Ga alloy exhibits both magneto-caloric and elasto-caloric conventional effects, i.e., the transition temperature increases with an external applied field and applied stress. Therefore, both compressive stress and magnetic field effects results in the stability of the martensite phase. In addition, the entropy values associated with the elastocaloric effect for relatively low applied stresses (about 10 MPa) are only a fraction of the whole available entropy content owing to the fact that the investigated range of stresses is not large enough to induce the transformation of the whole sample. Actually the brittleness of magnetic shape memory alloys is one of the major drawbacks for the practical application of the magnetic shape memory effect, and efforts are devoted to finding materials with improved mechanical performances. Finally, it is shown that application of a magnetic field below 1 T increases the estimated elastocaloric relative cooling power by about 20%. A comparison of elastocaloric and magnetocaloric properties indicates that a similar relative cooling power is reached under application of 10 MPa or 0.8 T.

In the last two papers [13,14] we have used a purpose-built calorimeter that operates under hydrostatic pressures up to 3 kbar in order to observe the pressure effects on the thermal response. The application of hydrostatic pressure under adiabatic conditions causes a change in temperature in any substance, this effect is known as the barocaloric effect (BCE). In the paper [13], we reported for the first time direct-measurements of a caloric effect under hydrostatic pressures in a shape-memory alloy. We observed that the application of a moderate hydrostatic pressure to a magnetic shape-memory alloy gives rise to a caloric effect with a magnitude that is comparable to the giant magnetocaloric effect (MCE) reported in this class of materials, i.e., a BCE of $24.4 \text{ J/kg}\cdot\text{K}$ under a hydrostatic pressure of 2.6 kbar. For the Ni–Mn–In [13], it is worth noting that the isothermal application of pressure results in a decrease

of entropy –i.e., conventional BCE–, whereas the isothermal application of a magnetic field results in an entropy increase –i.e., inverse MCE. This result is consistent with the fact that pressure stabilizes the martensitic phase, whereas magnetic field stabilizes the cubic phase. For the conventional BCE, in the forward transformation –on cooling– the alloy suffers a negative volume change in consequence of the smaller volume of the martensite in comparison to the austenite. By contrast, the inverse MCE is the result of the magnetization decrease in the forward transformation, which reflects the magneto-structural coupling.

On the other hand, the La–Fe–Co–Si alloy [14] –Co–doped in order to increase its transition-point without changing its thermal effects– exhibits an inverse BCE and a conventional MCE. In contrast to the magneto-structural coupling in the Ni–Mn–In, the La–Fe–Co–Si undergoes a magneto-elastic coupling –i.e., there exist the same structure in both sites of the transition point. On cooling, the inverse BCE that shows the LaFeCoSi alloy is the result of the expansion in the unit cell through the transition-point, i.e., a volume increment. But the conventional MCE is due to the fact that upon cooling the magnetization of the low temperature phase is more important than the magnetization in the high temperature phase, which reflects the magneto-elastic coupling. We have made direct -measurements of the adiabatic temperature change, and are in good agreement with the latter results. Finally, it is worth noting that the BCE for moderate pressures –a value of $8.6 \text{ J/kg}\cdot\text{K}$ was obtained for a pressure of about 2 kbar– is larger than the MCE for magnetic fields reachable with permanent magnets.

To sum up, it could be pointed out that all the reported magnetic materials within this thesis are potentially useful for eco-friendly solid-state refrigeration purposes.

BIBLIOGRAPHY

- [1] V. FRANCO, J. BLÁZQUEZ, B. INGALE, and A. CONDE, *Annual Review of Materials Research* **42**, 305 (2012).
- [2] O. GUTFLEISCH, M. A. WILLARD, E. BRÜCK, C. H. CHEN, S. G. SANKAR, and J. P. LIU, *Advanced Materials* **23**, 821 (2011).
- [3] A. SMITH, *The European Physical Journal H* **38**, 507 (2013).
- [4] E. WARBURG, *Ann. Phys.* **249**, 141 (1881).
- [5] W. GIAUQUE, *J. Am. Chem. Soc* **49**, 1864 (1927).
- [6] W. F. GIAUQUE and D. P. MACDOUGALL, *Letters to Editor. Phys. Rev.* **43**, 768 (1933).
- [7] V. K. PECHARSKY and K. A. GSCHNEIDNER, JR., *Phys. Rev. Lett.* **78**, 4494 (1997).
- [8] Kyoto Protocol, In Rio de Janeiro in 1992, more than 160 countries negotiated at the United Nations Conference on Environment and Development

an international treaty to cooperatively consider what they could do to limit average global temperature increases and the resulting climate change. The Kyoto Protocol, signed in Japan on 11 December 1997, is an international agreement linked to the United Nations Framework Convention on Climate Change, which commits its Parties –191 states (all the UN members, except Andorra, Canada, South Sudan and the United States) and the European Union– by setting internationally binding emission reduction targets. Official Web: <http://unfccc.int/2860.php>.

- [9] N. T. TRUNG, V. BIHARIE, L. ZHANG, L. CARON, K. H. J. BUSCHOW, and E. BRÜCK, *Applied Physics Letters* **96**, (2010).
- [10] G. V. BROWN, *Journal of Applied Physics* **47**, 3673 (1976).
- [11] E. BRÜCK, *Journal of Physics D: Applied Physics* **38**, R381 (2005).
- [12] D. E. SOTO-PARRA, E. VIVES, D. GONZÁLEZ-ALONSO, L. MAÑOSA, A. PLANES, R. ROMERO, J. A. MATUTES-AQUINO, R. A. OCHOA-GAMBOA, and H. FLORES-ZÚÑIGA, *Appl. Phys. Lett.* **96**, 071912 (2010).
- [13] L. MAÑOSA, D. GONZÁLEZ-ALONSO, A. PLANES, E. BONNOT, M. BARRIO, J. TAMARIT, S. AKSOY, and M. ACET, *Nat. Mater.* **9**, 478 (2010).
- [14] L. MAÑOSA, D. GONZÁLEZ-ALONSO, A. PLANES, M. BARRIO, J. TAMARIT, I. TITOV, M. ACET, A. BHATTACHARYYA, and S. MAJUMDAR, *Nat. Commun.* **2**, 595 (2011).
- [15] P. O. CASTILLO-VILLA, D. E. SOTO-PARRA, J. A. MATUTES-AQUINO, R. A. OCHOA-GAMBOA, A. PLANES, L. MAÑOSA, D. GONZÁLEZ-ALONSO,

- M. STIPCICH, R. ROMERO, D. RÍOS-JARA, and H. FLORES-ZÚÑIGA, *Phys. Rev. B* **83**, 174109 (2011).
- [16] X. MOYA, E. STERN-TAULATS, S. CROSSLEY, D. GONZÁLEZ-ALONSO, S. KAR-NARAYAN, A. PLANES, L. MAÑOSA, and N. MATHUR, *Adv. Mater.* **25**, 1360 (2013).
- [17] C. DANNORITZER, The Light Bulb Conspiracy, 2010, based on three years of investigation, the film explains the interesting reality of Planned Obsolescence from its beginnings in the 1920s, citing cases where consumer electronics are affected, such as inkjet printers and the iPod, or the disappearance of ladder-resistant nylon stockings. Official Web: <http://www.rtve.es/television/documentales/comprar-tirar-comprar/>.
- [18] K. A. GSCHNEIDNER, JR. and V. PECHARSKY, *International Journal of Refrigeration* **31**, 945 (2008).
- [19] S. Y. DAN'KOV, A. M. TISHIN, V. K. PECHARSKY, and K. A. GSCHNEIDNER, JR., *Phys. Rev. B* **57**, 3478 (1998).
- [20] V. K. PECHARSKY, K. A. GSCHNEIDNER, A. O. PECHARSKY, and A. M. TISHIN, *Phys. Rev. B* **64**, 144406 (2001).
- [21] A. PLANES, L. MAÑOSA, and M. ACET, *Journal of Physics: Condensed Matter* **21**, 233201 (2009).
- [22] E. WARBURG and L. HÖNIG, *Ann. Phys.* **256**, 814 (1883).
- [23] M. CURIE, *Ann. Chem. Phys.* **5**, 289 (1895).

-
- [24] J. M. D. COEY, *Magnetism and magnetic materials*, Cambridge Univ. Press, New York, NY, 2010.
- [25] P. WEISS, *J. Phys.* **6**, 661 (1907).
- [26] P. WEISS, *Compt. Rend.* **143**, 1136 (1906).
- [27] P. DEBYE, *Ann. Phys.* **81**, 1154 (1927).
- [28] P. WEISS and A. PICCARD, *C.R. Hebd. Séan. Acad. Sci. Paris* **166**, 352 (1918).
- [29] J. W. WILLIAMS, *Peter Josseph Wilhelm Debye 1884-1966*, National Academy of Science Washington D. C., 1 edition, 1975.
- [30] K. P. SKOKOV, V. V. KHOVAYLO, K.-H. MÜLLER, J. D. MOORE, J. LIU, and O. GUTFLEISCH, *Journal of Applied Physics* **111**, 07A910 (2012).
- [31] T. A. EDISON, Pyromagnetic Motor, 1888, US Patent US380100.
- [32] T. A. EDISON, Pyromagnetic Generator, 1892, US Patent US476983.
- [33] N. TESLA, Thermo-Magnetic Motor, 1889, US Patent US396121.
- [34] N. TESLA, Pyromagneto-Electric Generator, 1890, US Patent US428057.
- [35] J. STEFAN, *Wien. Ber.* **64**, 193 (1871).
- [36] J. STEFAN, *Ann. Phys.* **274**, 427 (1889).
- [37] D. JILES, *Introduction to Magnetism and Magnetic Materials*, Taylor & Francis CRC Group, Department of Materials Science and Engineering and Department of Electrical and Computer Engineering, Iowa State University, Ames, Iowa, USA, 2 edition, 1998.

- [38] B. CULLITY and C. GRAHAM, *Introduction to Magnetic Materials*, Wiley-IEEE Press, John Wiley & sons, Inc., University of Notre Dame and UNiversity of Pennsylvania, respectively, 2 edition, 2009.
- [39] K. A. GSCHNEIDNER, JR., V. K. PECHARSKY, and A. O. TSOKOL, *Reports on Progress in Physics* **68**, 1479 (2005).
- [40] National High Magnetic Field Laboratory (1995-present day), 1800 E. Paul Dirac Drive, Tallahassee, FL 32310-3706, Phone: (850) 644-0311. Official Web: <http://www.magnet.fsu.edu/mediacenter/factsheets/records.html>.
- [41] P. GORRIA, J. L. S. LLAMAZARES, P. ÁLVAREZ, M. J. PÉREZ, J. S. MARCOS, and J. A. BLANCO, *Journal of Physics D: Applied Physics* **41**, 192003 (2008).
- [42] J. BARCLAY and W. STEYERT, Active magnetic regenerator, 1982, US Patent 4-332-135.
- [43] N. DE OLIVEIRA and P. VON RANKE, *Physics Reports* **489**, 89 (2010).
- [44] J. LIU, T. GOTTSCHALL, K. P. SKOKOV, J. D. MOORE, and O. GUTFLEISCH, *Nature Materials* , 620 (2012).
- [45] K. A. GSCHNEIDNER, JR. and V. K. PECHARSKY, *Journal of Applied Physics* **85**, 5365 (1999).
- [46] C. ZIMM, A. JASTRAB, A. STERNBERG, V. K. PECHARSKY, K. GSCHNEIDNER, JR, M. OSBORNE, and I. ANDERSON, Description and Performance of a Near-Room Temperature Magnetic Refrigerator, in *Advances in Cryogenic Engineering*, edited by P. KITTEL, volume 43 of *Advances in Cryogenic Engineering*, pp. 1759–1766, Springer US, 1998.

-
- [47] B. YU, Q. GAO, B. ZHANG, X. MENG, and Z. CHEN, *International Journal of Refrigeration* **26**, 622 (2003).
- [48] A. ROWE and A. TURA, *International Journal of Refrigeration* **29**, 1286 (2006), Magnetic Refrigeration at Room Temperature.
- [49] M.-A. RICHARD, A. M. ROWE, and R. CHAHINE, *Journal of Applied Physics* **95**, 2146 (2004).
- [50] C. ZIMM, A. BOEDER, J. CHELL, A. STERNBERG, A. FUJITA, S. FUJIEDA, and K. FUKAMICHI, *International Journal of Refrigeration* **29**, 1302 (2006), Magnetic Refrigeration at Room Temperature.
- [51] C. ZIMM, A. STERNBERG, A. JASTRAB, A. BOEDER, L. LAWTON, and J. CHELL, Rotating bed magnetic refrigeration apparatus, 2003, U.S. Patent 6-526-759.
- [52] M. SOUTHWOOD and P. GRAY, Rare Earths: Too Late To The Party?, The figures were obtained from an investment research of Goldman Sachs & Partners Australia with date 4 May 2011.
- [53] V. K. PECHARSKY and K. A. GSCHNEIDNER, JR., *Journal of Magnetism and Magnetic Materials* **200**, 44 (1999).
- [54] H. WADA and Y. TANABE, *Applied Physics Letters* **79**, 3302 (2001).
- [55] F.-X. HU, B.-G. SHEN, J.-R. SUN, Z.-H. CHENG, G.-H. RAO, and X.-X. ZHANG, *Applied Physics Letters* **78**, 3675 (2001).
- [56] A. FUJITA, S. FUJIEDA, Y. HASEGAWA, and K. FUKAMICHI, *Phys. Rev. B* **67**, 104416 (2003).

-
- [57] O. TEGUS, E. BRÜCK, K. H. J. BUSCHOW, and F. R. DE BOER, *Nature* **415**, 150 (2002).
- [58] J. MARCOS, L. MAÑOSA, A. PLANES, F. CASANOVA, X. BATLLE, and A. LABARTA, *Phys. Rev. B* **68**, 094401 (2003).
- [59] T. KRENKE, E. DUMAN, M. ACET, E. F. WASSERMANN, X. MOYA, L. MAÑOSA, and A. PLANES, *Nature Materials* **4**, 450 (2005).
- [60] N. T. TRUNG, L. ZHANG, L. CARON, K. H. J. BUSCHOW, and E. BRÜCK, *Applied Physics Letters* **96**, 172504 (2010).
- [61] V. K. PECHARSKY and K. A. GSCHNEIDNER, *Applied Physics Letters* **70**, 3299 (1997).
- [62] S. Y. DAN'KOV, A. M. TISHIN, V. K. PECHARSKY, and K. A. GSCHNEIDNER, JR., *Phys. Rev. B* **57**, 3478 (1998).
- [63] P. WEBSTER and K. ZIEBECK, *Magnetic Properties of Metals*, Berlin: Springer, 1988, Landolt-Börnstein e group III condensed matter, vol. 19C, pag. 75-184.
- [64] T. GRAF, C. FELSER, and S. S. PARKIN, *Progress in Solid State Chemistry* **39**, 1 (2011).
- [65] F. HEUSLER, W. STARCK, and E. HAUPT, *Verh. d. DPG* **5**, 220 (1903).
- [66] F. HEUSLER, *Verh. d. DPG* **5**, 219 (1903).
- [67] J. PONS, V. CHERNENKO, R. SANTAMARTA, and E. CESARI, *Acta Materialia* **48**, 3027 (2000).

- [68] W. ITO, Y. IMANO, R. KAINUMA, Y. SUTOU, K. OIKAWA, and K. ISHIDA, *Metallurgical and Materials Transactions A* **38**, 759 (2007).
- [69] V. SÁNCHEZ-ALARCOS, J. PÉREZ-LANDAZÁBAL, V. RECARTE, I. LUCIA, J. VÉLEZ, and J. RODRÍGUEZ-VELAMAZÁN, *Acta Materialia* **61**, 4676 (2013).
- [70] A. AYUELA, J. ENKOVAARA, K. ULLAKKO, and R. M. NIEMINEN, *Journal of Physics: Condensed Matter* **11**, 2017 (1999).
- [71] T. GRAF, S. S. P. PARKIN, and C. FELSER, *Magnetics, IEEE Transactions on* **47**, 367 (2011).
- [72] J. PIERRE, R. SKOLOZDRA, J. TOBOLA, S. KAPRZYK, C. HORDEQUIN, M. KOUACOU, I. KARLA, R. CURRAT, and E. LELIÉVRE-BERNA, *Journal of Alloys and Compounds* **262–263**, 101 (1997), Proceedings of the Twelfth International Conference on Solid Compounds of Transition Elements.
- [73] V. KSENOFONTOV, G. MELNYK, M. WOJCIK, S. WURMEHL, K. KROTH, S. REIMAN, P. BLAHA, and C. FELSER, *Phys. Rev. B* **74**, 134426 (2006).
- [74] T. SÁNCHEZ, R. S. TURTELLI, R. GRÖSSINGER, M. SÁNCHEZ, J. SANTOS, W. ROSA, V. PRIDA, L. ESCODA, J. SUÑOL, V. KOLEDOV, and B. HERNANDO, *Journal of Magnetism and Magnetic Materials* **324**, 3535 (2012), Fifth Moscow international symposium on magnetism.
- [75] C. KITTEL, *Introducción a la física del estado sólido*, Reverté, 3 edition, 2003.
- [76] M. SINGH, H. S. SAINI, J. THAKUR, A. H. RESHAK, and M. K. KASHYAP, *Journal of Solid State Chemistry* **208**, 71 (2013).

-
- [77] G. D. LIU, X. F. DAI, H. Y. LIU, J. L. CHEN, Y. X. LI, G. XIAO, and G. H. WU, *Phys. Rev. B* **77**, 014424 (2008).
- [78] K. OTSUKA and C. WAYMAN, *Shape Memory Materials*, Cambridge University Press, 1 edition, 1998.
- [79] M. ACET, L. MAÑOSA, and A. PLANES, *Magnetic-Field-Induced Effects in Martensitic Heusler-Based Magnetic Shape Memory Alloys*, Elsevier B.V., 2011, Chapter 4, Handbook of Magnetic Materials, Volume 19, Ed. by K.H.J. Buschow.
- [80] K. ULLAKKO, J. K. HUANG, C. KANTNER, R. C. O'HANDLEY, and V. V. KOKORIN, *Applied Physics Letters* **69**, 1966 (1996).
- [81] R. KAINUMA, Y. IMANO, W. ITO, Y. SUTOU, H. MORITO, S. OKAMOTO, O. KITAKAMI, K. OIKAWA, A. FUJITA, and T. KANOMATA, *Nature* , 957 (2006).
- [82] B. INGALE, R. GOPALAN, V. CHANDRASEKARAN, and S. RAM, *Journal of Applied Physics* **105**, (2009).
- [83] T. BÖHNERT, V. VEGA, A.-K. MICHEL, V. M. PRIDA, and K. NIELSCH, *Applied Physics Letters* **103**, 5 (2013).
- [84] S. GIRI, M. PATRA, and S. MAJUMDAR, *Journal of Physics: Condensed Matter* **23**, 073201 (2011).
- [85] W. CALLISTER, *Introducción a la Ciencia e Ingeniería de los Materiales*, Ed. Reverté, 1988.

-
- [86] J. W. CHRISTIAN, G. B. OLSON, and M. COHEN, *J. Phys. IV France* **5**, C8 (1995).
- [87] X. MOYA, D. GONZÁLEZ-ALONSO, L. MAÑOSA, A. PLANES, V. O. GARLEA, T. A. LOGRASSO, D. L. SCHLAGEL, J. L. ZARESTKY, S. AKSOY, and M. ACET, *Phys. Rev. B* **79**, 214118 (2009).
- [88] X. MOYA, L. MAÑOSA, A. PLANES, T. KRENKE, M. ACET, and E. F. WASSERMANN, *Materials Science and Engineering: A* **438–440**, 911 (2006), Proceedings of the International Conference on Martensitic Transformations.
- [89] S. AKSOY, M. ACET, P. P. DEEN, L. MAÑOSA, and A. PLANES, *Phys. Rev. B* **79**, 212401 (2009).
- [90] E. BONNOT, E. VIVES, L. MAÑOSA, A. PLANES, and R. ROMERO, *Phys. Rev. B* **78**, 094104 (2008).
- [91] E. BONNOT, R. ROMERO, X. ILLA, L. MAÑOSA, A. PLANES, and E. VIVES, *Phys. Rev. B* **76**, 064105 (2007).
- [92] X. REN and K. OTSUKA, *Nature* , 579 (1997).
- [93] R. C. O’HANDLEY, S. J. MURRAY, M. MARIONI, H. NEMBACH, and S. M. ALLEN, *Journal of Applied Physics* **87**, 4712 (2000).
- [94] S. KAUFMANN, U. K. RÖSSLER, O. HECZKO, M. WUTTIG, J. BUSCHBECK, L. SCHULTZ, and S. FÄHLER, *Phys. Rev. Lett.* **104**, 145702 (2010).
- [95] T. KRENKE, M. ACET, E. F. WASSERMANN, X. MOYA, L. MAÑOSA, and A. PLANES, *Phys. Rev. B* **73**, 174413 (2006).

-
- [96] T. KRENKE, M. ACET, E. F. WASSERMANN, X. MOYA, L. MAÑOSA, and A. PLANES, *Phys. Rev. B* **72**, 014412 (2005).
- [97] T. DURLU, *Scripta Metallurgica* **12**, 865 (1978).
- [98] E. LIU, W. WANG, L. FENG, W. ZHU, G. LI, J. CHEN, H. ZHANG, G. WU, C. JIANG, and H. XU, *Nature Communications* , 873 (2012).
- [99] S. AKSOY, T. KRENKE, M. ACET, E. F. WASSERMANN, X. MOYA, L. MAÑOSA, and A. PLANES, *Applied Physics Letters* **91**, (2007).
- [100] T. KRENKE, E. DUMAN, M. ACET, X. MOYA, L. MAÑOSA, and A. PLANES, *Journal of Applied Physics* **102**, (2007).
- [101] J. MARCOS, A. PLANES, L. MAÑOSA, A. LABARTA, and B. J. HATTINK, *Phys. Rev. B* **66**, 054428 (2002).
- [102] Z. LI, C. JING, J. CHEN, S. YUAN, S. CAO, and J. ZHANG, *Applied Physics Letters* **91**, (2007).
- [103] F.-X. HU, B.-G. SHEN, J.-R. SUN, Z.-H. CHENG, G.-H. RAO, and X.-X. ZHANG, *Applied Physics Letters* **78**, 3675 (2001).
- [104] F.-X. HU, B.-G. SHEN, J.-R. SUN, G.-J. WANG, and Z.-H. CHENG, *Applied Physics Letters* **80**, 826 (2002).
- [105] K. BUSCHOW and F. D. BOER, *Physics of Magnetism and Magnetic Materials*, Kluwer Academic Publishers, Van Der Waals-Zeeman Instituut, Universiteit van Amsterdam, Amsterdam, The Netherlands, 2 edition, 2004.
- [106] A. BECQUEREL, *Ann. chim. phys.* **31**, 371 (1827).

-
- [107] E. GMELIN, *Modern low-temperature calorimetry: A Review*, Thermochemica acta, Elsevier, 1979.
- [108] J. MARCOS, F. CASANOVA, X. BATLLE, A. LABARTA, A. PLANES, and L. MAÑOSA, *Review of Scientific Instruments* **74**, 4768 (2003).
- [109] J. ORTÍN, *Thermochemica Acta* **121**, 397 (1987).
- [110] S. AKSOY, *Magnetic interactions in martensitic Ni-Mn based Heusler systems*, PhD thesis, Fakultät für Physik der Universität Duisburg-Essen, 2010.
- [111] X. MOYA, *Comportament vibracional i magnètic d'aliatges funcionals tipus Heusler*, PhD thesis, Departament d'Estructura i Constituents de la Matèria de la Universitat de Barcelona, 2008.

CURRICULUM VITAE

David González Alonso

Universitat de Barcelona
Estructura i Constituents de la Matèria
Av. Diagonal, 645
08028 Barcelona, Spain
Citizenship: Spanish

Office: (+34) 934021176
Fax: (+34) 934021198
Email: dagal99@gmail.com

Academic degrees

- Physics Degree, University of Barcelona (October 2007).
- Master on Biophysics, University of Barcelona (February 2009).
- PhD student, University of Barcelona (September 2008 - currently).

Languages

	Speaking	Writing	Reading
Catalan (native)	E	E	E
Spanish (native)	E	E	E
English	G	G	G

E: Excellent knowledge; G: Good Knowledge

Scholarships

- PhD Grant supported by the Spanish Government, Ministry of Science and Innovation (September 2008 - August 2012).

Given Seminars and Lectures

- Given Seminar on Experimental Physics for high-school students, organized by the University of Barcelona (Genuary-February 2010).
- Given Lecture on Physics Laboratory for freshman chemistry, University of Barcelona (Fall Semester 2010).
- Given Lecture on Basic Laboratory for chemical engineering freshman, University of Barcelona (Spring Semester 2011).

Participation in Congresses

- "Hysteretic aspects of the inverse magnetocaloric effect in a martensitic Ni-Mn-Sn alloy", I. Titov, D. Gonzalez-Alonso, M. Acet. 3rd International Conference on Ferromagnetic Shape Memory Alloys (ICFSMA'11), Dresden, Germany, on June,18-22 2011. ORAL.

CURRICULUM VITAE

- “Barocaloric effects in giant magnetocaloric materials”, Ll. Mañosa, D. González-Alonso, A. Planes, M. Barrio, J.-Ll. Tamarit, S. Majumdar, M. Acet. 3rd International Conference on Ferromagnetic Shape Memory Alloys, Dresden, Germany, on June,18-22 2011. INVITED TALK.
- “Interplay of thermal, magnetic and hydrostatic-pressure as external fields in Ni_{49.26}Mn_{36.08}In_{14.66}”, D. González-Alonso, L. Mañosa, A. Planes, O. Gutfleisch, K. P. Skokov, J. D. Moore, M. Acet. Joint European Magnetic Symposia (JEMS), 9-14 2012. Poster.

Stays Abroad

- Experimentalphysik Department, University of Duisburg-Essen, Germany (12/January-12/March 2011).
- Leibniz-Institut für Festkörper- und Werkstoffforschung (IFW), Dresden, Germany (10/January-10/March 2012).

List of Publications

- 1.Xavier Moya, David González-Alonso, Lluís Mañosa, Antoni Planes, V.O. Garlea, T.A. Lograsso, D.L. Schlagel, J.L. Zaretsky, Seda Aksoy and Mehmet Acet, *Lattice dynamics in magnetic superelastic Ni-Mn-In alloys: Neutron scattering and ultrasonic experiments*, Physical Review B 79, 214118 (2009).
- 2.Daniel Soto-Parra, Eduard Vives, David González-Alonso, Lluís Mañosa, Antoni Planes, Ricardo Romero, J.A. Matutes-Aquino, R.A. Ochoa-Gamboa and H. Flores-Zúñiga, *Stress- and magnetic field-induced entropy changes in Fe-doped Ni-Mn-Ga shape-memory alloys*, Applied Physics Letters 96, 071912 (2010).
- 3.Lluís Mañosa, David González-Alonso, Antoni Planes, Erell Bonot, Maria Barrio, Josep-Lluís Tamarit, Seda Aksoy and Mehmet Acet, *Giant solid-state barocaloric effect in the Ni-Mn-In magnetic shape-memory alloy*, Nature Materials, 9, 478 (2010).
4. P. O. Castillo-Villa, D. E. Soto-Parra, J. A. Matutes-Aquino, R. A. Ochoa-Gamboa, Antoni Planes, Lluís Mañosa, David González-Alonso, Marcelo Stipcich, Ricardo Romero, D. Ríos-Jara and H. Flores-Zúñiga, *Caloric effects induced by magnetic and mechanical fields in a Ni₅₀Mn_{25-x}Ga₂₅Cox magnetic shape memory alloy*, Physical Review B 83, 174109 (2011).
- 5.Lluís Mañosa, David González-Alonso, Antoni Planes, Maria Barrio, Josep-Lluís Tamarit, Ivan S. Titov, Mehmet Acet, Amitava Bhattacharyya and Subham Majumdar, *Inverse barocaloric effect in the giant magnetocaloric La-Fe-Si-Co compound*, Nature Communications 2, 595 (2011).
- 6.Ivan Titov, Mehmet Acet, Michael Farle, David González-Alonso, Lluís Mañosa, Antoni Planes, Thorsten Krenke, *Hysteresis effects in the inverse magnetocaloric effect in martensitic Ni-Mn-In and Ni-Mn-Sn*, Journal of Applied Physics, 112, 073914 (2012).
- 7.Xavier Moya, Enric Stern-Taulats, Sam Crossley, David González-Alonso, Sohini Kar-Narayan, Antoni Planes, Lluís Mañosa, and Neil D. Mathur, *Giant Electrocaloric Strength in Single-Crystal BaTiO₃*, Advanced Materials 25, 1360 (2013).

Computer Skills

- User of Matlab, Mathematica, Origin, Fortran, C/C++, LaTeX and Labview.
- User level Knowledge of Windows, Linux and Macintosh (OSX).

CURRICULUM VITAE

Miscellaneous

- Working as a waiter from 1-31/August/1999.
- Working as a waiter from August/2001-Sept/2008.
- Certificate of CAP/ Teacher Training Course for High-School Students, University of Barcelona (May 2008).
- Advanced Open Water Diver (October 2011).
- Patró de iot/Recreational Skipper: To a line parallel to the coast traced to 60 miles with a 20m-length limit boat for sailing and motor. (September 2012).

Last updated: January, 2014